NASA/CR—2010-216330

Computational Aerodynamic Simulations of a Spacecraft Cabin Ventilation Fan Design

Daniel L. Tweedt
AP Solutions, Inc., Solon, Ohio

December 2010

NASA STI Program . . . in Profile

Since its founding, NASA has been dedicated to the advancement of aeronautics and space science. The NASA Scientific and Technical Information (STI) program plays a key part in helping NASA maintain this important role.

The NASA STI Program operates under the auspices of the Agency Chief Information Officer. It collects, organizes, provides for archiving, and disseminates NASA's STI. The NASA STI program provides access to the NASA Aeronautics and Space Database and its public interface, the NASA Technical Reports Server, thus providing one of the largest collections of aeronautical and space science STI in the world. Results are published in both non-NASA channels and by NASA in the NASA STI Report Series, which includes the following report types:

- TECHNICAL PUBLICATION. Reports of completed research or a major significant phase of research that present the results of NASA programs and include extensive data or theoretical analysis. Includes compilations of significant scientific and technical data and information deemed to be of continuing reference value. NASA counterpart of peer-reviewed formal professional papers but has less stringent limitations on manuscript length and extent of graphic presentations.

- TECHNICAL MEMORANDUM. Scientific and technical findings that are preliminary or of specialized interest, e.g., quick release reports, working papers, and bibliographies that contain minimal annotation. Does not contain extensive analysis.

- CONTRACTOR REPORT. Scientific and technical findings by NASA-sponsored contractors and grantees.

- CONFERENCE PUBLICATION. Collected papers from scientific and technical conferences, symposia, seminars, or other meetings sponsored or cosponsored by NASA.

- SPECIAL PUBLICATION. Scientific, technical, or historical information from NASA programs, projects, and missions, often concerned with subjects having substantial public interest.

- TECHNICAL TRANSLATION. English-language translations of foreign scientific and technical material pertinent to NASA's mission.

Specialized services also include creating custom thesauri, building customized databases, organizing and publishing research results.

For more information about the NASA STI program, see the following:

- Access the NASA STI program home page at *http://www.sti.nasa.gov*

- E-mail your question via the Internet to *help@sti.nasa.gov*

- Fax your question to the NASA STI Help Desk at 443–757–5803

- Telephone the NASA STI Help Desk at 443–757–5802

- Write to:
  NASA Center for AeroSpace Information (CASI)
  7115 Standard Drive
  Hanover, MD 21076–1320

NASA/CR—2010-216330

Computational Aerodynamic Simulations of a Spacecraft Cabin Ventilation Fan Design

Daniel L. Tweedt
AP Solutions, Inc., Solon, Ohio

Prepared under Contract NNC06BA07B, Task 190

National Aeronautics and
Space Administration

Glenn Research Center
Cleveland, Ohio 44135

December 2010

Acknowledgments

Final Report Submitted to ASRC Aerospace Corporation for Purchase Order Number AS6461 NASA Glenn Research Center Prime Contract Number NNC06BA07B, Task 190. The author would like to thank Dr. Rodrick V. Chima of the NASA Glenn Research Center for the many helpful discussions regarding computational fluid dynamics code development and application. The author would also like to thank Hamilton Sundstrand for supplying the fan design information, and Mr. Timothy M. Roach of the NASA Glenn Research Center for extracting coordinate data from the supplied three-dimensional fan model.

Level of Review: This material has been technically reviewed by expert reviewer(s).

Available from

NASA Center for Aerospace Information
7115 Standard Drive
Hanover, MD 21076–1320

National Technical Information Service
5301 Shawnee Road
Alexandria, VA 22312

Available electronically at http://gltrs.grc.nasa.gov

Computational Aerodynamic Simulations of a Spacecraft Cabin Ventilation Fan Design

Daniel L. Tweedt
AP Solutions, Inc.
Solon, Ohio 44139

Abstract

Quieter working environments for astronauts are needed if future long-duration space exploration missions are to be safe and productive. Ventilation and payload cooling fans are known to be dominant sources of noise, with the International Space Station being a good case in point. To address this issue cost effectively, early attention to fan design, selection, and installation has been recommended, leading to an effort by NASA to examine the potential for small-fan noise reduction by improving fan aerodynamic design. As a preliminary part of that effort, the aerodynamics of a cabin ventilation fan designed by Hamilton Sundstrand has been simulated using computational fluid dynamics codes, and the computed solutions analyzed to quantify various aspects of the fan aerodynamics and performance. Four simulations were performed at the design rotational speed: two at the design flow rate and two at off-design flow rates. Following a brief discussion of the computational codes, various aerodynamic- and performance-related quantities derived from the computed flow fields are presented along with relevant flow field details. The results show that the computed fan performance is in generally good agreement with stated design goals.

Introduction

Quieter working environments for astronauts are needed if future long-duration space exploration missions are to be safe and productive. Ventilation and payload cooling fans are known to be dominant sources of noise, with the International Space Station being a good case in point. Noise management by means of externally applied mechanisms, such as surface acoustic treatments and mufflers, is common and effective, but tends to be costly in terms of subsystem performance and weight (Refs. 1 to 3). To address this issue more cost effectively, early attention to fan design, selection, and installation has been recommended.

The current study is part of a larger effort to examine the potential for small-fan noise reduction through improvements in fan aerodynamic design. To initiate that effort, a cabin ventilation fan designed by Hamilton Sundstrand was selected for detailed analysis using computational fluid dynamics (CFD) codes. The analysis involves computationally simulating the aerodynamics of the fan at its design operating point, and then examining and quantifying various aspects of the fan aerodynamics and performance from the computed solutions. It is anticipated that these results, presented below, will serve as a reference for future aerodynamic design investigations aimed at quieter fan operation.

In addition to simulating the cabin ventilation fan at its aerodynamic design point, two off-design simulations were also performed, one at a higher flow rate and the other at a lower flow rate, to quantify the fan operating characteristics at the design rotational speed.

Fan Geometry and Design Operation

Geometric and aerodynamic design information for the cabin ventilation fan design was supplied by Hamilton Sundstrand to the NASA Glenn Research Center. A computer-generated picture of the fan is shown in Figure 1, where a three-dimensional cutaway view reveals the fan assembly with all of its major components. The electric drive motor is an integral part of the subsystem, as is a flow straightener upstream of the fan. The inlet flow straightener is a honeycomb structure with an effective/flow path diameter of 3.50 in., a thickness of 0.9375 in., and a cell size (or center-to-center cell spacing) of 0.1875 in.

A meridional view of the fan system flow path is shown in Figure 2, which also indicates the location of each blade row. The rotor has nine blades, a tip clearance of 0.009 in., and a design rotational speed of 16 000 rpm at 70 °F. The vertical dashed line below the hub contour in Figure 2 indicates the end of the rotor hub. Downstream of this location the hub is stationary. The stator has 11 blades, and each blade has a virtually uniform profile shape along its span. At the stator exit is an annular duct that extends downstream over three stator chord lengths, or four duct heights, and provides an annulus area increase before ending abruptly as the hub radius steps to zero at the back face of the centerbody. Blade section profiles for the rotor and stator are shown in Figure 3.

The specified design flow rate for the fan is 150.3 ft^3/min, with a corresponding total-pressure rise of 3.64 in. of water from inlet to exit. For this specification, the inlet is defined as the upstream side of the flow straightener, and the exit is defined as some (unspecified) location in the circular duct downstream of the centerbody. Design conditions at the inlet are a total pressure of 14.7 psia and a total temperature of 70 °F.

The total-pressure drop across the inlet flow straightener is calculated from the average flow velocity using an empirical correlation provided by Hamilton Sundstrand. For the design flow rate, the calculated pressure drop is 0.0735 in. of water.

Computational Fluid Dynamics

Two different CFD codes were used to simulate the airflow through the fan system: an axisymmetric viscous solver called AVCS and a three-dimensional viscous turbomachinery solver called TSWIFT. Multiple solution domains (grid blocks) were used, with axisymmetric solutions coupled to three-dimensional solutions at mixing planes by means of a separate computer program called SMPI, developed as a companion program for AVCS and TSWIFT. SMPI was also used to couple rotating and stationary three-dimensional solutions together at mixing planes. In general, the three-dimensional TSWIFT solver was used for computational domains in and near blade rows, and the axisymmetric AVCS solver was used for computational domains upstream and downstream of the fan, sufficiently far away from the blade rows.[1]

The AVCS and TSWIFT codes use similar numerical algorithms; both solve the Reynolds-averaged Navier-Stokes equations on body-fitted grids using an explicit, finite-difference scheme. The codes include viscous terms in all grid directions, except that TSWIFT neglects the mixed-derivative viscous terms containing derivatives in the predominantly streamwise grid direction. The discretized equations are solved with a multistage Runge-Kutta time-marching scheme using a spatially varying time step, implicit residual smoothing, and preconditioning (Refs. 4 to 7). All simulations discussed herein were run using a two-stage Runge-Kutta scheme with a CFL (Courant-Friedrichs-Lewy) number of 2.5 and the H-CUSP (convective upwind split pressure) upwind scheme (Refs. 8 and 9). Initial solutions were run using the AUSM+ (advection upstream splitting method) upwind scheme (Ref. 10), which is considered the best for accuracy, but laminar-free shear-layer instabilities were encountered near the rotor blade tip and just downstream of the rotor trailing edge. It is believed that the instabilities are due to the relatively low Reynolds numbers involved, with concomitant laminar/transitional shear layers, and the H-CUSP scheme provides enough artificial dissipation to suppress the laminar instabilities and allow solution convergence.

The TSWIFT code was derived from, and has the same basic features as the SWIFT code (Ref. 11) developed by Chima at the NASA Glenn Research Center. TSWIFT also has a fairly general multiblock capability (when used with SYNCEX; see preceding footnote), includes the two-equation SST (shear stress transport) turbulence model developed by Menter (Ref. 12), and implements Giles' two-dimensional, steady-state, nonreflecting boundary conditions (Refs. 13 and 14) at flow inlet, exit, and mixing-plane boundaries.[2] Note that when a two-equation turbulence model is used, either the Wilcox k-ω model

[1]All program-to-program communications, for mixing planes and direct block-to-block interfaces, were handled using a facility called SYNCEX (pronounced sink-ex). SYNCEX is a message-passing interface that enables two or more executing programs to efficiently exchange data on a single computer and/or over a network.

[2]The SMPI code also implements Giles' two-dimensional, steady-state, and nonreflecting boundary conditions.

(Ref. 15) or the Menter SST model, it is necessary at mixing planes to circumferentially average the computed turbulence properties on the upstream side of the mixing plane. In that case the turbulence kinetic energy, k, and the ratio of turbulence kinetic energy to turbulence dissipation, k/ω, are each mass-averaged. The resulting average values of k and (indirectly) ω are then used as inflow boundary values for the domain on the downstream side of the mixing plane.

For Mach number levels below about 0.3, it becomes necessary to use preconditioning, sometimes referred to as artificial compressibility, to obtain good solution convergence. The preconditioning can also be used at higher Mach numbers, typically because it has been found to generally improve convergence behavior. Mach number levels in the current fan system are nominally around 0.1 or less, except in the rotor where blade-tip-relative Mach numbers exceed 0.3.

Initial solution results revealed that it was also necessary to use double precision for CFD solver execution. Single precision was sufficient for grid generation, solution preprocessing, and solution postprocessing, but proved inadequate for solver execution because of truncation errors in density and pressure. In general, as Mach number levels approach zero, the dimensionless density and pressure each approach a constant positive value with an order of magnitude of one. The resulting flow-field solutions involve relatively small spatial variations in density and pressure, such that property differences computed in single precision are significantly affected by the truncation error.

Fan System Aerodynamic Simulations

The aerodynamic simulations were performed for air modeled as a perfect gas with a ratio of specific heats, γ, equal to 1.400, and with inlet total (stagnation) flow conditions set at standard day sea-level (SSL) values. Since a nonstandard inlet temperature was specified for the design, it was necessary to apply a correction to values of rotational speed, volumetric flow rate, and unit Reynolds number to maintain aerodynamic similarity. The SSL-corrected values were used as input data for the CFD solver, and are now being used for standardized data presentations and comparisons. For the inlet total temperature of 70 °F, the total-temperature correction factor, θ, is equal to 1.0218. Note that a total-pressure correction is not necessary because for an inlet total pressure of 14.7 psia, the total-pressure correction factor, δ, is equal to 1.0000. Applying the temperature correction gives a design rotational speed, $N/\sqrt{\theta}$, of 15 828 rpm, a design flow rate, $Q/\sqrt{\theta}$, of 148.7 ft^3/min, and a unit Reynolds number based on inlet total conditions, $(\rho c/\mu)_{SSL}\ \delta/\theta^{7/6}$, of 5.768×10^5 $in.^{-1}$, where ρ is density, c is the speed of sound, and μ is dynamic viscosity.

The fan inlet conditions are specified for the upstream side of the flow straightener. The inlet computational domain, however, begins on the downstream side, so the total pressure at the computational boundary must include the pressure loss of the straightener. Consistent with the Hamilton Sundstrand pressure-loss correlation for the straightener, applied at the specified design flow rate of 150.3 ft^3/min at 70 °F, a total-pressure drop of 0.0735 in. of water was used. The corresponding total-pressure ratio for the straightener is 0.999819, which is the value specified as input to the CFD solver. Note that this value was used even though the SSL-corrected design flow rate is slightly different. It was also used at the two off-design flow rates that differ from the design value by several percent.

The effects of turbulence were modeled using the Wilcox k-ω turbulence model (Ref. 15), with free-stream turbulence at the upstream computational boundary set at 1.0 percent, along with a turbulence (eddy) viscosity equal to 0.5 times the molecular viscosity. The corresponding turbulence kinetic energy is 1.68×10^{-7} (dimensionless; multiply by reference speed-of-sound squared to obtain a dimensional value). Two versions of the model were applied, a high-Reynolds-number version and a low-Reynolds-number version, the latter being considered more appropriate and accurate for the cases being computed. The high-Reynolds-number model is known to simulate the onset of transition much too soon, which potentially could have a significant impact on the simulation results at such low Reynolds numbers; blade-chord Reynolds numbers are on the order of 70 000 for the rotor and 45 000 for the stator. Applying both models allows an assessment to be made of the relative importance of this effect. Note that both models were

applied only at the design flow condition; at the two off-design flow rates, the low-Reynolds-number model was used.

For computational efficiency, the fan solution and the discharge flow field at the fan system exit were computed separately; that is, the exit discharge solution was not close-coupled to the fan solution. Both computational domains include a section of the annular diffuser duct, so there is a substantial overlap region. The fan solution, the domain of which terminates at the exit of the annular duct, was computed first, with the exit-tip static pressure specified and simple radial-equilibrium solved to determine the radial static-pressure distribution. For the design flow simulation, the exit static pressure was adjusted iteratively to achieve the design flow rate, and the same pressure value was used for both the low- and high-Reynolds-number turbulence model simulations. The corresponding solution for the exit discharge region was then computed using the fan solution to supply upstream boundary values. The exit region solution mainly provides computational total-pressure loss results for the discharge flow, as well as information about the extent of the separation (reverse flow) bubble downstream of the annular diffuser centerbody.

Computational Grids

Hub and tip/casing flow path coordinates were modified slightly to avoid slope discontinuities (sharp corners), since cubic splines were used for interpolation during grid generation. The modifications involved deleting sharp corner points, while adding points to create a small fillet.

A meridional view of the fan system grid blocks is shown in Figure 4, where different colors are used to differentiate nine different blocks. For clarity, only every other grid line has been drawn for each grid. The blue and light-blue blocks on the far left in the inlet duct, and the blue block on the far right in the annular diffuser duct, are two-dimensional/axisymmetric H-grids. The location of the far-left boundary corresponds to the downstream side of the inlet flow straightener, and the lower boundary of the light-blue inlet block is on the fan centerline. The two black blocks represent three-dimensional blade row C-grids: one on the left for the rotor and the other on the right for the stator. The two green blocks represent three-dimensional H-grids that extend the rotor domain upstream and downstream, and the two red blocks represent three-dimensional H-grids that extend the stator domain upstream and downstream. Not indicated in the figure is a rotor-tip clearance gap O-grid block.

The system exit domain contains three two-dimensional/axisymmetric grid blocks, shown in Figure 5. The front part of the blue block, the part located within the annular diffuser duct, is identical to the grid used for the fan system (see Fig. 4, blue grid block on right). The lower boundary of the light-blue base grid and the violet downstream extension tube grid is on the fan centerline.

Both of the inlet duct grid blocks were generated using a Poisson partial differential equation (PDE) solver, otherwise known as an elliptic grid generator, which produces grids with good boundary-normal node clusterings and spacings, and generally good local orthogonality. The annular diffuser duct and system exit grid blocks were generated using an algebraic method because the grid lines are naturally orthogonal, or nearly so.

The blade row grids, except for the rotor exit and stator exit H-grid blocks, were generated using a computer program called TTGRID, which is a modified version of TCGRID (Ref. 16), a three-dimensional grid generator for turbomachinery developed by Chima at the NASA Glenn Research Center. TTGRID applies an elliptic PDE solver to the streamwise-pitchwise (blade-to-blade) mesh surfaces of blade row C- and H-grids.

A three-dimensional view of the rotor grid is shown in Figure 6. Note that the (green) upstream/inlet H-grid overlaps the (black) C-grid and has node-to-node alignment with it. The (green) downstream/exit H-grid also overlaps the C-grid, but the grid nodes are not aligned. An axial-circumferential (blade-to-blade) mesh plot of the rotor grid at the blade tip is shown in Figure 7(a), which also includes magnified views of the blade leading and trailing edge regions. The tip clearance gap O-grid block (light gray) overlaps the C-grid with node-to-node alignment. A circumferential-radial view of the tip clearance grid at a midchord cross section is included in Figure 7(a), on the right. An axial-circumferential mesh plot of the

rotor grid at the hub is shown in Figure 7(b), along with three circumferential-radial-view mesh plots of the grid at the cross sections indicated.

A three-dimensional view of the stator grid is shown in Figure 8. Many of the comments in the previous paragraph also apply to the stator grid, except that the stator does not have an endwall clearance gap, and the upstream and downstream extension H-grid blocks are red. An axial-circumferential mesh plot of the stator grid at midspan is shown in Figure 9, along with three circumferential-radial-view mesh plots for the cross sections indicated.

Turbulent boundary-layer flow solutions near solid walls always involve direct computation of the viscous sublayer; that is, wall functions are not used. It is important, therefore, that node spacings at solid walls be sufficiently small. The nominal wall-normal spacing at hub and tip endwalls is 0.00025 in., and at blade surfaces is 0.00010 in. Corresponding inner-variable wall distances, $y+$, are typically between 1.0 and 2.0 at the endwalls, and between 0.2 and 0.8 at blade surfaces.

Table 1 summarizes the grid blocks and their sizes for the fan system computational domain, and Table 2 summarizes the grid blocks and their sizes for the system exit computational domain.

TABLE 1.—FAN SYSTEM COMPUTATIONAL GRID BLOCKS

Grid block	Size (I×J×K)	Number of nodes
Inlet duct inner H-grid (2–D)	81×1×81	6,561
Inlet duct outer H-grid (2–D)	81×1×81	6,561
Rotor inlet H-grid	13×38×85	41,990
Rotor blade C-grid	201×49×85	837,165
Rotor exit H-grid	73×89×77	500,269
Rotor tip clearance O-grid	157×15×17	40,035
Stator inlet H-grid	13×32×73	30,368
Stator blade C-grid	201×49×73	718,977
Stator exit H-grid	65×89×73	422,305
Exit duct H-grid	29×1×73	2,117

TABLE 2.—FAN EXIT COMPUTATIONAL GRID BLOCKS

Grid block	Size (I×J×K)	Number of nodes
Exit duct/outer H-grid (2–D)	69×1×73	5037
Exit duct/inner H-grid (2–D)	61×1×49	2989
Exit extension tube H-grid (2–D)	57×1×89	5073

Aerodynamic Simulation Results

Fan system CFD results are presented below using averaged and nonaveraged data. Circumferential (pitchwise) averaging of the three-dimensional flow fields was performed on a structured meridional grid for some selected solutions, allowing contour plots to be generated for the averaged flow fields. Detailed comparisons are made at the axial stations indicated with red vertical dashed lines in Figure 10. The stations are labeled as indicated. Note that the vertical blue lines in Figure 10 show mixing plane locations, and the (near-) vertical gray lines show grid block interface locations. Stations 1a and 4b, respectively, are at the upstream and downstream boundaries of the computational domain(s), and are included only for completeness, as well as possible future reference.

Overall averages, obtained by spanwise (radial) averaging of the circumferentially averaged flow field, were calculated at stations 2b, 3d, and 4a, to provide representative performance numbers for the rotor and fan stage. These results are summarized below in Tables 3 and 4, and are presented first because they provide a convenient overview of the operating points and performance values computed for the fan. Note that all simulated cases are included, off-design as well as design, and that the left column indicates the turbulence model used. A fan performance map generated from these results is shown in Figure 11, where total-pressure rise and hydraulic efficiency are graphed against volumetric flow rate.

TABLE 3.—COMPUTED ROTOR PERFORMANCE

Turbulence model	Flow rate $Q/\sqrt{\theta}$, ft^3/min	Pressure rise $\Delta p_{t,2b}$, in. water	Work input $\Delta h_{t,2b}$, in. water	Hydraulic efficiency $\eta_{H,2b}$	Rotor torque T/δ, in.-oz
Low Re	143.18	4.523	5.409	0.8362	7.779
Low Re	148.60	4.313	5.156	0.8366	7.695
Low Re	153.73	4.097	4.909	0.8345	7.579
High Re	148.37	4.299	5.129	0.8381	7.644

TABLE 4.—COMPUTED FAN STAGE PERFORMANCE

Turbulence model	Flow rate $Q/\sqrt{\theta}$, ft^3/min	Pressure rise $\Delta p_{t,3d}$, in. water	Work input $\Delta_{H,3d}$, in. water	Pressure rise $\eta_{H,3d}$ in. water	Hydraulic efficiency $\eta_{H,4a}$
Low Re	143.18	3.899	0.7208	3.658	0.6763
Low Re	148.60	3.690	0.7157	3.435	0.6663
Low Re	153.73	3.480	0.7090	3.209	0.6538
High Re	148.37	3.720	0.7252	3.441	0.6709

Figure 11, as well as in Tables 3 and 4, show the turbulence model version has only a small impact on the computed overall performance for the fan, at least for operation near the aerodynamic design point. At the design flow rate, the computed total-pressure rise is 3.435 in. of water for the fan system (station 4a, low-Reynolds-number model), which is 5.6 percent less than the design objective of 3.640 in. of water. The corresponding hydraulic efficiency of 0.6663 also falls below the design value, estimated to be 0.686. Although the computed total-pressure rise and hydraulic efficiency are less than the values anticipated for the design, the general level of agreement is considered to be good.

Referring again to Figure 11, notice the relative amount of total-pressure loss incurred between stations 3d and 4a. That loss, the exit discharge total-pressure loss, is significant. At the design flow rate the discharge loss is 0.255 in. of water, which is equal to 7.4 percent of the total-pressure rise for the entire fan system.

Several contour plots showing the fan system flow field and the exit discharge region flow field, for the design flow rate, are contained in Figures 12 and 13, respectively, where for Figure 12 the three-dimensional blade-row flow solutions were mixed-out averaged in the circumferential direction.[3] Note that the grid blocks in Figure 4 correspond to the contour plots of Figure 12, the grid blocks in Figure 5 correspond to the contour plots of Figure 13, and all of the contour plots were generated from the solution set obtained with the low-Reynolds-number k-ω turbulence model. The entropy rise and turbulence kinetic energy plots involve dimensionless values, with entropy rise nondimensionalized by the gas constant, R, for air, and turbulence kinetic energy normalized by the inlet kinetic energy. The inlet kinetic energy is based on the magnitude of the mean flow velocity at the flow straightener, $Q/A\sqrt{\theta}$, which has a value of

[3]Turbulence kinetic energy was mass-averaged in the circumferential direction.

37.09 ft/s at the design flow rate. Note also that Figure 13 uses the contour legends in Figure 12, as appropriate, with static-pressure rise using the same legend as total-pressure rise, and axial velocity using the same legend as velocity magnitude.

Noteworthy in Figure 12 are the relatively thick, higher-entropy regions generated at the rotor hub and tip, but especially at the tip. The regions widen as the flow convects downstream, until at the stator they encompass almost 30 percent of the span by the hub, and about 45 percent of the span by the tip. Such extensive endwall viscous-loss regions are somewhat unusual, and are a direct result of the relatively low Reynolds numbers involved. Simple considerations from flat-plate boundary-layer theory suggest that this effect should be expected, although at the tip the highly viscous, three-dimensional nature of the clearance flow seems to amplify it considerably. When the Reynolds number for a flat-plate boundary-layer flow is decreased by a factor of 10, for example, the thickness of the layer increases by a factor of $\sqrt{10}$ (equal to 3.2) if it is laminar, or by a factor of about $\sqrt[5]{10}$ (equal to 1.6) if it is turbulent. Lower Reynolds numbers are also generally associated with delayed, or even nonexistent, laminar-to-turbulent transition, as well as with decreased turbulence viscosity levels.

Also of interest in Figure 12 are the inlet- and exit-diffuser flow fields. The velocity magnitude plot shows the flow in the inlet undergoes a rapid acceleration as it enters the annular passage. On the hub/spinner nose, the flow is overexpanded (accelerated to excessive velocities) because of the high endwall curvature. This overexpansion, combined with a small separation bubble (not visible) just above the sharp corner, leads to a thicker hub boundary layer going into the rotor and adds to the static-pressure rise across the rotor. In the exit diffuser, the flow is aerodynamically clean along the hub, but not along the tip endwall where a viscous boundary-layer separation exists. The separated (reverse flow) region is large enough that the average axial velocities are slightly negative very near the endwall. Later, more detailed results will be provided that show the flow structure of the separated region is highly three-dimensional. At the hub there is no reverse flow until after the flow discharges into the downstream tube, as revealed by the axial velocity contour plot in Figure 13. The thick black contour in that plot corresponds to a value of zero and outlines a region of reverse flow (negative axial velocity) just downstream of the diffuser centerbody.

Axial distributions of static-pressure rise at the hub and tip endwalls for the fan system and the exit discharge region are shown in Figures 14 and 15, respectively. These results correspond to the design flow rate and involve circumferentially mixed-out averaged flow-field solutions. Both the low- and high-Reynolds-number turbulence model results are included for comparison, but the differences between them are small. Blade row locations are indicated by thin vertical lines with labels, so various sections of the flow path can be identified along with corresponding static-pressure rise changes and gradients. As expected, static pressure generally increases in the axial/streamwise direction; however, the static-pressure rise and associated pressure gradients are by far the largest in and across the rotor. Static-pressure recovery for the diffuser is good, with static pressure increasing by 0.780 in. of water from station 3a to station 3d. The corresponding total-pressure loss is somewhat high, however, at 0.308 in. of water. When this loss is added to the discharge loss, the total-pressure loss for the entire diffusion process (station 3a to station 4a) is 0.563 in. of water, or 16.4 percent of the total-pressure rise for the entire fan system, for a corresponding static-pressure rise of 1.176 in. of water.

Line graphs of circumferentially mixed-out averaged results at all axial stations from 1b through 3d, for the design flow rate, are presented in Figures 16 through 23, respectively. A fairly extensive set of graphs is included for documentation purposes, so many of the graphs are not discussed. Again, results for the low- and high-Reynolds-number turbulence models are included for comparison, and the differences between them are generally small. Note that the contour plots of Figure 12 may be helpful for interpreting these line graphs, by providing a broader perspective for the station data.

Referring to Figures 17(a) and 19(a), corresponding respectively to stations 2a and 2b, the total-pressure rise and work input distributions downstream of the rotor are fairly flat for much of the passage, that is, from about 15 to 70 percent of passage height, in which region the hydraulic efficiency is high at around 0.950. Near the endwalls, the efficiency decreases as a result of higher total-pressure losses there, appearing as higher entropy in the contours of Figure 12. Note that it is common practice with pumps

and low-speed fans to calculate hydraulic efficiency using work input based on changes in tangential velocity multiplied by blade speed, $\Delta(uv_\theta)$, a kinematic quantity. At low Reynolds numbers, however, this approach leads to excessive errors because viscous effects are too prevalent. To avoid such errors here, the work input has been calculated using total-enthalpy rise, $\Delta(h_t)$, a thermodynamic quantity. A comparison of the two methods at station 2a is provided in Figure 18, where the errors are substantial near the endwalls. Similarly, it would be more accurate to use thermodynamic adiabatic efficiency rather than hydraulic efficiency, but convention favors the latter. In general, calculated hydraulic efficiencies are greater than corresponding adiabatic efficiencies, with the differences depending on the particular conditions involved, and decreasing to zero as flow compressibility approaches zero. For all cases presented herein, representative hydraulic efficiency values are greater than adiabatic efficiency values by an amount somewhere between 0.0023 and 0.0038.

As the rotor exit flow convects downstream, first through the stator blade row, and then through the annular diffuser, the flow property profiles become progressively more rounded; that is, less flat (compare results at stations 2a through 3d in Figs. 17(a) through 23(b)). Viscous dissipation and blade-row generated secondary flows are the fluid dynamic mechanisms producing this effect, both working to expand the influence of the endwalls by mixing the endwall fluid with the high-efficiency core flow. Most of the rotor exit flow swirl (negative tangential velocity) is removed by the stator, which leaves less than 8° of residual swirl at its exit. Near the hub and tip endwalls, secondary flow effects in the stator blade row lead to some overturning, that is, to positive tangential velocities at the stator exit (see station 3a in Fig. 20), but the amount of overturning is not excessive.

Line graphs showing several blade row parameters relevant to the aerodynamic design and performance of the fan are presented in Figures 24 and 25. Parameters for the rotor blade row are shown in Figure 24, and parameters for the stator blade row are shown in Figure 25. The results graphed are based on circumferentially mixed-out average quantities at blade leading and trailing edge meridional stations, and results for the low- and high-Reynolds-number turbulence models are both included for comparison. For the rotor (see Fig. 24(a)), the graph of total-pressure loss coefficient shows low losses over most of the span, corresponding to the high hydraulic efficiencies discussed earlier for the same approximate region of the passage. Near the hub and tip endwalls, however, the loss coefficients are much higher due to the additional losses generated by the endwall flows. The high-loss regions, especially the tip, involve a substantial fraction of the passage flow, and therefore have a large effect on overall performance. The graph of diffusion factor shows a nearly constant value of around 0.4 everywhere outside the endwall flow regions, indicating low to moderate levels of aerodynamic blade loading, at least by conventional standards. Near the hub and tip, diffusion factor follows roughly the same trend as loss coefficient. Given the nominal diffusion factor value of 0.4, excluding the high-loss regions, the amount of endwall-generated loss (entropy) seems inordinately large and demonstrates the increased influence of viscosity at low Reynolds numbers.

For the stator (see Fig. 25(a)), the graph of loss coefficient indicates moderate total-pressure loss levels, and the graph of diffusion factor reveals low to moderate blade loading. Notice that the loss coefficients very near the endwalls are negative (truncated by the graph), but that the maximum values are somewhat close by, that is, in the general vicinity of each endwall. This is a result of secondary flow migration in the blade row, where low-momentum fluid is transported away from the endwalls. Although the diffusion factors are fairly low by conventional standards, it is noteworthy that the flow deviation angles are relatively large (see Fig. 25(a)), around 15° over most of the span. Apparently, the large deviation angles are also a low-Reynolds-number effect.

The rotor blade-to-blade flow field in the rotating frame-of-reference is shown in Figure 26 for three stream surfaces of revolution: one at 85 percent of passage flow (near the tip), one at 50 percent of passage flow (near midspan), and one at 15 percent of passage flow (near the hub). Contours of relative velocity magnitude are plotted using the same contour range for all three stream surfaces, and flow solutions for both the low- and high-Reynolds-number turbulence models are presented for comparison. In Figure 27, contours of turbulence kinetic energy (normalized by inlet kinetic energy) are shown for the 50 percent of passage flow stream surface, with small red arrows indicating locations where laminar-to-turbulent

boundary layer transition occurs. Transition behavior and turbulence development on the blade surface for the near-hub and near-tip stream surfaces are generally similar to that at midspan, so turbulence kinetic energy contours are not shown for those locations.[4] Line graphs showing chordwise distributions of rotor blade surface pressure coefficient, C_p, for the 15, 50, and 85 percent of passage flow stream surfaces are provided in Figure 28. The pressure coefficient accounts for the effects of rotation and radius change and the reference values for static and relative total pressure are based on the mixed-out average conditions at the blade leading edge. In these line graphs, the top curve corresponds to the blade pressure surface, the bottom curve corresponds to the blade suction surface, and the vertical spacing between the curves is related to the local aerodynamic loading (static pressure difference) at a particular chordwise location. In the contour plots, the upper blade surface corresponds to the suction surface.

In general, the blade-to-blade flow field for all three stream surfaces is aerodynamically clean and robust. The pressure coefficient distributions are all similar and show that the rotor blade loading is maximum at the front of the blade, very near the leading edge, and decreases almost linearly from about 10 percent of the chord to the trailing edge. On the blade suction surface, the static-pressure gradient, or rate of flow deceleration/diffusion, is fairly uniform, and the boundary layer remains attached. With the low-Reynolds-number turbulence model, the blade boundary layers are mostly laminar, and the suction-surface transition to turbulence takes place somewhere between midchord and the trailing edge, depending on spanwise location (see footnote). At midspan, the transition occurs at 75 percent chord (see small red arrow in Fig. 27). With the high-Reynolds-number model, transition to turbulence generally occurs at the front of the blade, on both sides, and the resulting turbulent boundary layers are noticeably thicker, as is the wake. Aside from that, however, the flow fields are very similar. It might be added that it is unusual to have a nearly all-laminar blade flow, such as that simulated using the low-Reynolds-number model, but the solution is probably correct, or is at least more accurate than the solution obtained using the high-Reynolds-number model.

Relative velocity magnitude and turbulence kinetic energy contour plots in Figure 29 show the computed flow field in and around the rotor tip clearance gap, which has a height equal to 2.0 percent of span. The blade-to-blade contours in Figures 29(a) and 29(b) were calculated on a surface of revolution located spanwise near the middle of the clearance gap, and the contours in Figure 29(c) were calculated on a plane perpendicular to the axis of rotation at a midchord axial location (see Figs. 1 and 2). A comparison of the flow-field solutions obtained with the low- and high-Reynolds-number turbulence models reveals significant differences, but the impact on overall performance is small, and both solution sets indicate acceptable aerodynamic characteristics. Notable is the lack of turbulence for most of the tip flow region as computed using the low-Reynolds-number model. Of particular interest is the laminar-free shear layer between the tip jet and the flow just below the jet, on the suction side of the blade (see Fig. 29(c), left side of figure, right side of blade). The region below the shear layer is also laminar and involves a radial-tangential secondary flow that is considerably larger than that computed using the high-Reynolds-number turbulence model (compare to right side of Fig. 29(c)). The free shear layer itself exhibits a peculiar flow instability, mentioned earlier in the discussion of the CFD codes, which led to numerical difficulties for the AUSM+ upwind scheme. Evidence of the instability can be seen in Figure 29(a), in the left plot, but its existence is far more apparent in Figure 30, which shows entropy contours at a spanwise location about 0.001 in. above the blade tip. Property oscillations in the chordwise directions on the blade suction side reveal a wavetype instability for the low-Reynolds-number turbulence model (left plot), but not for the high-Reynolds-number model (right plot). The physical existence of such waves is uncertain, but their general appearance is reminiscent of that observed for various other types of unstable laminar-shear flows at the onset of turbulence (Ref. 17).

The rotor exit flow field at station 2b, located over one chord-length downstream of the rotor blade row, is shown in Figure 31, where contour plots of relative velocity magnitude, total-pressure rise, entropy rise, and turbulence kinetic energy are presented. Solution results for both the low- and high-Reynolds-number

[4]For the low-Reynolds-number turbulence model, boundary layer transition on the blade suction surface occurs at midchord, near the hub, and slightly upstream of the trailing edge near the tip.

turbulence models are included, and are generally similar. Close inspection reveals some differences in local flow features, but their significance is thought to be minimal. Note that the contour levels of relative velocity magnitude are the same as those in Figures 26 and 29, that total-pressure rise is in the stationary system, entropy rise is nondimensionalized by the gas constant, and turbulence kinetic energy is normalized by inlet kinetic energy (see discussion of Fig. 12). Rotation is in the direction indicated, so the wake-convecting flow field is moving counterclockwise, and the circumferential property variations are, in the stationary frame of reference, transient fluctuations. Tone noise is generated as this periodic unsteady flow interacts with the stator blades at the blade-passing frequency of the rotor. Although the stator blade row is actually located further downstream, it is close enough that the fluctuation patterns and amplitudes there should be similar to those existing at station 2b. No effort has been made as yet to predict the tone noise, and the acoustic complexities involved require specialized methods to do so. At the risk of oversimplification, however, it might be suggested that the total-pressure contours give at least some impression of the noise-generating wake intensity. It might be added that turbulence kinetic energy is also related to noise, but to noise of a different type, namely, broadband noise.

The stator blade-to-blade flow field in the stationary frame of reference is shown in Figure 32 for the same three stream surfaces of revolution used for the rotor: 85, 50, and 15 percent of passage flow. Velocity magnitude and turbulence kinetic energy contours are plotted, each using the same contour range for all three stream surfaces, and flow solutions for both the low- and high-Reynolds-number turbulence models are presented for comparison. Small red arrows in the turbulence kinetic energy plots indicate locations of laminar-to-turbulent transition on the blade surface, except at 85 percent of passage flow where the blade boundary layer is turbulent all the way from the leading edge. Line graphs showing chordwise distributions of stator blade surface pressure coefficient, C_p, for all three stream surfaces are provided in Figure 33. The reference values of static- and total-pressure for the pressure coefficient are based on the mixed-out average conditions at the blade leading edge. The top curve in each line graph corresponds to the blade pressure surface, the bottom curve corresponds to the blade suction surface, and the vertical spacing between the curves is related to the local aerodynamic loading (static pressure difference) at a particular chordwise location. In the contour plots, the lower blade surface corresponds to the suction surface.

The contour plots show the flow field downstream of the stator (in the diffuser duct) differs a lot for the three stream surfaces, but that the blade-to-blade flow field within the stator blade row itself is basically the same, except near trailing edge on the suction surface. Differences due to the turbulence model are noticeable, but of only minor significance overall. The general similarity in the stator blade-to-blade flow is also seen in the pressure coefficient distributions, which reveal that the blade loading is fairly constant over the front 40 percent of the blade, and then decreases gradually to the trailing edge. Most of the flow diffusion (deceleration and static-pressure rise) on the blade suction surface takes place from about 40 to 70 percent of blade chord. On the blade suction surface near the hub and tip, the boundary layer separates before reaching the trailing edge; separation near the tip occurs at around 65 percent of chord and near the hub at around 75 percent of chord. The tip separation, however, is disproportionately more severe, as the contour plots suggest. On the suction surface near midspan there is no boundary-layer separation at the trailing edge, although for the low-Reynolds-number turbulence model there is a small laminar separation bubble, followed by transition to turbulence, at around 60 percent of chord.

Contour plots showing the stator exit flow field at station 3c, located over one chord-length downstream of the stator blade row, are provided in Figure 34. Plots of velocity magnitude, total-pressure rise, entropy rise, turbulence kinetic energy, and axial velocity are presented for both the low- and high-Reynolds-number turbulence models. Note that the contour levels of velocity magnitude are the same as those in Figure 32, that entropy rise is nondimensionalized by the gas constant, and turbulence kinetic energy is normalized by inlet kinetic energy (see discussion of Fig. 12). The legend for axial velocity is the same as for velocity magnitude, so it does not include values below zero, even though negative axial velocities are included in the contour plot. As has generally been the case, the turbulence-model-related differences are relatively minor.

The three-dimensional structure and extent of the tip endwall separation in the annular diffuser duct can be readily inferred from the contour plots in Figure 34 and by comparing the velocity magnitude plots in

Figure 34(a) to those in Figure 32. From the structure of the separation it is apparent that both wake and endwall low-momentum fluids are contained in it. The exact region where the axial velocity is negative (indicating upstream fluid migration) is outlined in Figure 34(c) by the thick black contour corresponding to an axial velocity of zero. As the contour plots in Figures 34(a) (bottom) and 34(b) (top) show, this region is also associated with a relatively low total-pressure rise and a relatively high entropy rise. The location and extent of the reverse-flow region further upstream, at station 3b, can be seen in Figure 35, which also shows axial velocity contours and more clearly reveals the wake-endwall nature of the separation.

Summary and Concluding Remarks

The aerodynamics of a cabin ventilation fan designed by Hamilton Sundstrand was successfully simulated using CFD codes, and the computed solutions were analyzed to quantify various aspects of the fan aerodynamics and performance. Four simulations were performed at the design rotational speed: two at the design flow rate and two at off-design flow rates. The two design-flow simulations involved different versions of the turbulence model: one more suitable for high-Reynolds-number flows and the other for low-Reynolds-number flows. Results show that the turbulence model version had only a small impact on the computed aerodynamics, in spite of significant differences in the turbulence solution.

Fan performance quantities derived from the computed flow fields are in generally good agreement with stated design goals. The design, however, seems to leave some room for aerodynamic improvement, especially in the exit diffuser. The rotor flow is aerodynamically clean, as is also the stator flow, except near the trailing edge at the stator tip where boundary layer separation on the suction surface is somewhat excessive. In the annular diffuser downstream of the stator, the total-pressure loss is higher than what might be expected, and the flow in the tip region involves a substantial wake-endwall separation. The total-pressure loss for the diffuser exit discharge also seems to be higher than what should be practically achievable. In the fan inlet the flow is well behaved, although there is a small separation above the sharp lip on the hub/spinner nose. More importantly, the high curvature of the nose surface produces an overexpansion of the flow, which increases the hub static-pressure rise across the rotor significantly beyond what is really necessary.

References

1. Munch, C.L.: Noise Reduction Study of Orbiting Workshop Ventilation Fans. NASA CR–102287 (Wyle Laboratories Research Staff Technical Memorandum 69–4), 1969.
2. Misoda, John; and Magliozzi, Bernard: Fan and Pump Noise Control. NASA CR–128986 (Hamilton Standard SVHSER 6183), 1973.
3. Lovell, John S.; and Magliozzi, Bernard: Design Guidelines for Quiet Fans and Pumps for Space Vehicles. NASA/CR—2008-215427 (Hamilton Standard SVHSER 6225), 2008.
4. Chima, R.V.: Viscous Three-Dimensional Calculations of Transonic Fan Performance. CFD Techniques for Propulsion Applications, AGARD Conference Proceedings CP510 (NASA TM–103800), AGARD, 1992, pp. 21–1 to 21–19.
5. Chima, R.V.; and Yokota, J.W.: Numerical Analysis of Three-Dimensional Viscous Flows in Turbomachinery. AIAA J., vol. 28, no. 5, 1990, pp. 798–806.
6. Tweedt, Daniel L.; and Chima, Rodrick V.: Rapid Numerical Simulation of Viscous Axisymmetric Flow Fields. NASA TM–107103 (AIAA–96–0449), 1995.
7. Tweedt, Daniel L.; Chima, Rodrick V.; and Turkel, Eli: Preconditioning for Numerical Simulation of Low Mach Number Three-Dimensional Viscous Turbomachinery Flows. NASA TM–113120 (ICOMP–97–11 and AIAA–97–1828), 1997.
8. Tatsumi, S.; Martinelli, L.; and Jameson, A.: Design, Implementation, and Validation of Flux Limited Schemes for the Solution of the Compressible Navier-Stokes Equations. AIAA Paper 94–0647, 1994.
9. Tatsumi, S.; Martinelli, L.; and Jameson, A.: A New High Resolution Scheme for Compressible Viscous Flows With Shocks. AIAA Paper 95–0466, 1995.

10. Chima, R.V.; and Liou, M.-S.: Comparison of the AUSM+ and H-CUSP Schemes for Turbomachinery Applications. AIAA Paper AIAA–2003–4120 (NASA/TM—2003-212457), 2003.
11. Chima, R.V.: Swift—Multiblock Analysis Code for Turbomachinery. User's Manual and Documentation, Version 300, 2003.
12. Menter, R.F.: Two-Equation Eddy-Viscosity Turbulence Models for Engineering Applications. AIAA J. (NASA TM–111958), vol. 32, no. 8, 1994, pp. 1598–1605.
13. Giles, Michael B.: Nonreflecting Boundary Conditions for Euler Equation Calculations. AIAA J., vol. 28, no. 12, 1990, pp. 2050–2058.
14. Giles, Michael: UNSFLO: A Numerical Method for the Calculation of Unsteady Flow in Turbomachinery. GTL Report No. 205, 1991, pp. 45–56.
15. Wilcox, David C.: Turbulence Modeling for CFD. Third ed., DCW Industries, Inc., La Cañada, CA, 2006.
16. Chima, R.V.: TCGRID 3–D Grid Generator for Turbomachinery. User's Manual and Documentation, Version 300, 2003.
17. Van Dyke, Milton: An Album of Fluid Motion. The Parabolic Press, Stanford, CA, 1982, pp. 60–87.

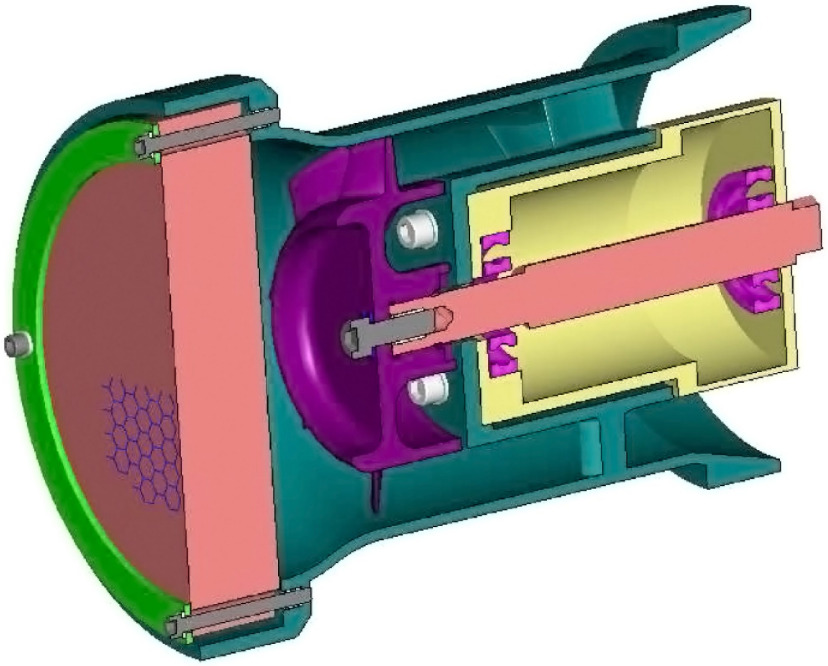

Figure 1.—Three-dimensional cutaway view of cabin ventilation fan assembly.

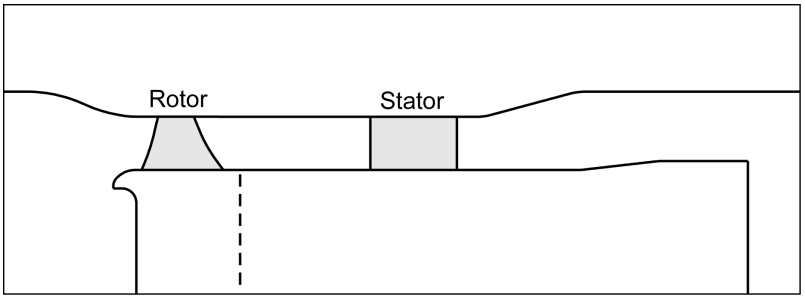

Figure 2.—Fan cross section.

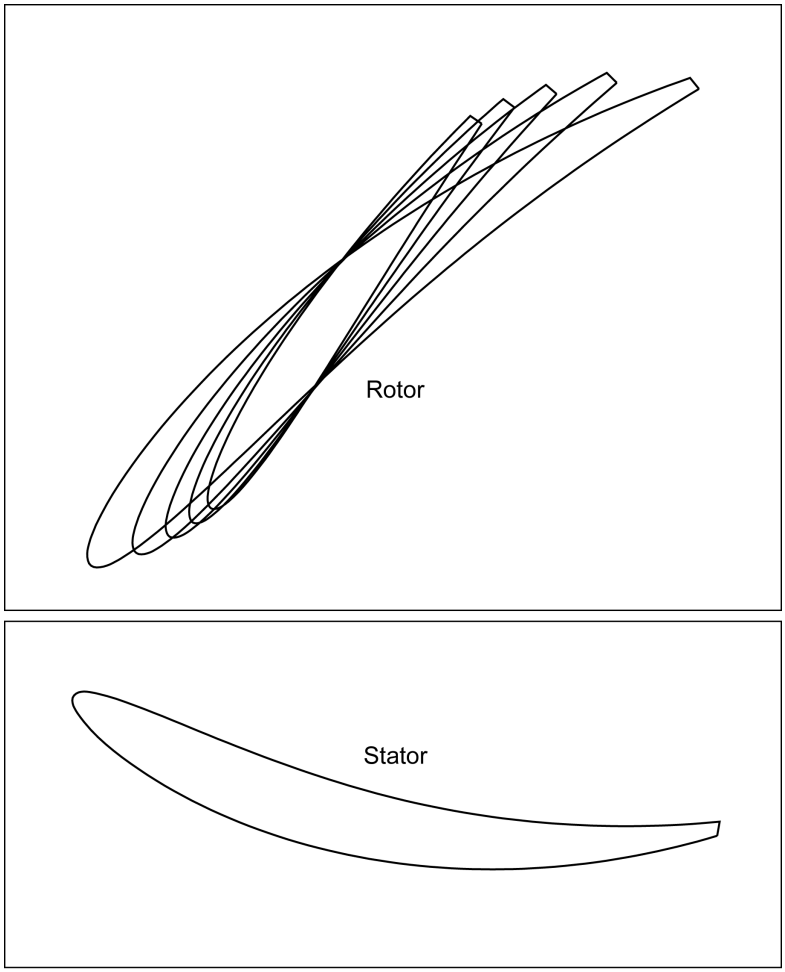

Figure 3.—Rotor and stator vane sections.

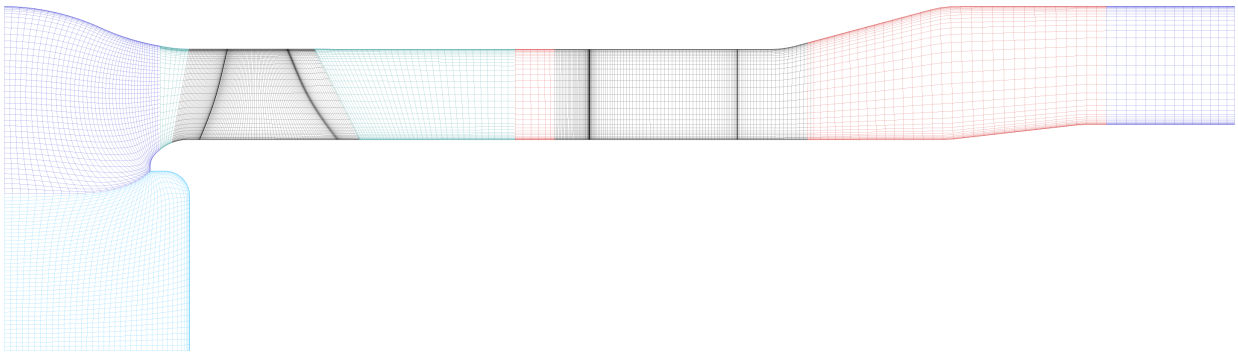

Figure 4.—Meridional view of fan system grid blocks.

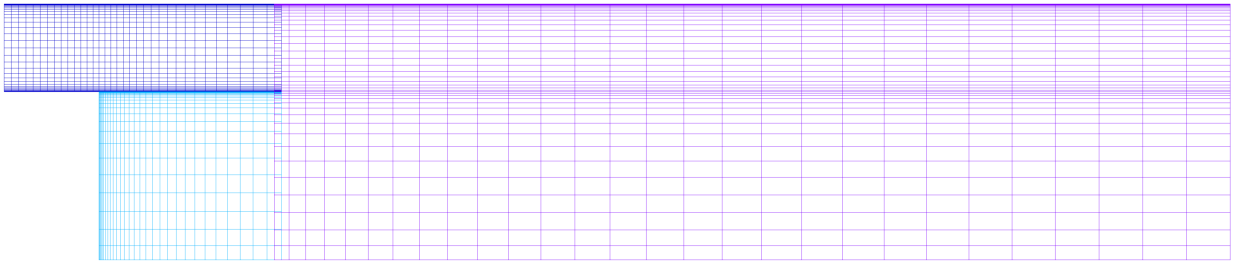

Figure 5.—System exit grid blocks.

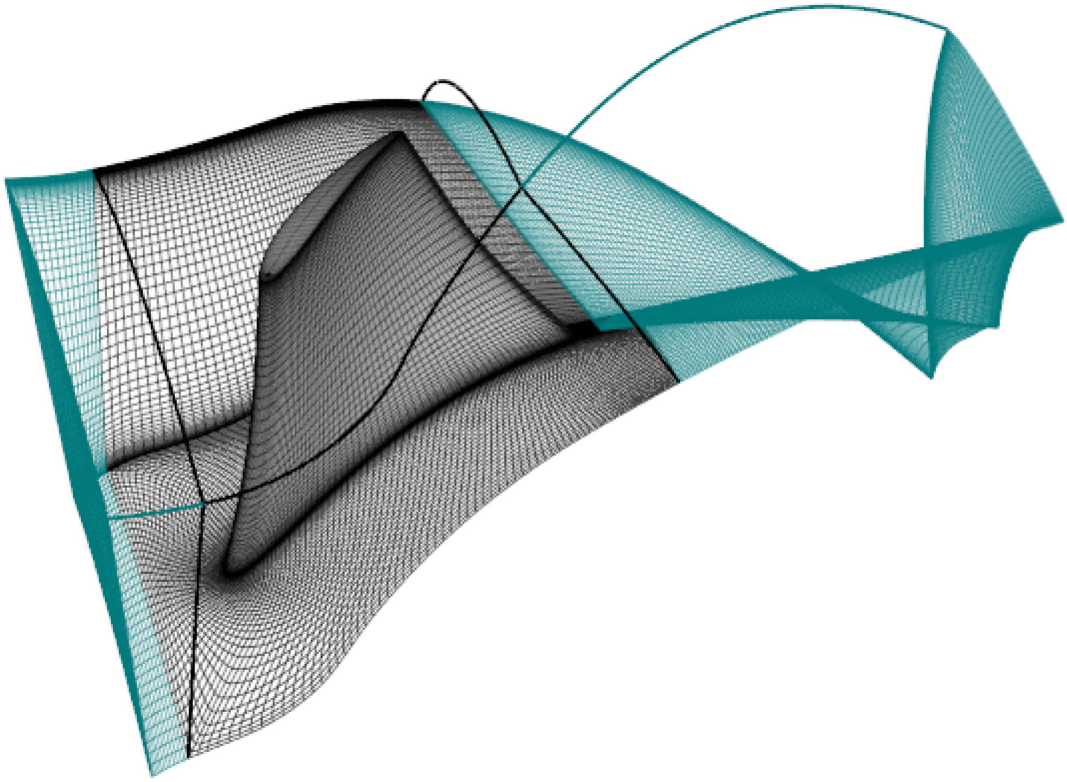

Figure 6.—Three-dimensional view of rotor grid blocks.

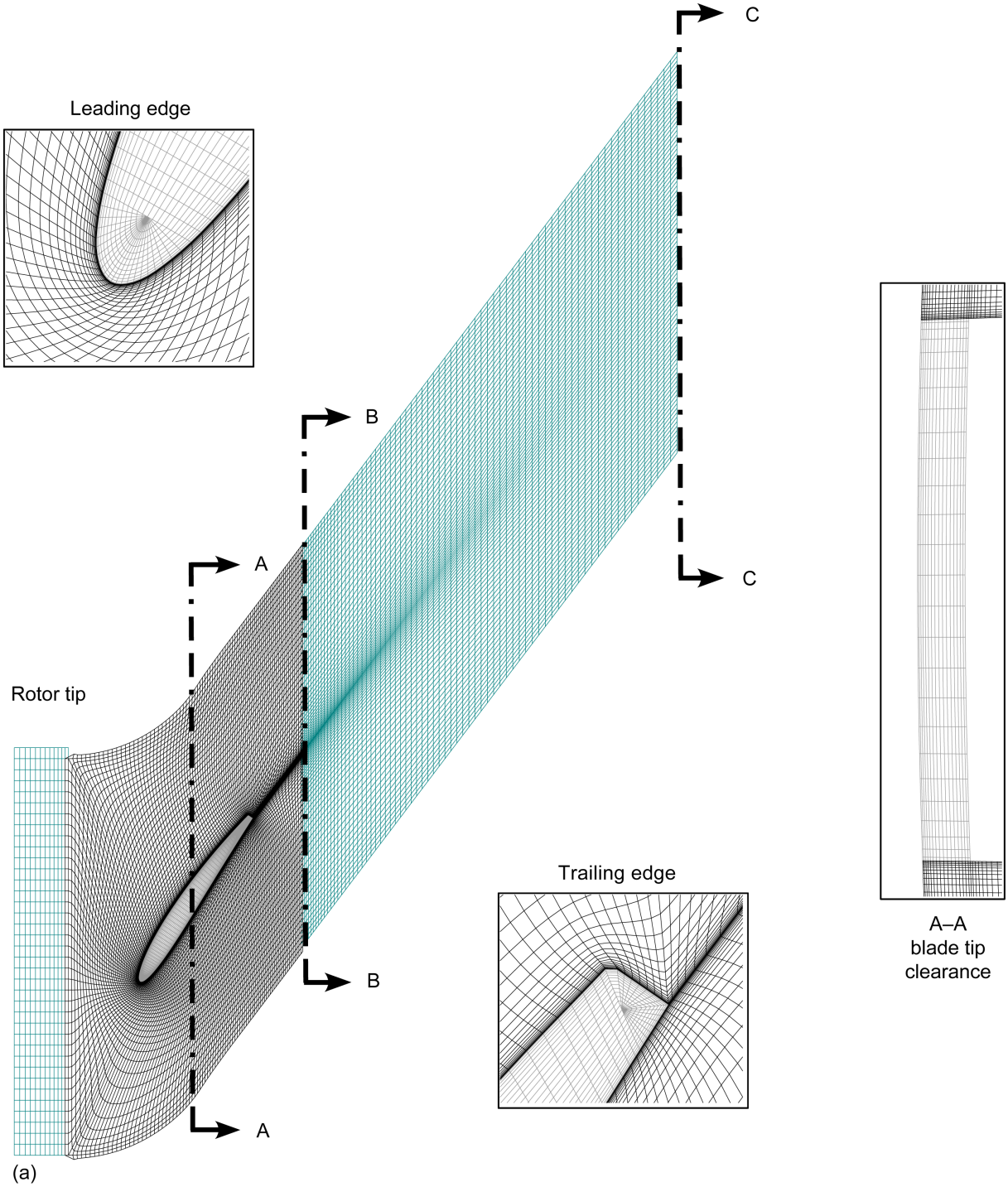

Figure 7.—Axial-circumferential (blade-to-blade) mesh plot of the rotor grid. (a) Rotor grid at the blade tip. (b) Rotor grid at the hub.

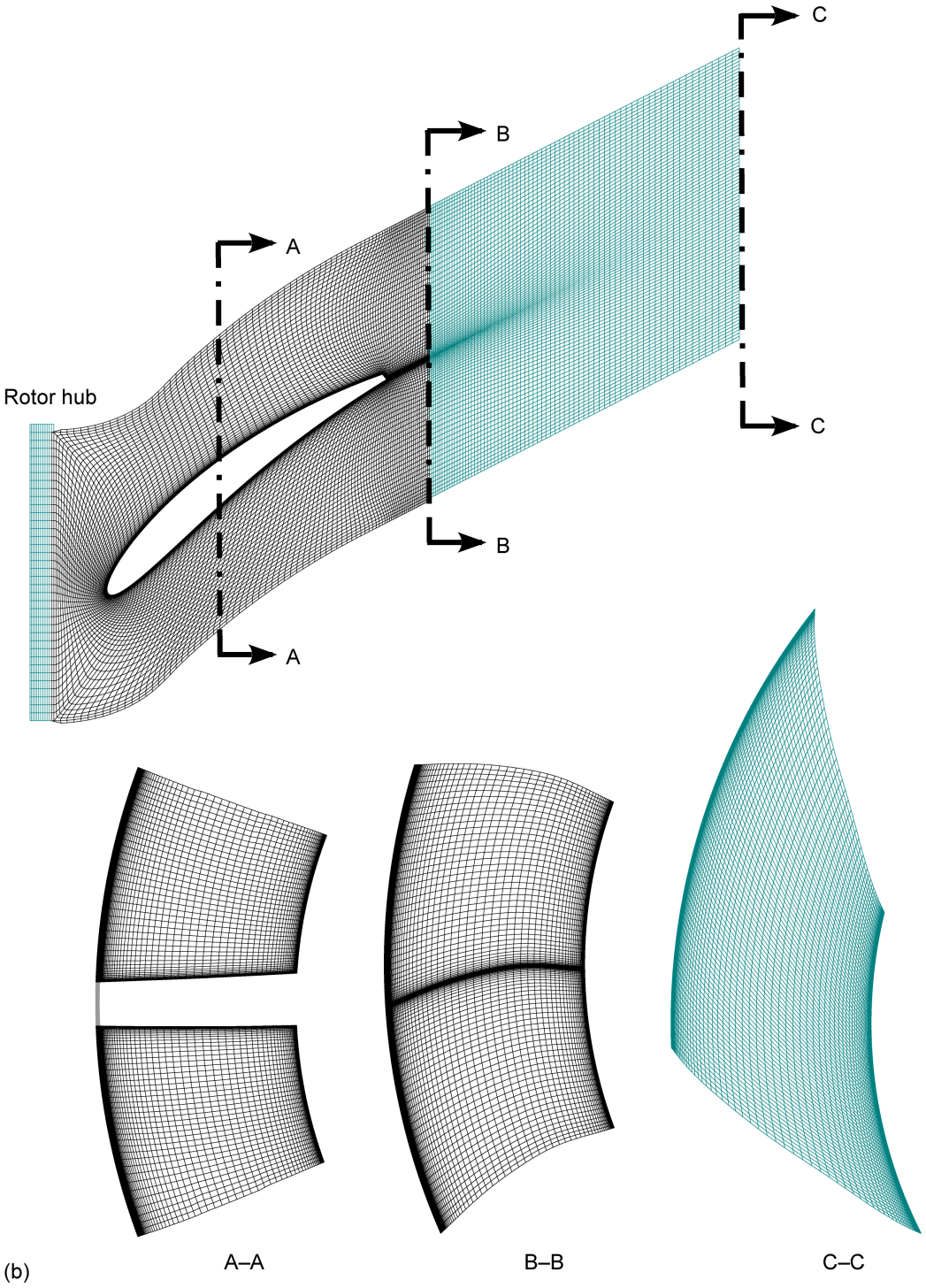

Figure 7.—Concluded. (b) Rotor grid at the hub.

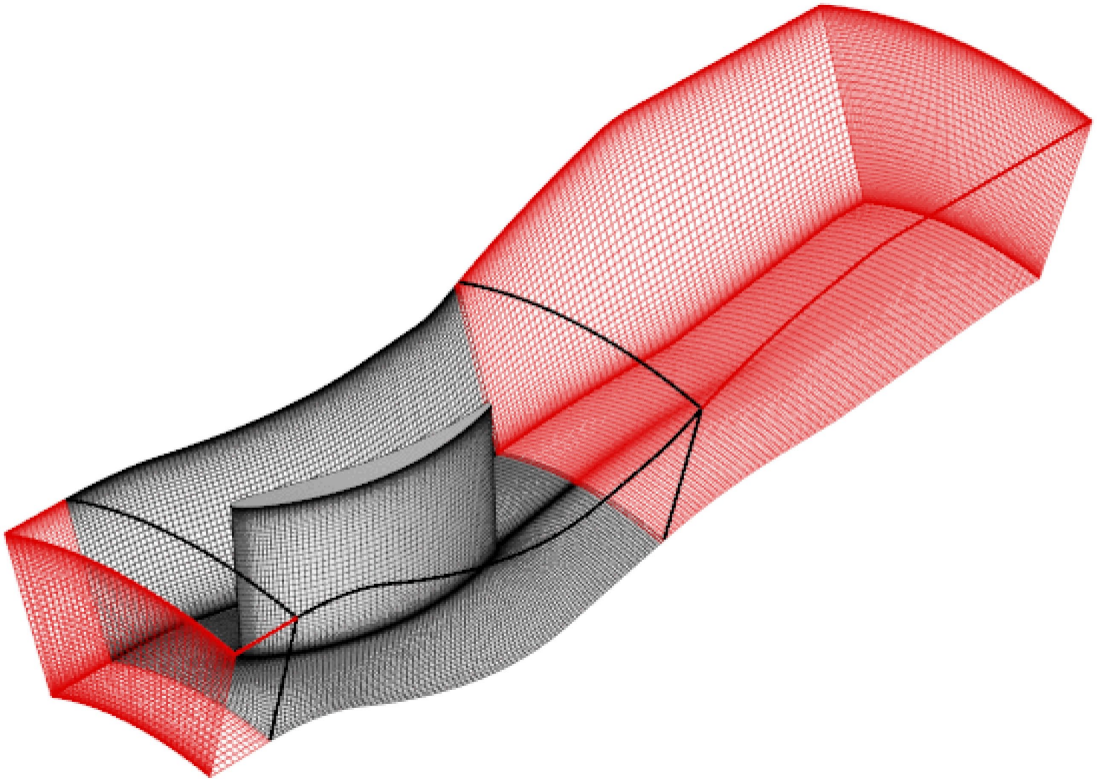

Figure 8.—Three-dimensional view of stator grid blocks.

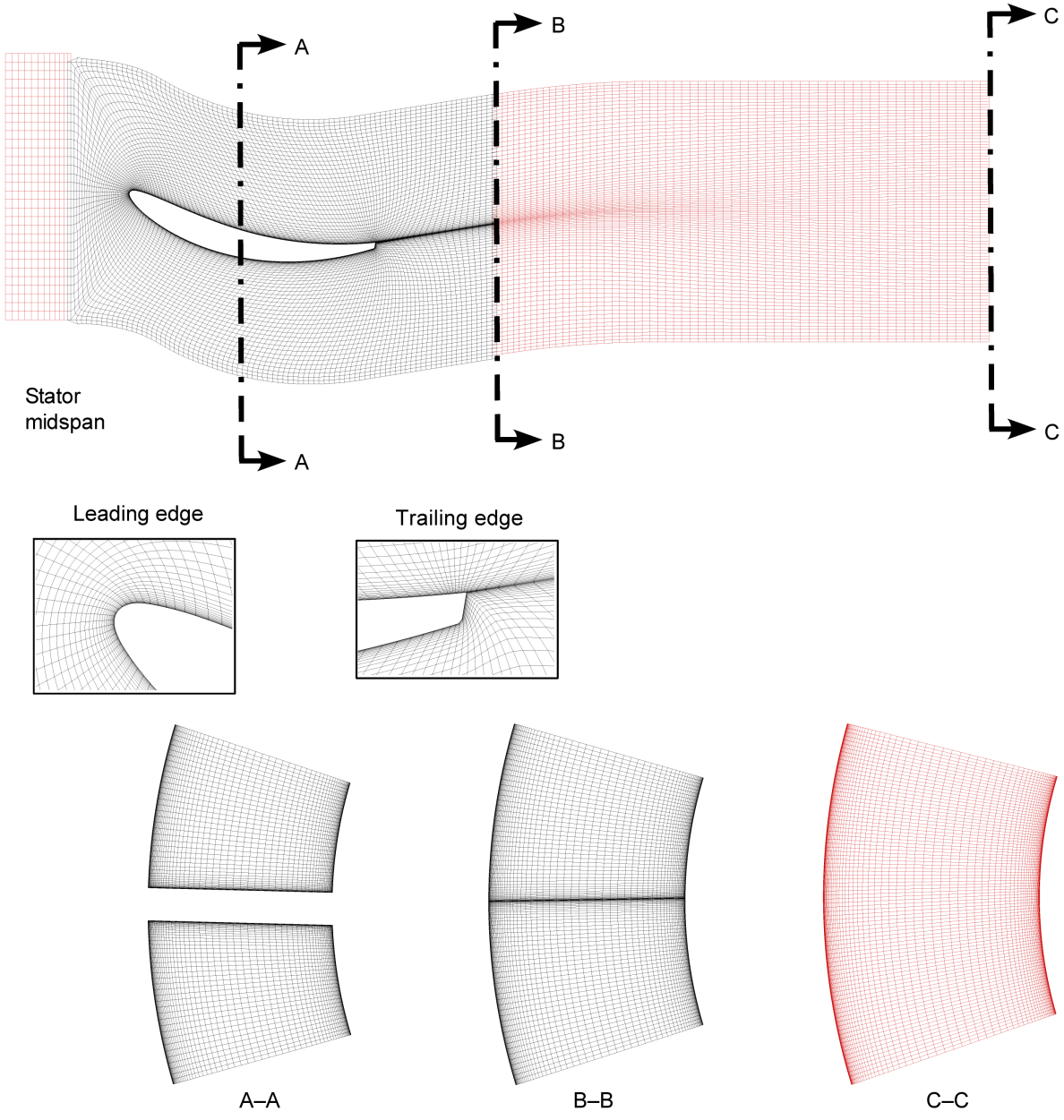

Figure 9.—Stator grid mesh plots.

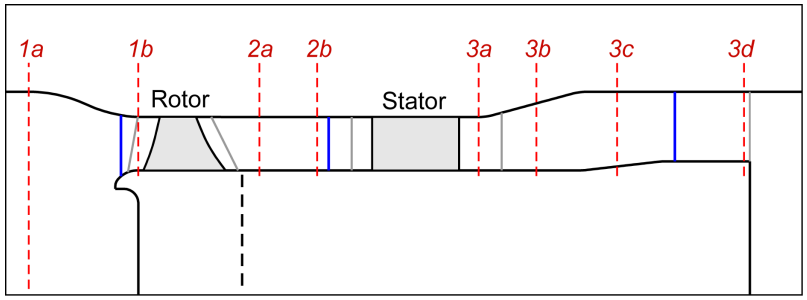

Figure 10.—Axial station locations.

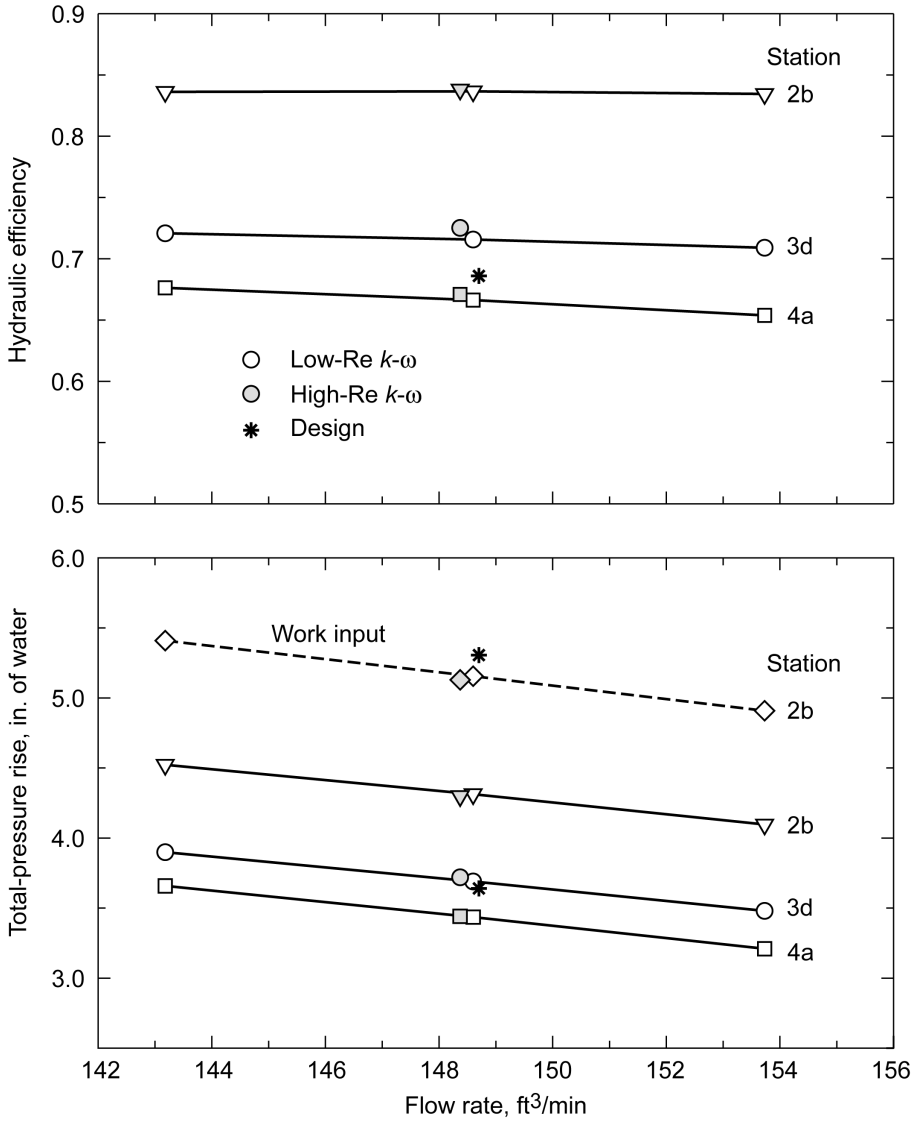

Figure 11.—Fan performance map.

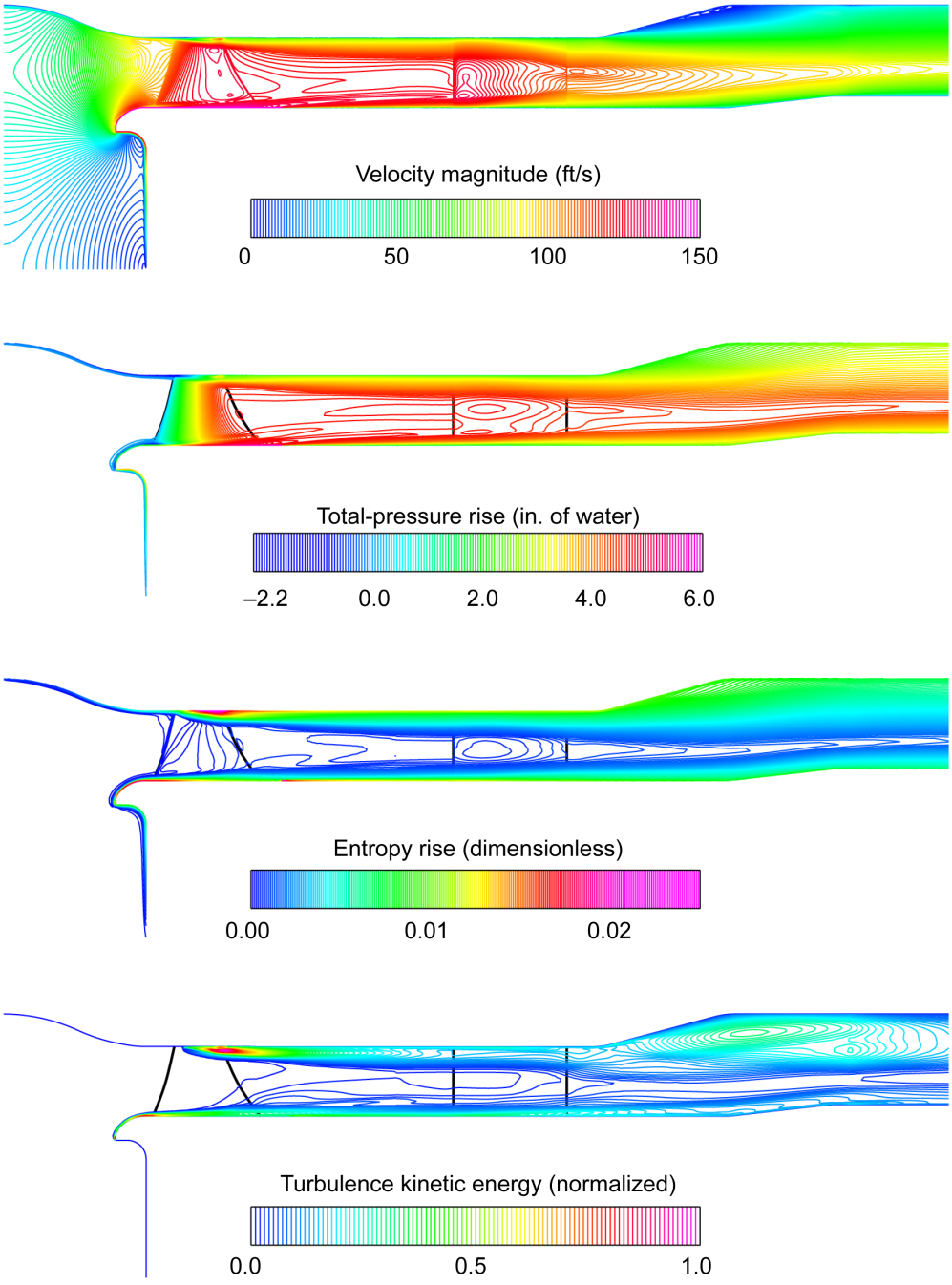

Figure 12.—Computed fan system flow field for design operating conditions; circumferentially averaged flow; low-Re turbulence model.

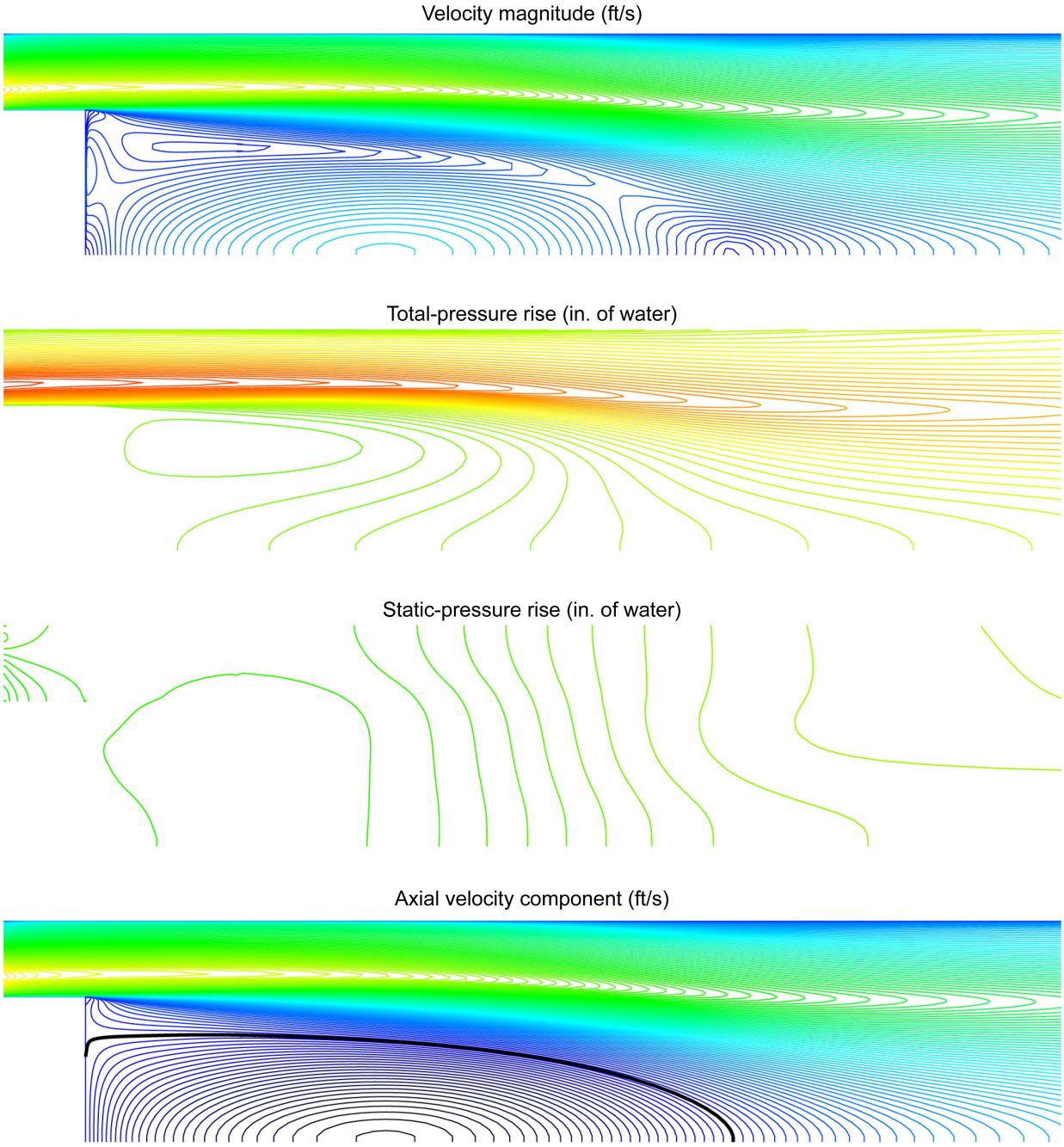

Figure 13.—Computed system exit flow field for design operating conditions; low-Re turbulence model.

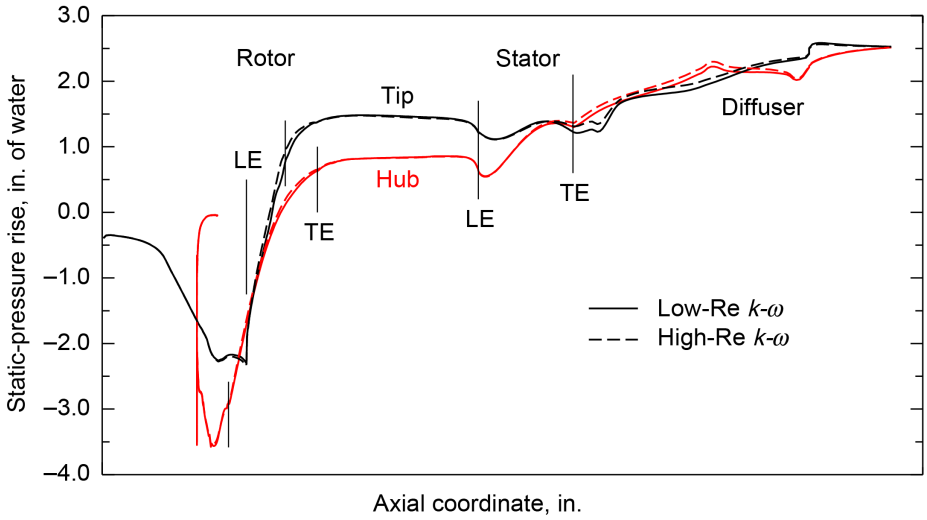

Figure 14.—Fan system endwall static-pressure rise for design operating conditions (circumferentially averaged flow).

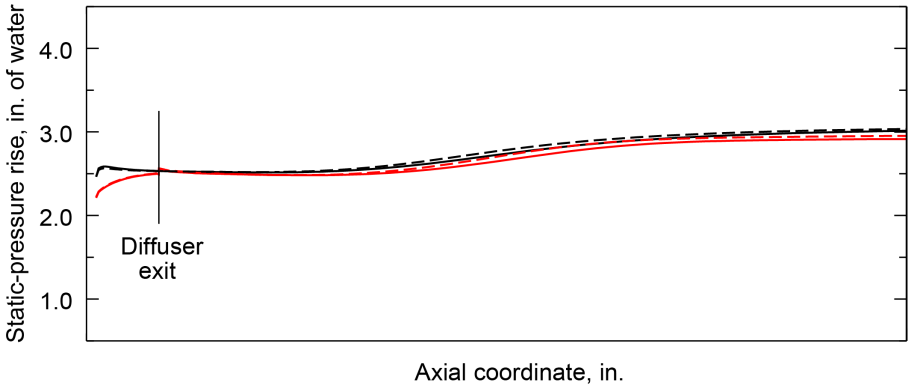

Figure 15.—System exit endwall static-pressure rise for design operating conditions.

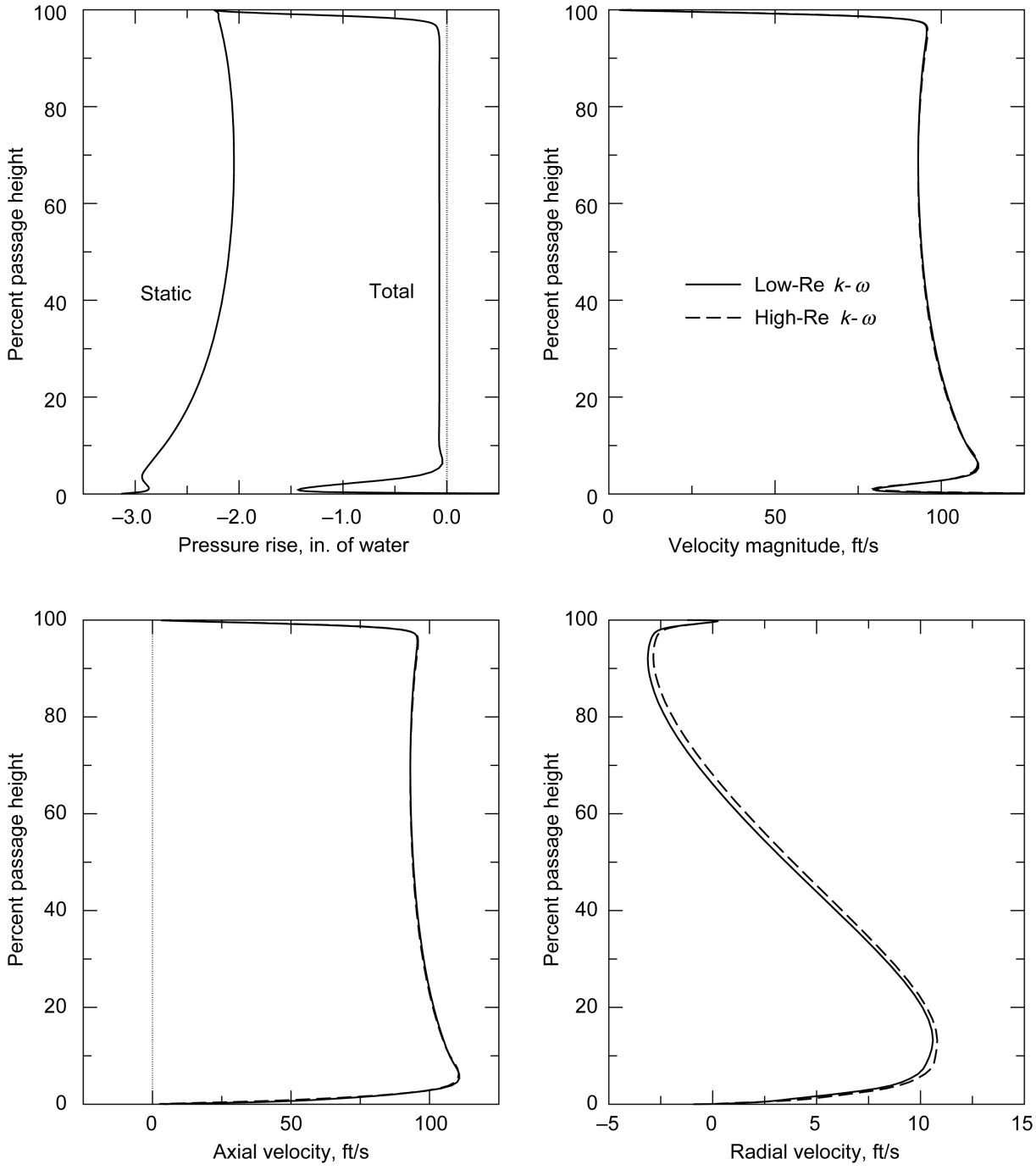

Figure 16.—Station 1b flow property profiles (circumferentially averaged flow).

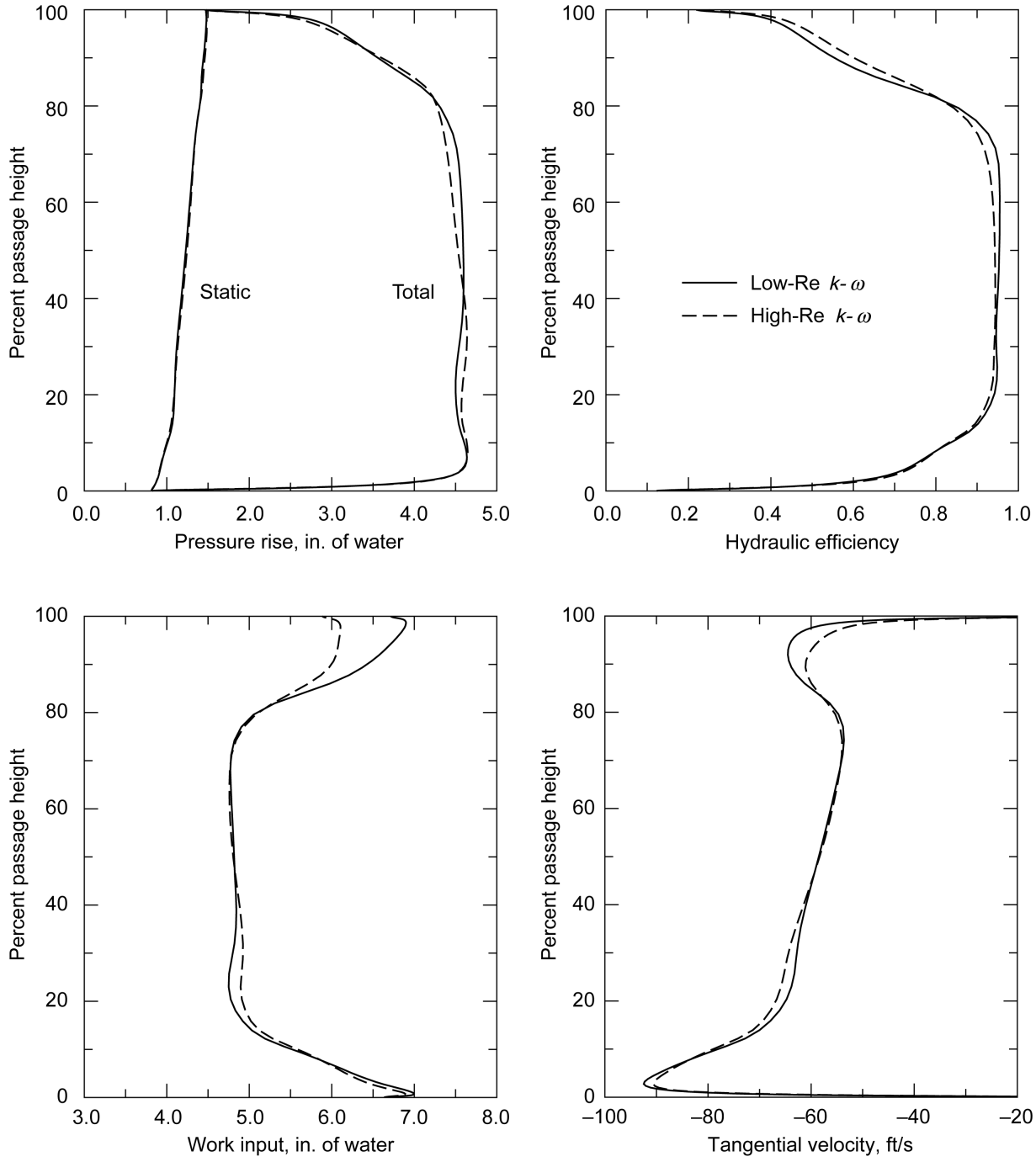

Figure 17(a).—Station 2a flow property profiles (circumferentially averaged flow).

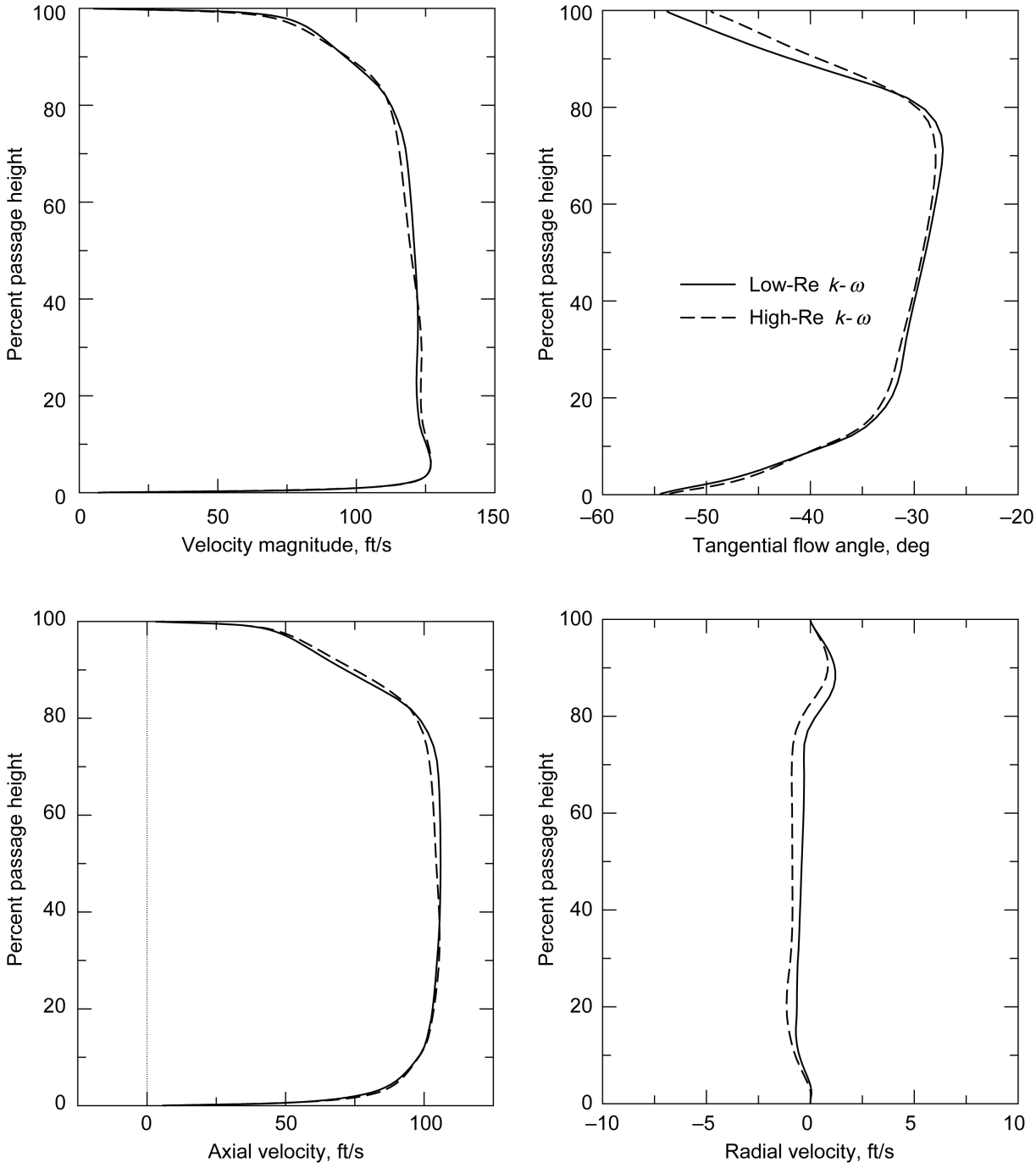

Figure 17(b).—Station 2a flow property profiles (circumferentially averaged flow).

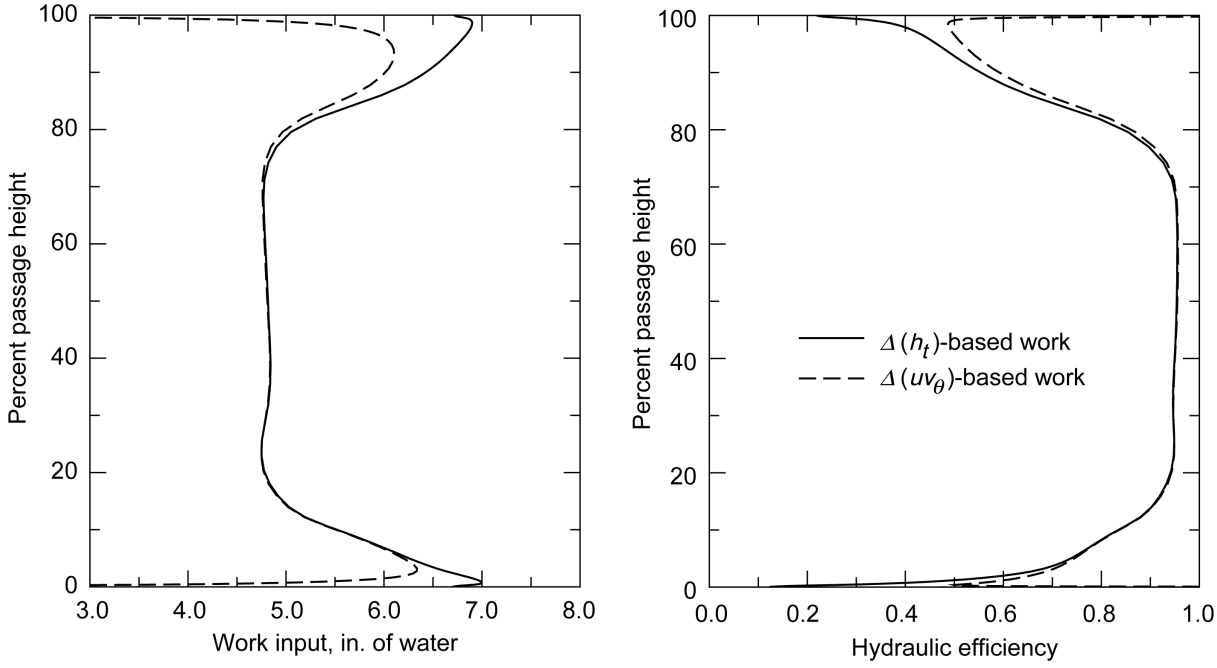

Figure 18.—Comparison of thermodynamic- and kinematic-based distributions of work input and hydraulic efficiency at station 2a (circumferentially averaged flow).

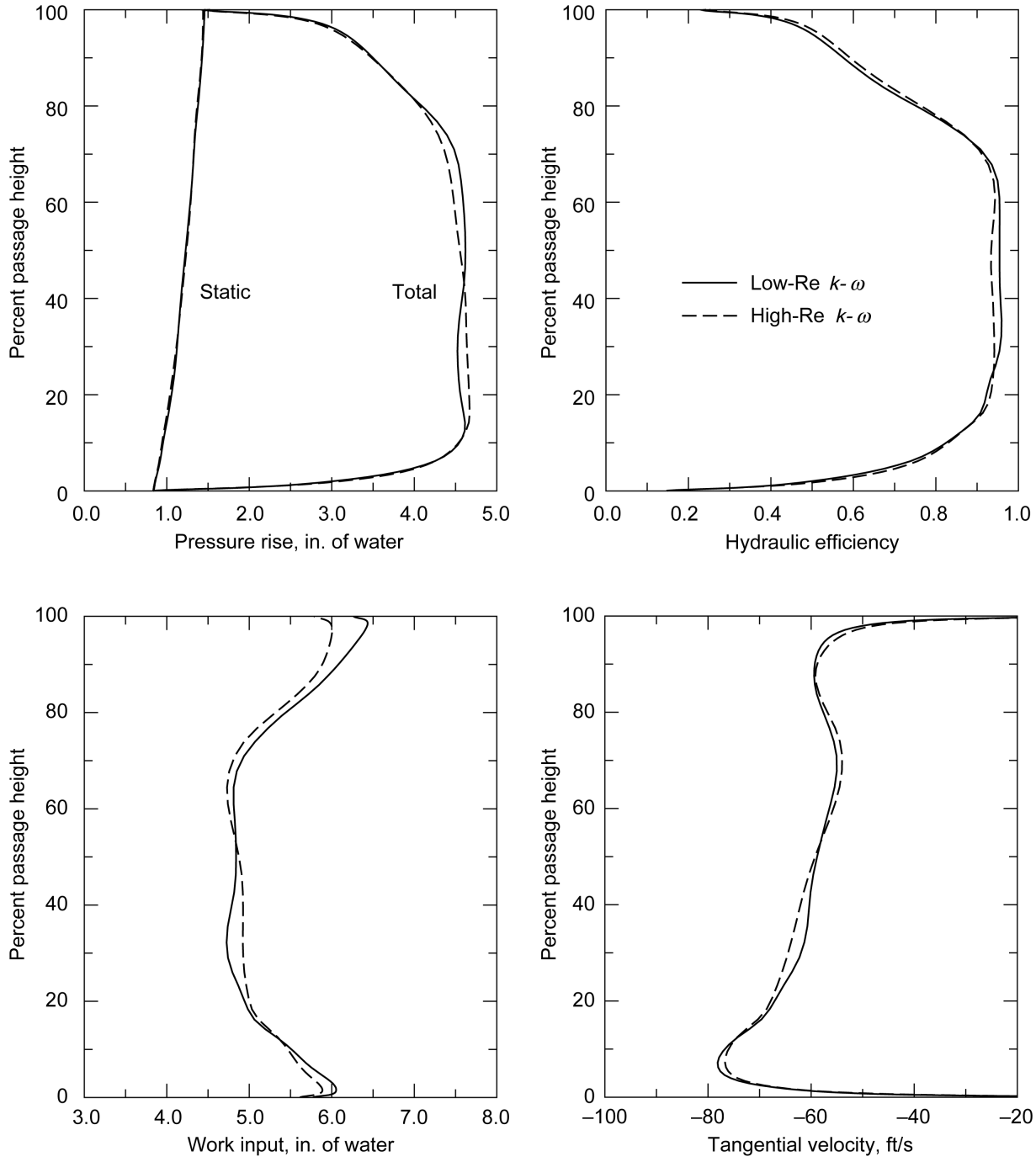

Figure 19(a).—Station 2b flow property profiles (circumferentially averaged flow).

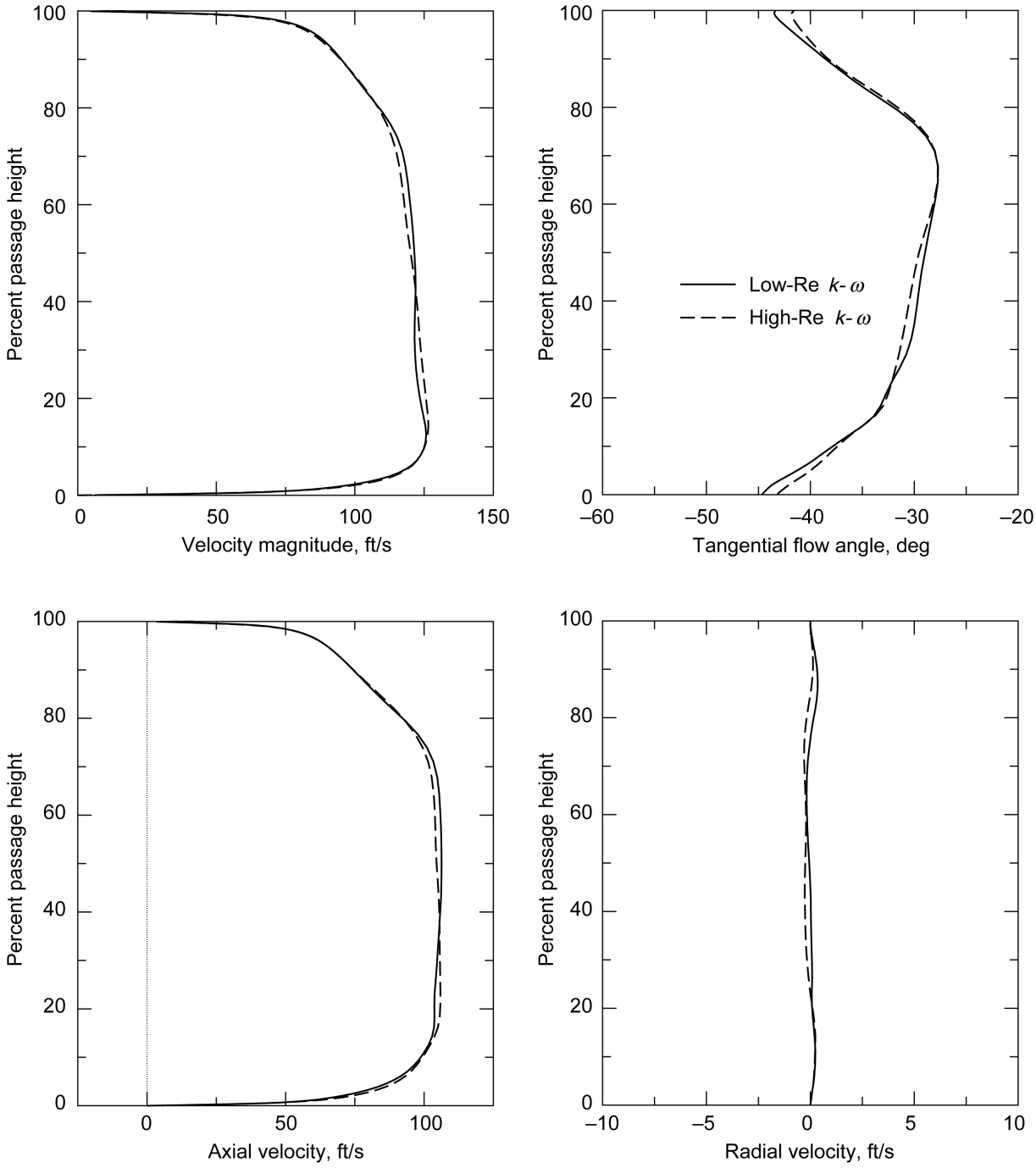

Figure 19(b).—Station 2b flow property profiles (circumferentially averaged flow).

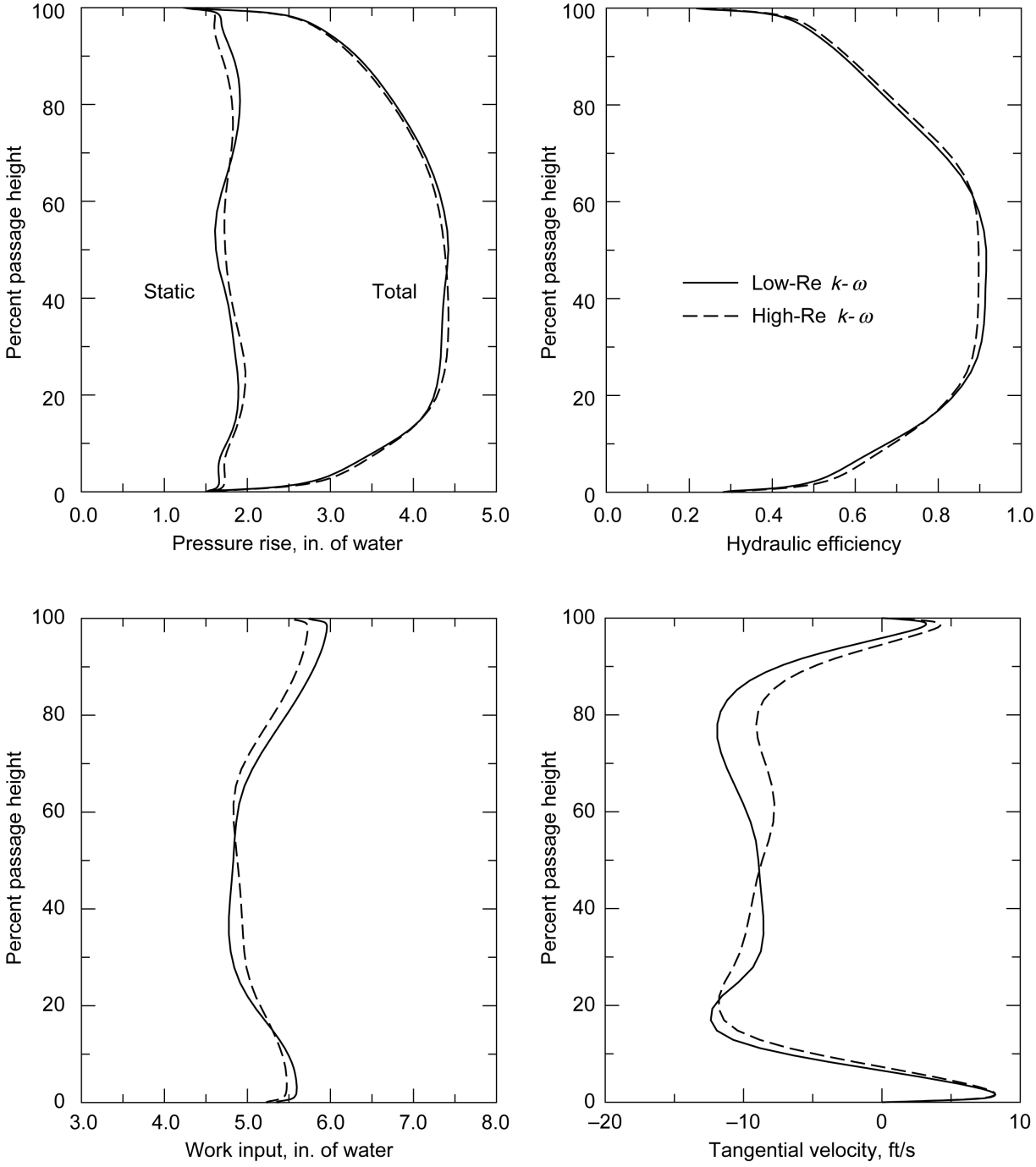

Figure 20(a).—Station 3a flow property profiles (circumferentially averaged flow).

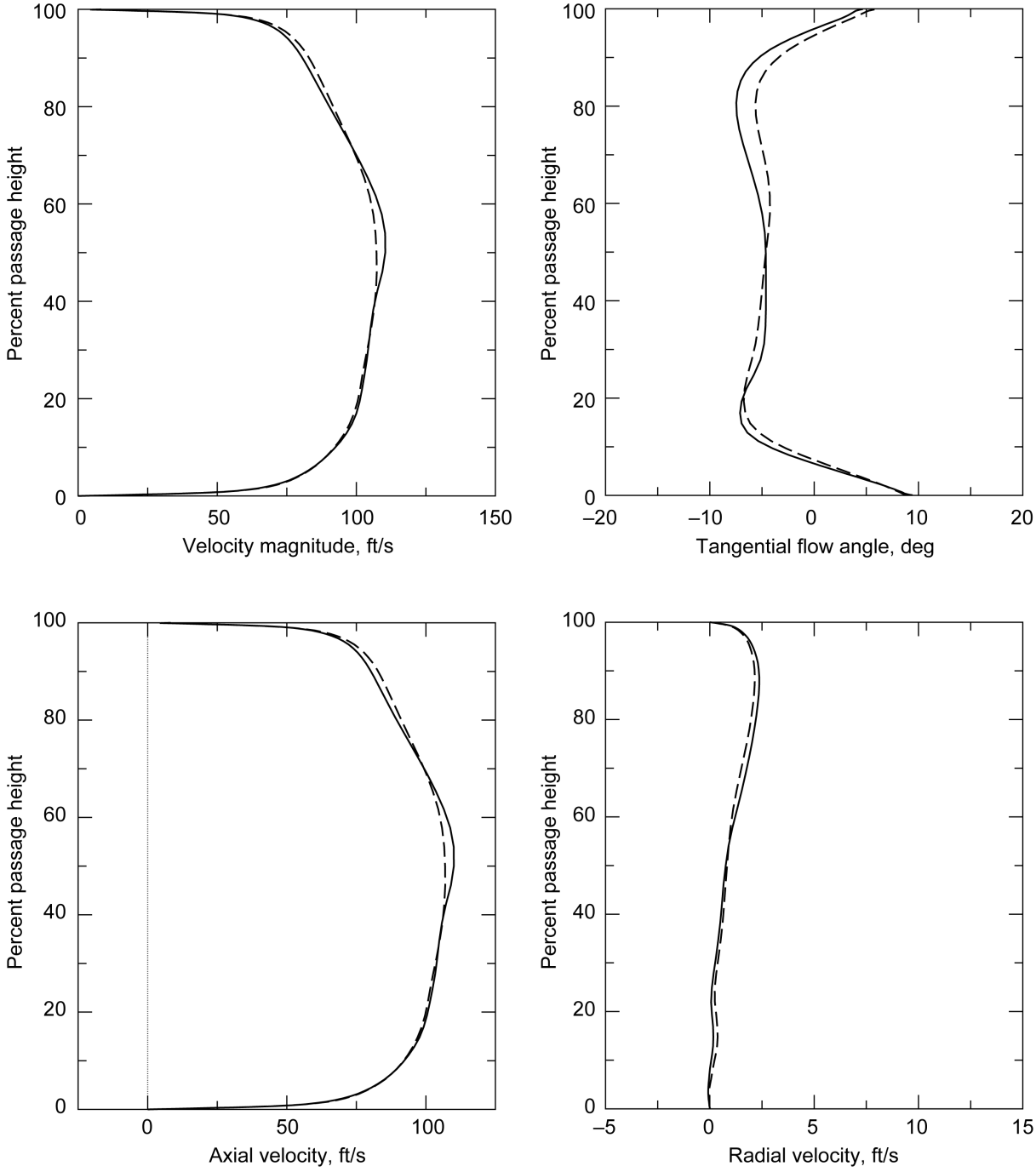

Figure 20(b).—Station 3a flow property profiles (circumferentially averaged flow).

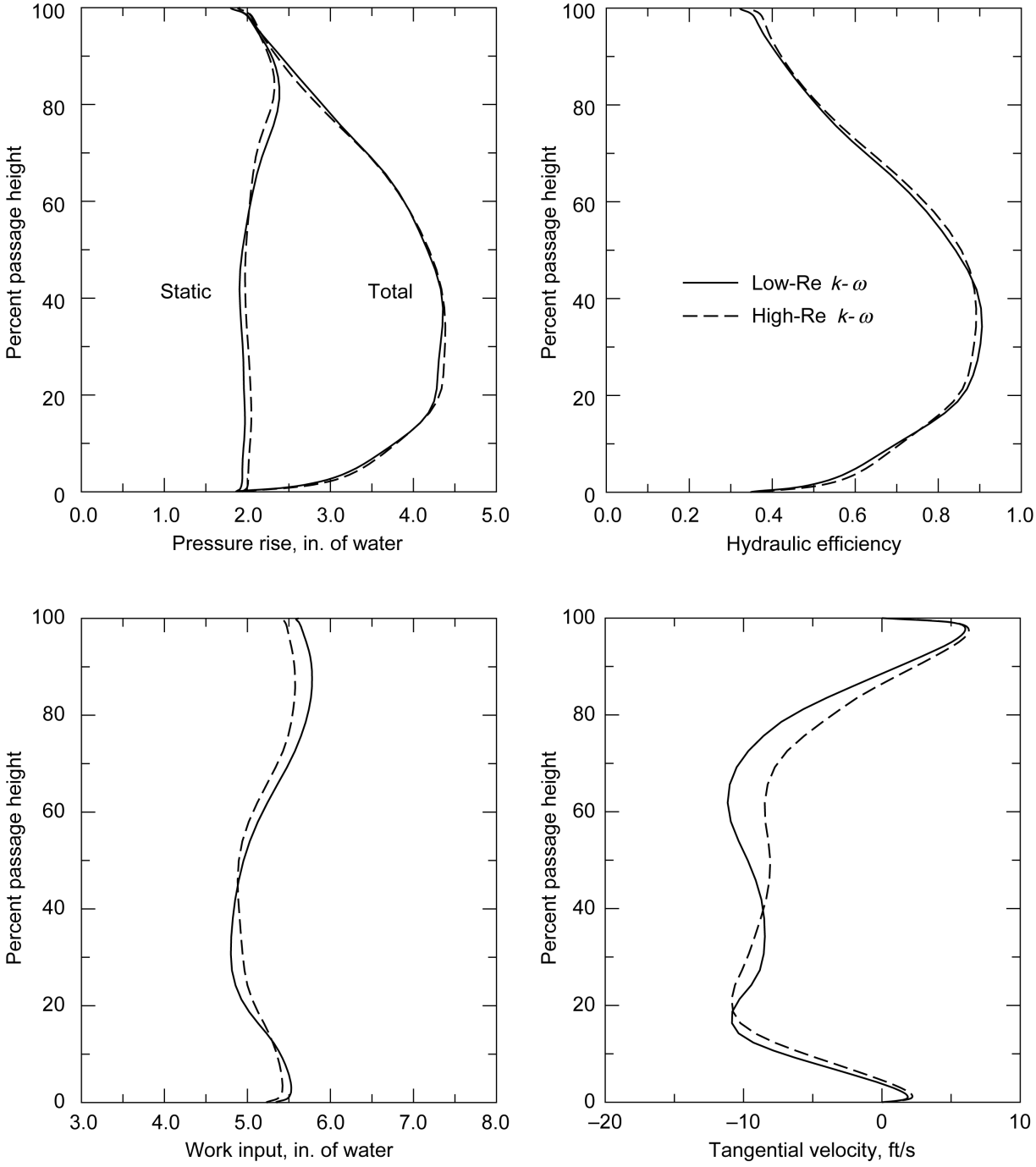

Figure 21(a).—Station 3b flow property profiles (circumferentially averaged flow).

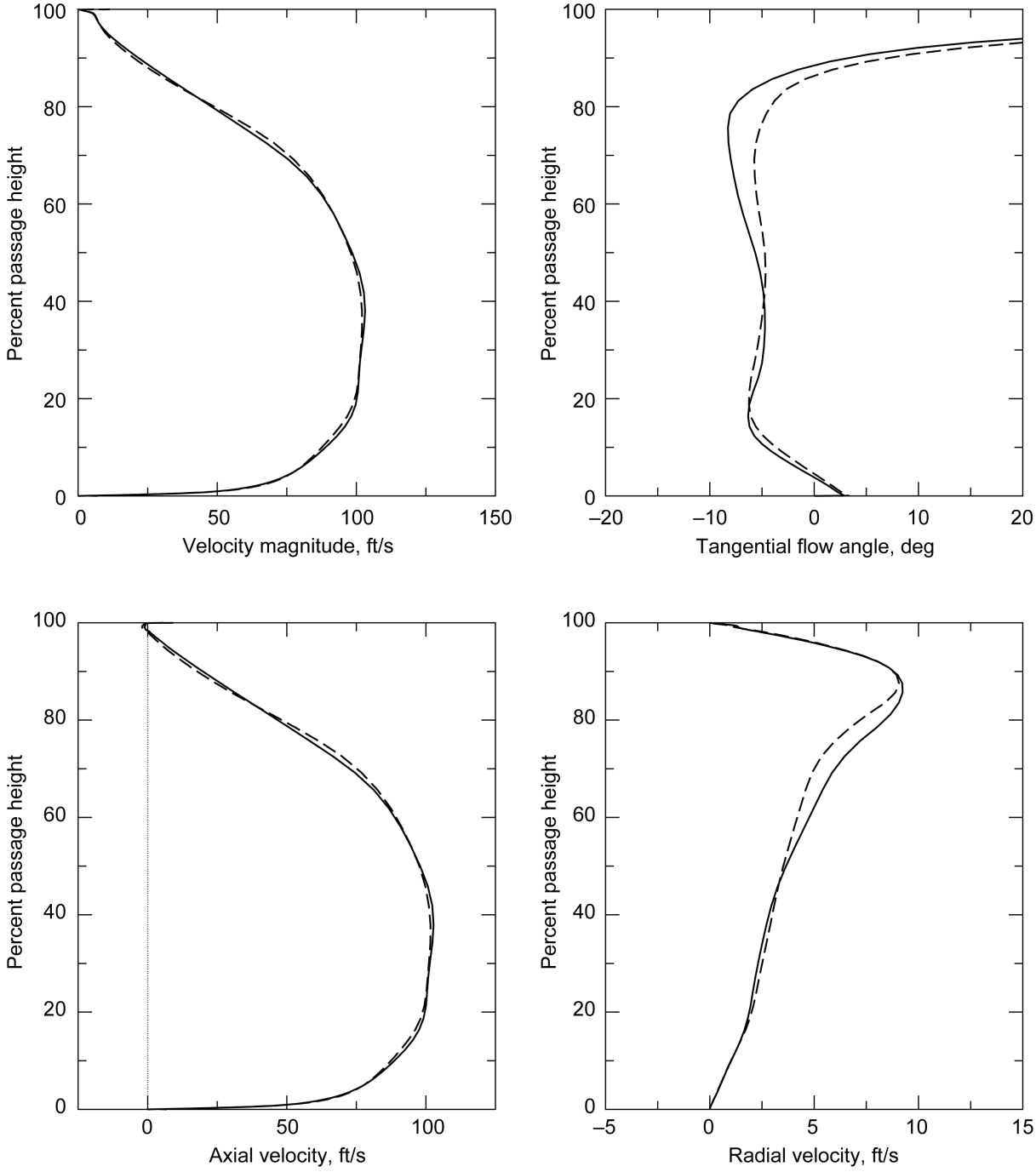

Figure 21(b).—Station 3b flow property profiles (circumferentially averaged flow).

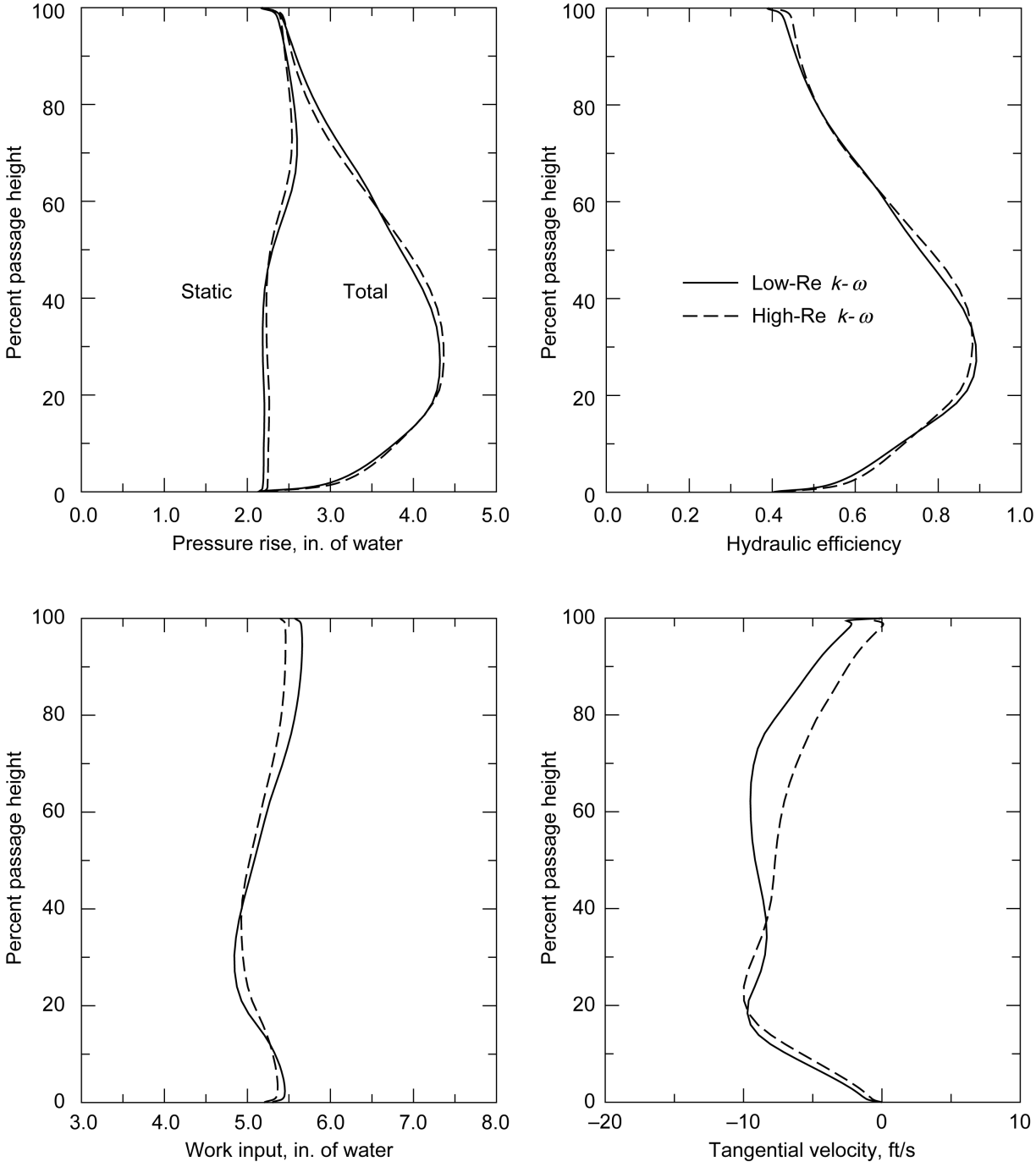

Figure 22(a).—Station 3c flow property profiles (circumferentially averaged flow).

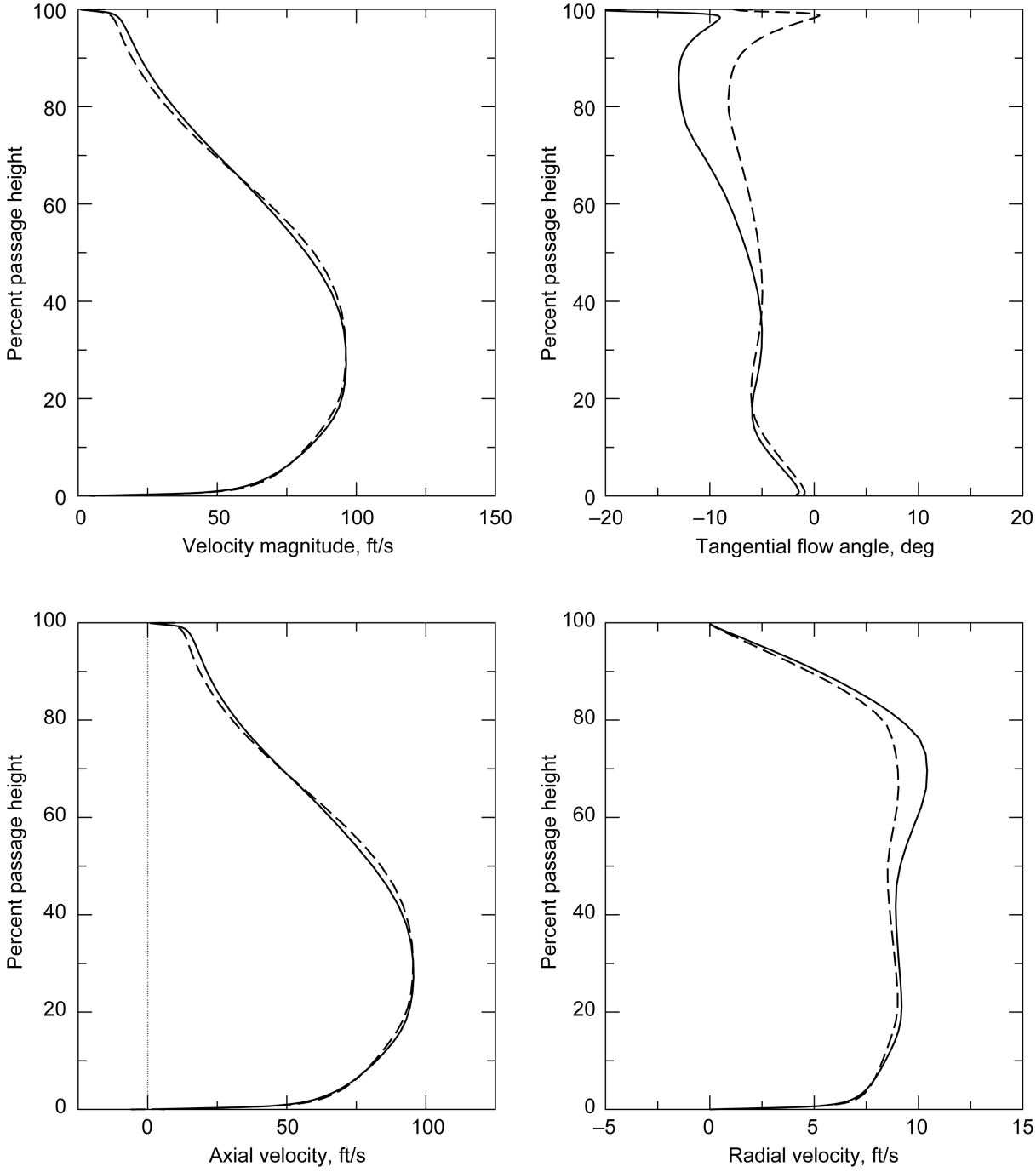

Figure 22(b).—Station 3c flow property profiles (circumferentially averaged flow).

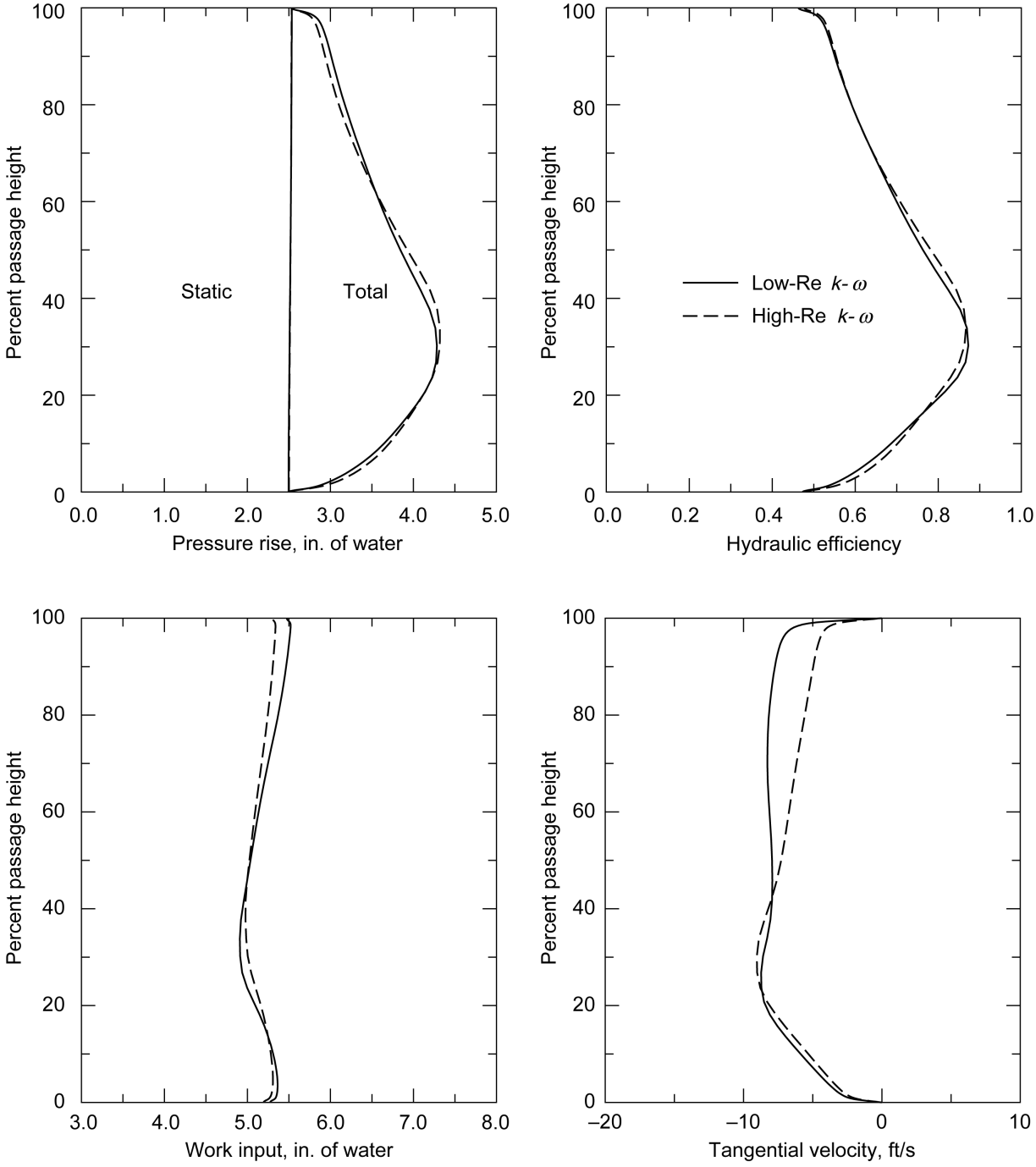

Figure 23(a).—Station 3d flow property profiles (circumferentially averaged flow).

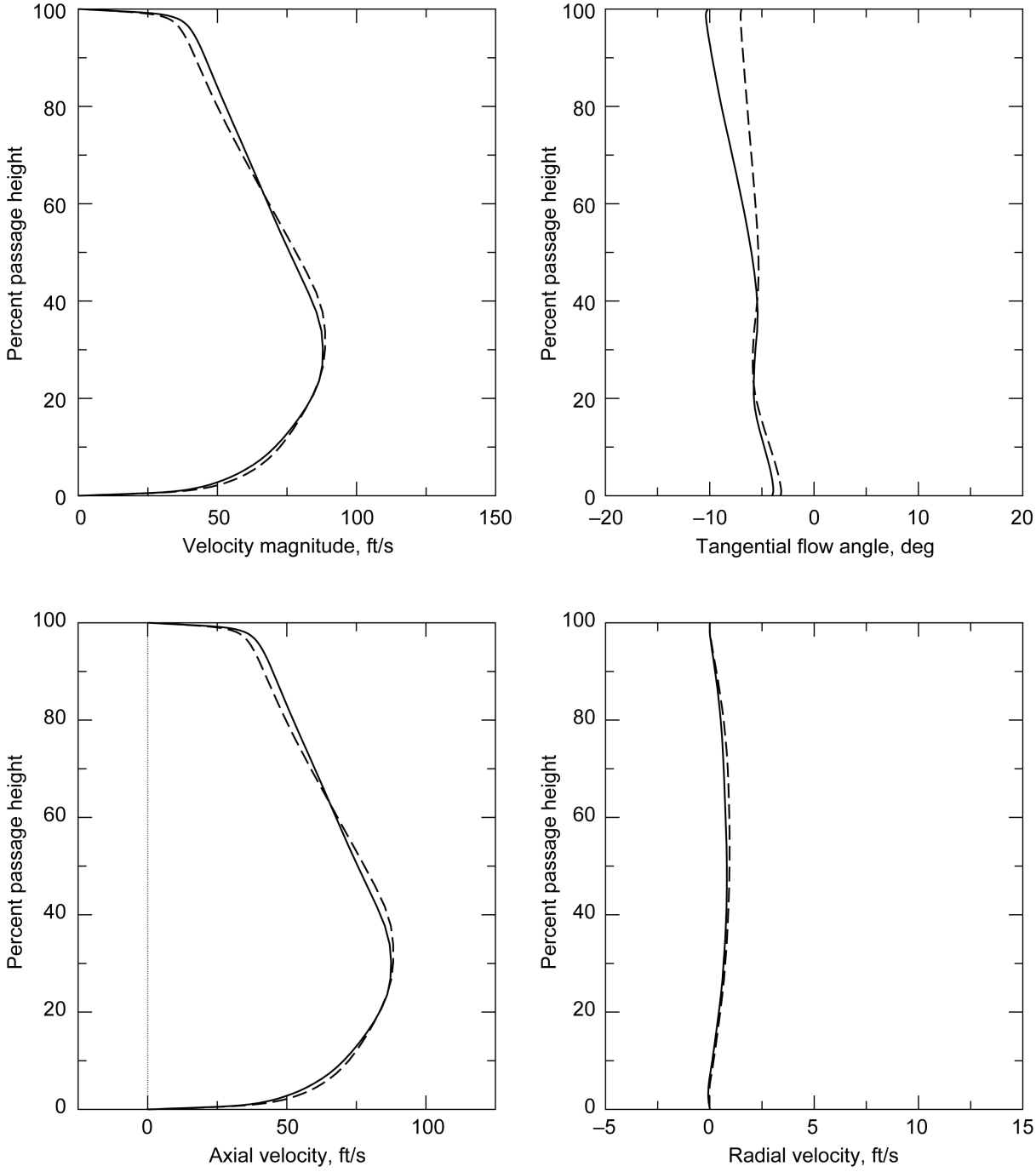

Figure 23(b).—Station 3d flow property profiles (circumferentially averaged flow).

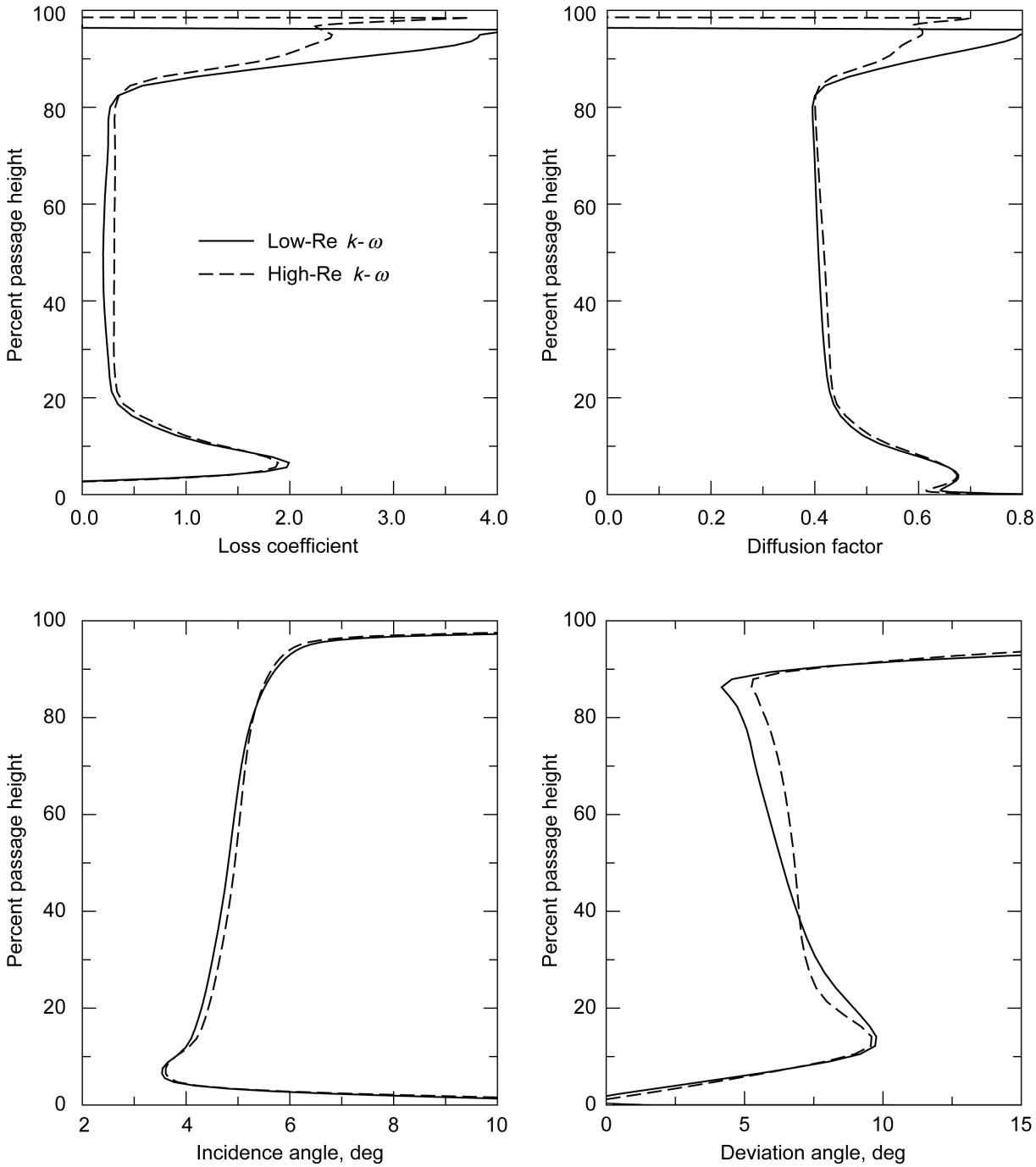

Figure 24(a).—Spanwise distributions of rotor blade row aerodynamic parameters.

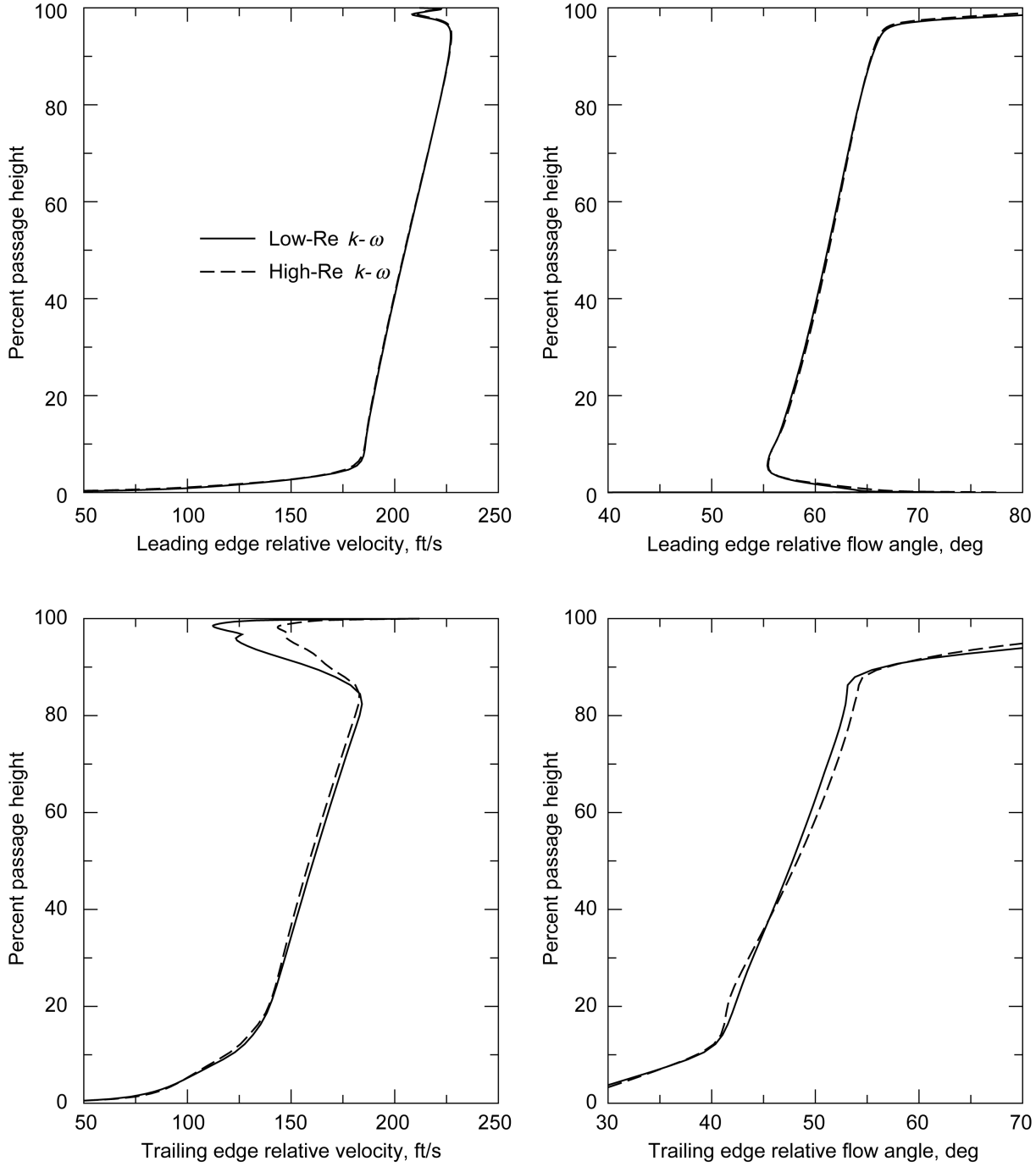

Figure 24(b).—Spanwise distributions of rotor blade row aerodynamic parameters.

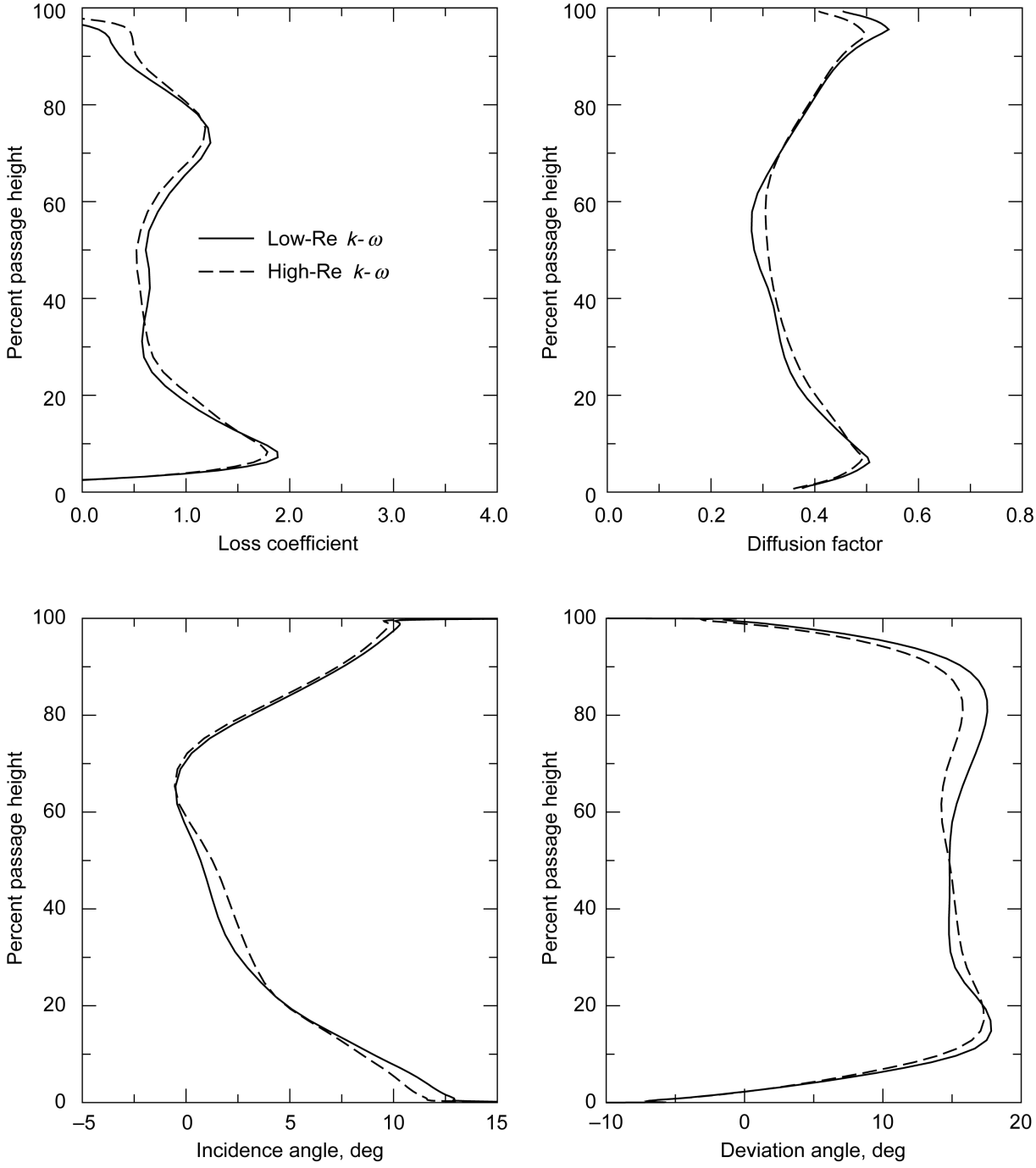

Figure 25(a).—Spanwise distributions of stator blade row aerodynamic parameters.

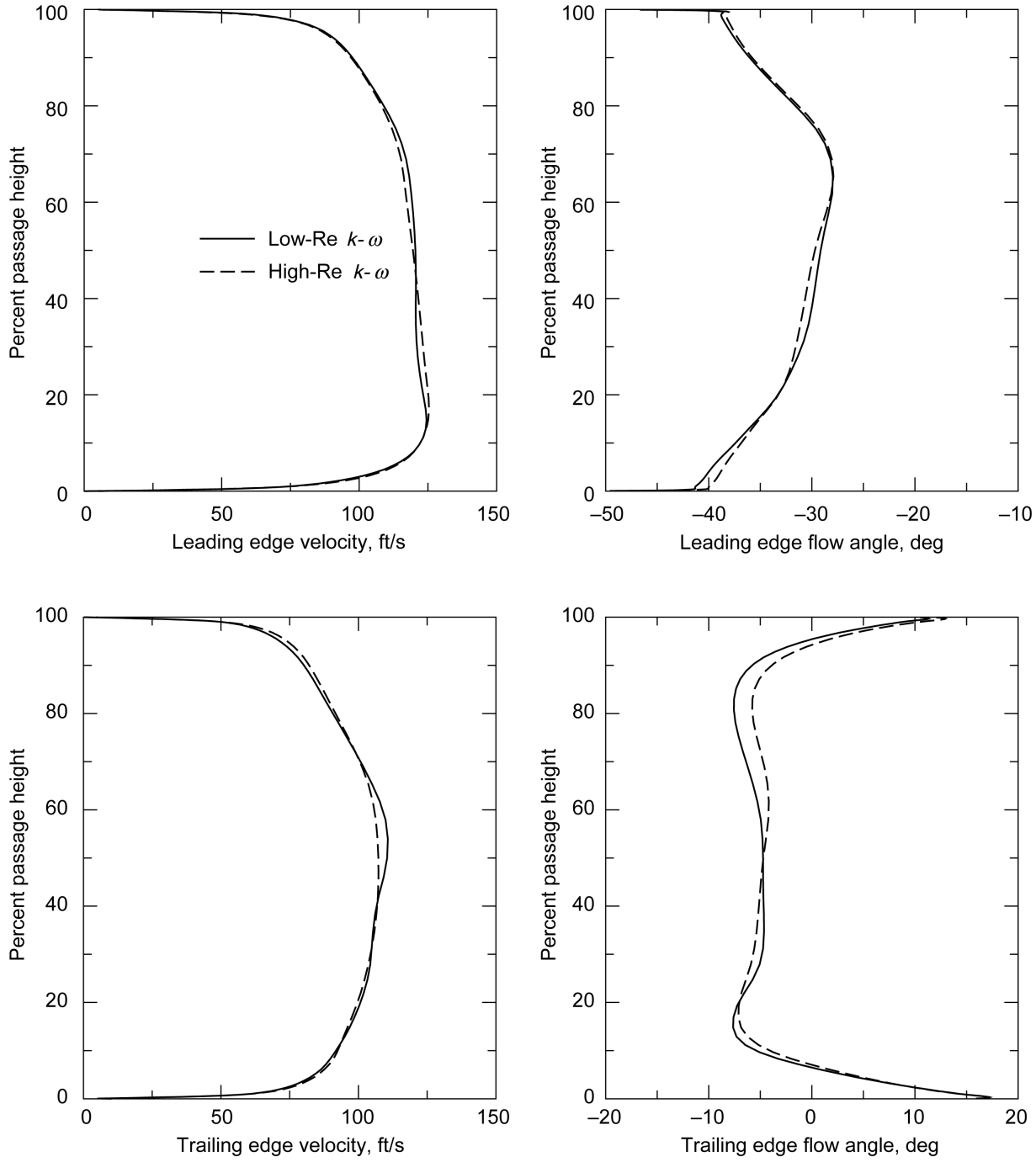

Figure 25(b).—Spanwise distributions of stator blade row aerodynamic parameters.

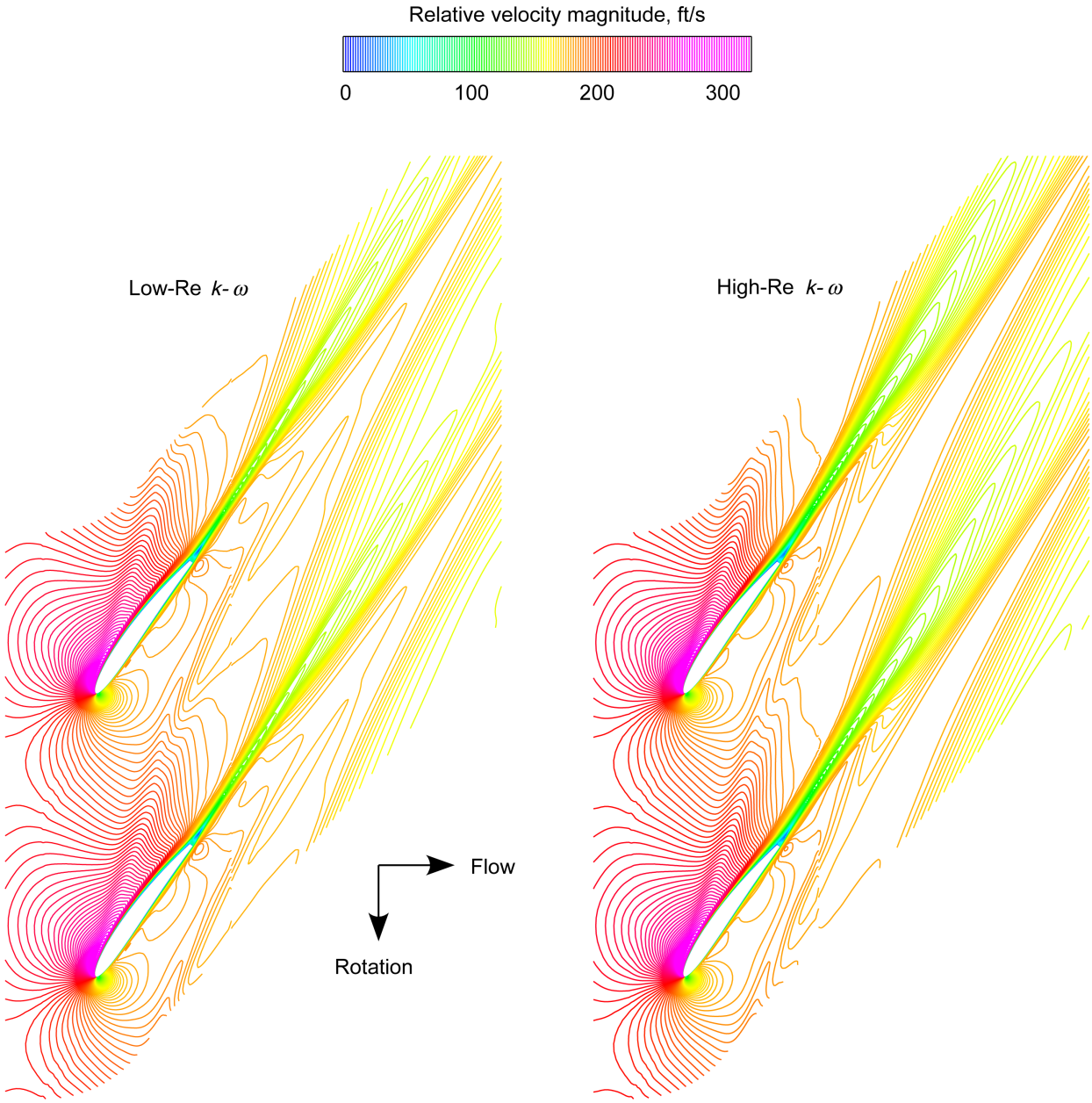

Figure 26(a).—Computed rotor flow field for design operating conditions; relative velocity magnitude; 85 percent of passage flow.

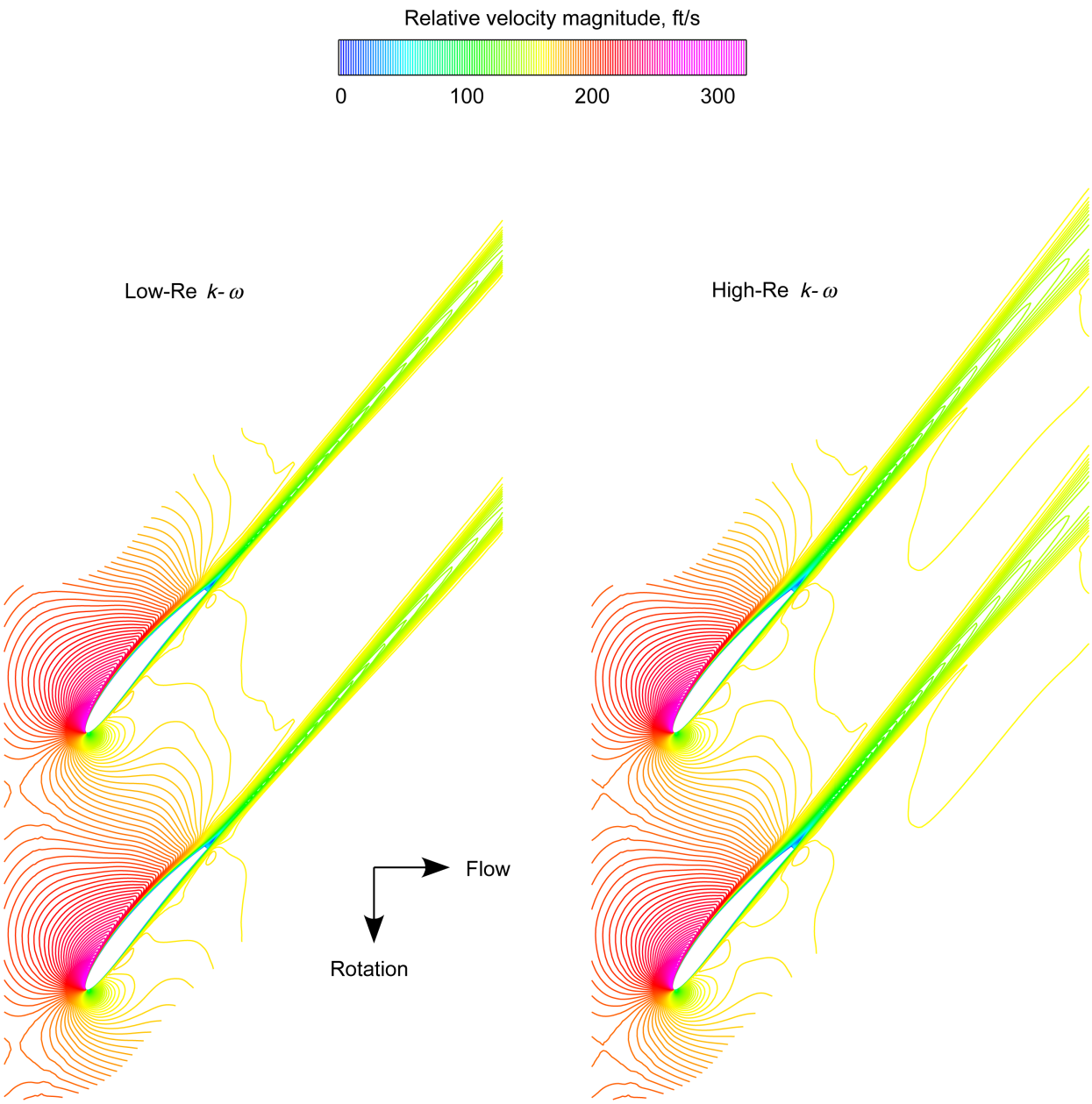

Figure 26(b).—Computed rotor flow field for design operating conditions; relative velocity magnitude; 50 percent of passage flow.

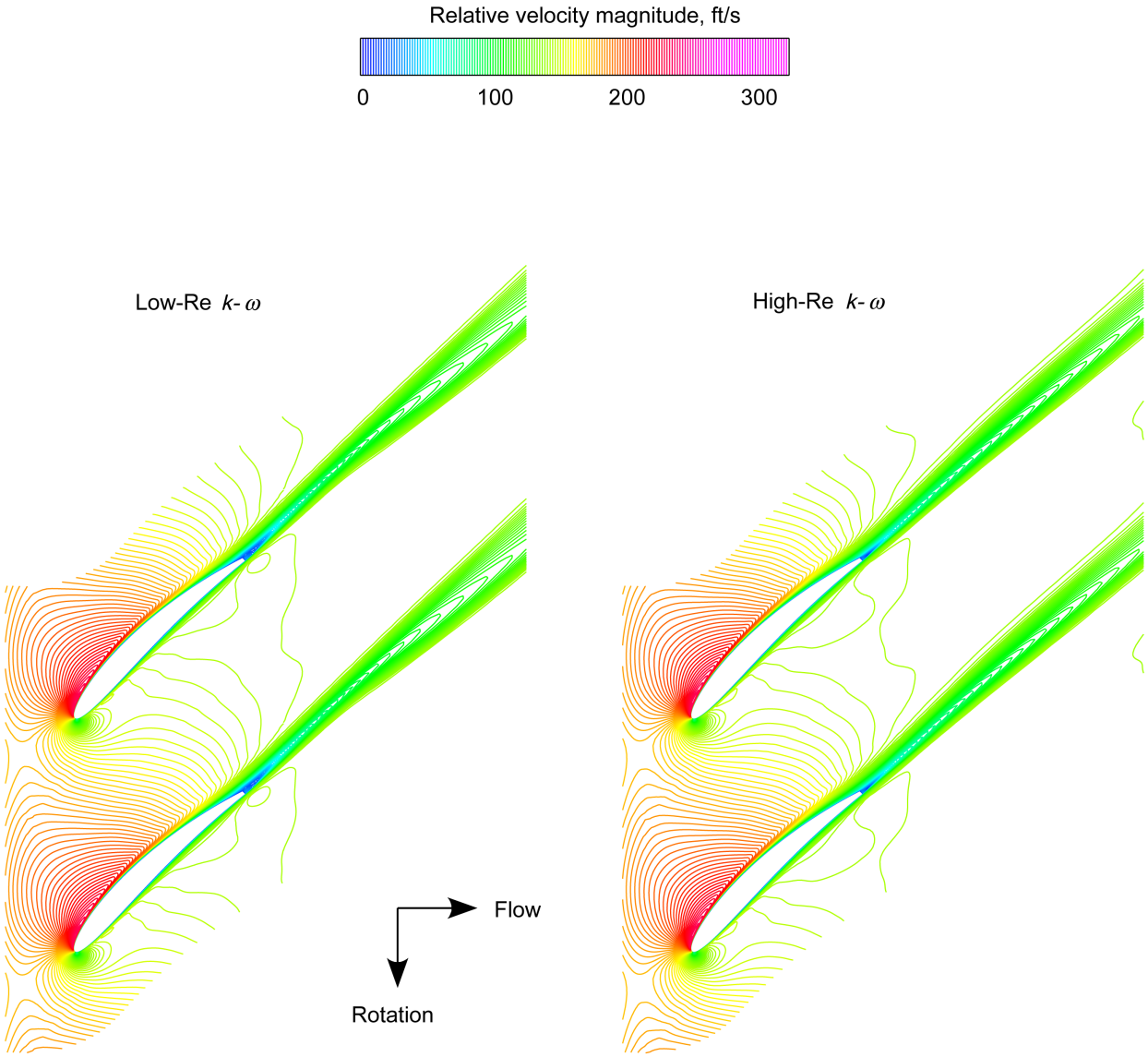

Figure 26(c).—Computed rotor flow field for design operating conditions; relative velocity magnitude; 15 percent of passage flow.

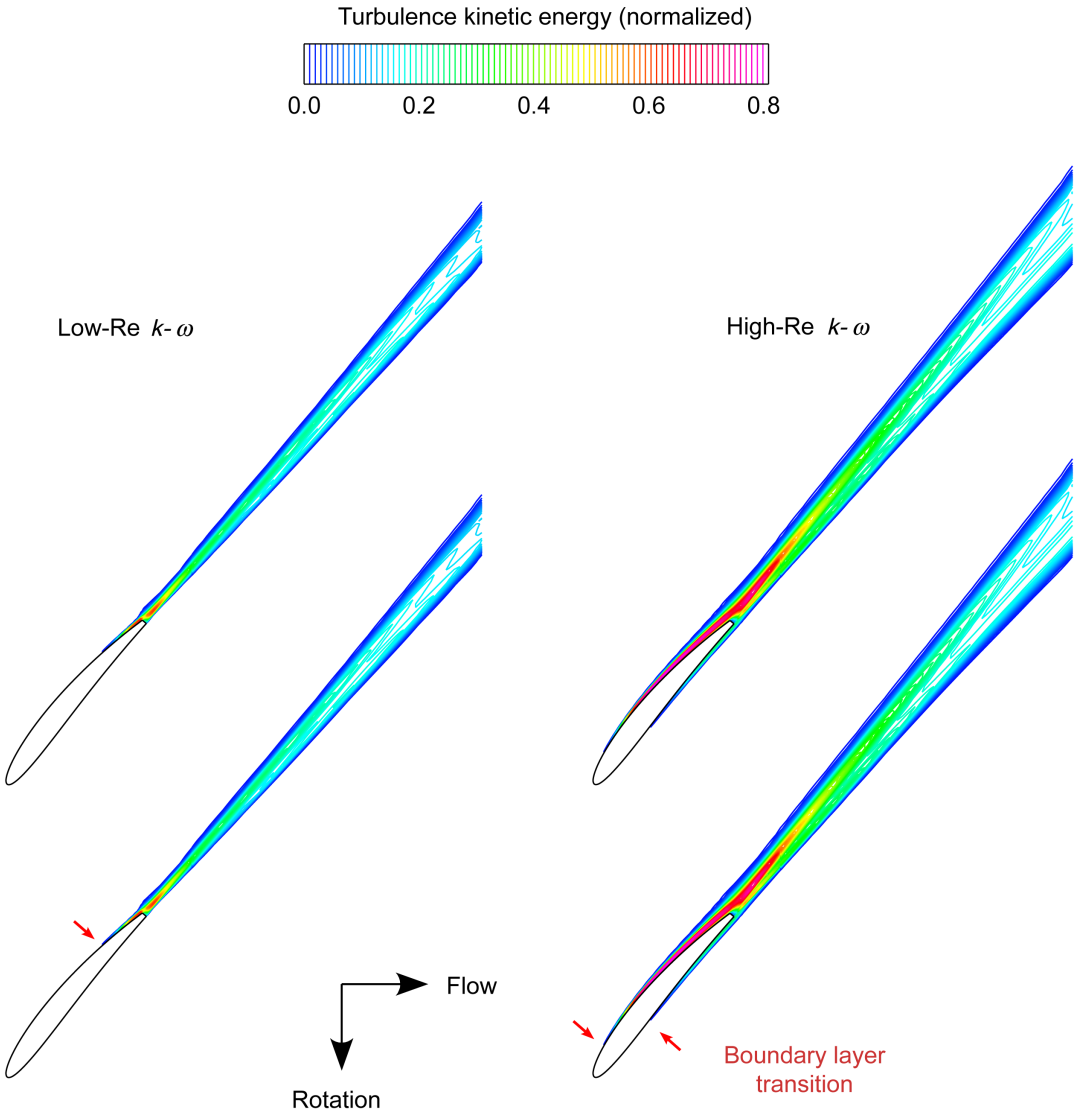

Figure 27.—Computed rotor flow field for design operating conditions; turbulence kinetic energy; 50 percent of passage flow.

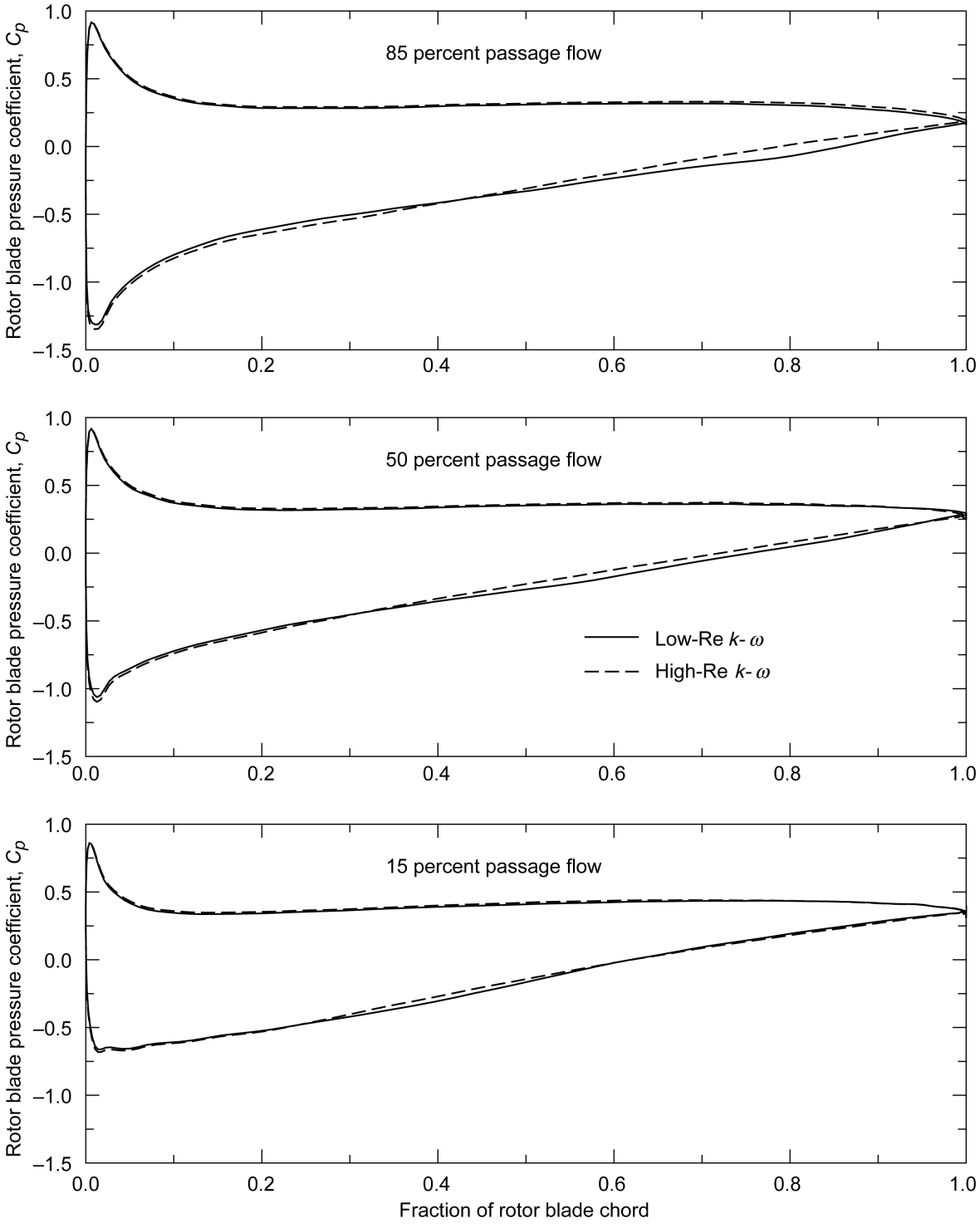

Figure 28.—Chordwise distributions of rotor blade surface pressure coefficient.

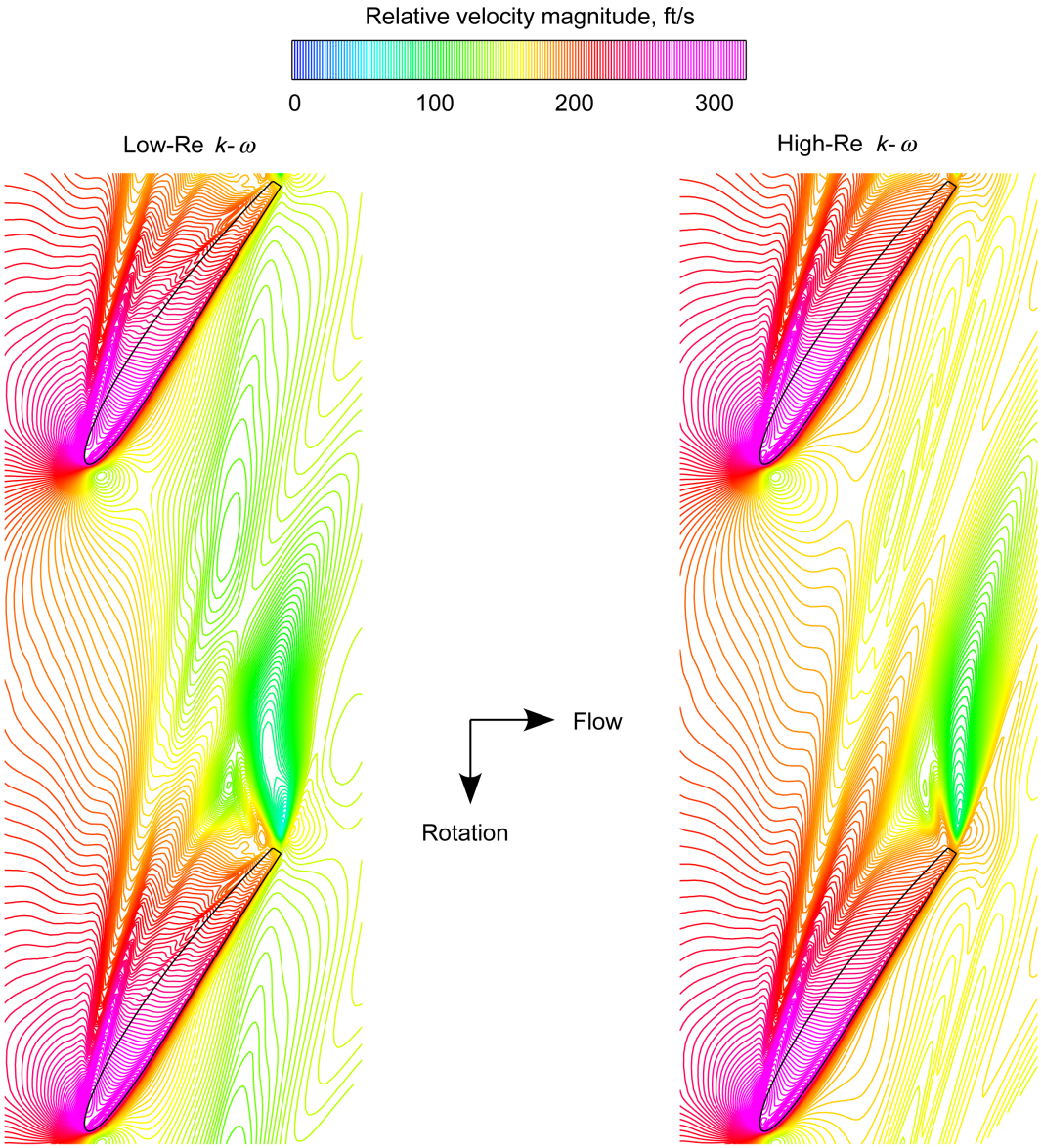

Figure 29(a).—Computed rotor-tip flow field for design operating conditions; relative velocity magnitude; mid-clearance-gap spanwise location.

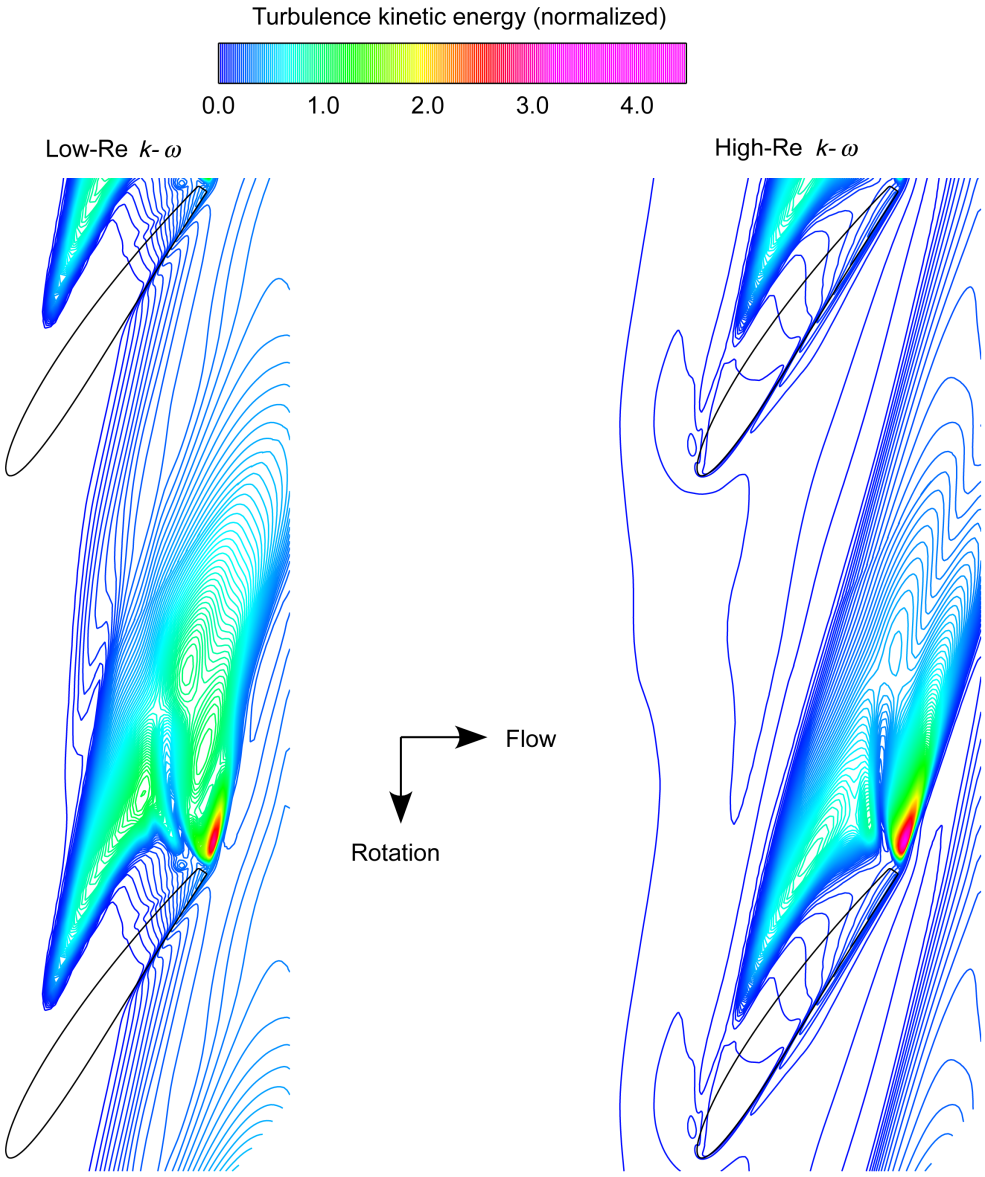

Figure 29(b).—Computed rotor-tip flow field for design operating conditions; turbulence kinetic energy; mid-clearance-gap spanwise location.

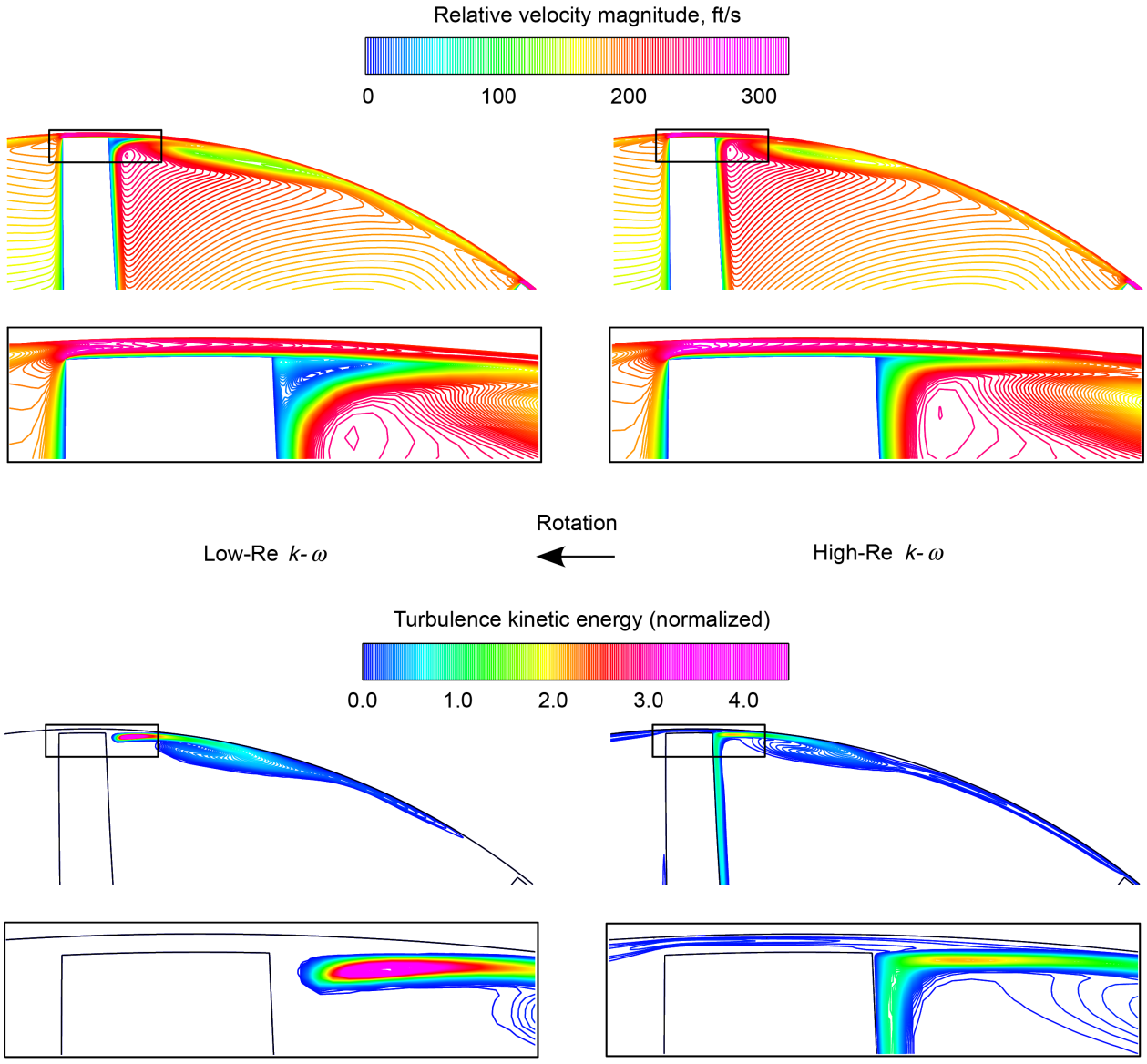

Figure 29(c).—Computed rotor-tip flow field for design operating conditions; midchord axial location.

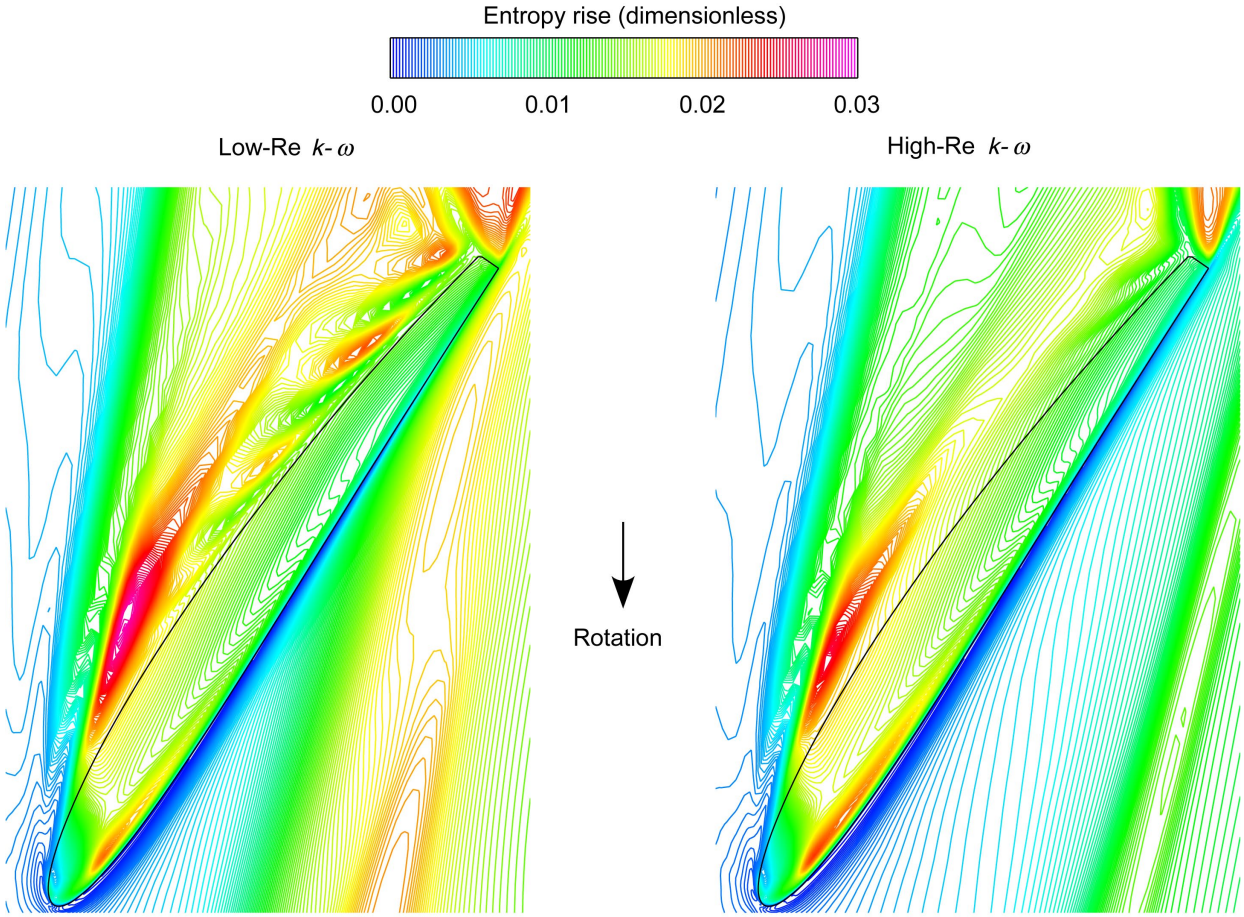

Figure 30.—Computed rotor-tip flow field for design operating conditions; entropy rise; near-blade tip spanwise location.

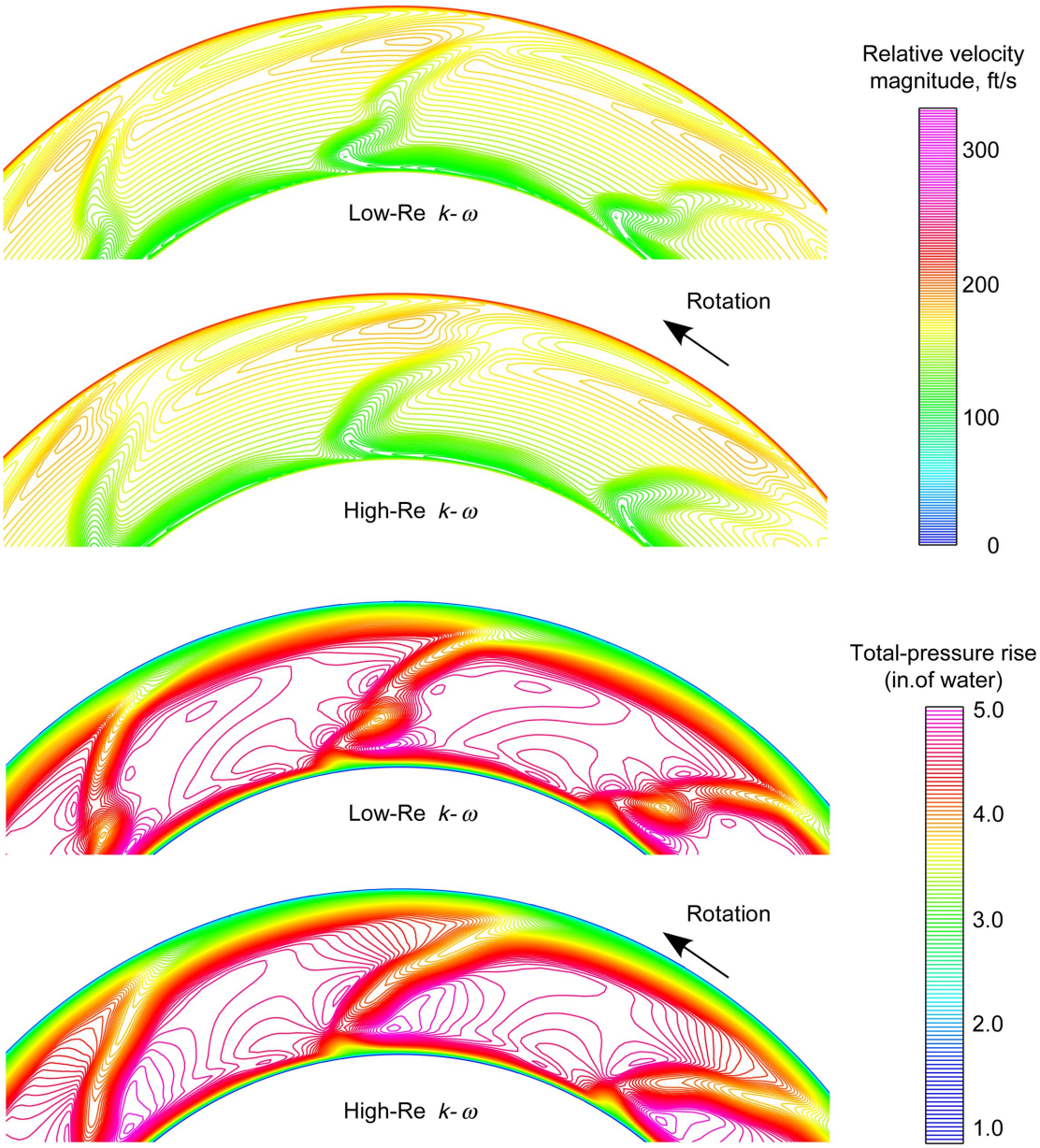

Figure 31(a).—Computed rotor exit flow field for design operating conditions; Station 2b.

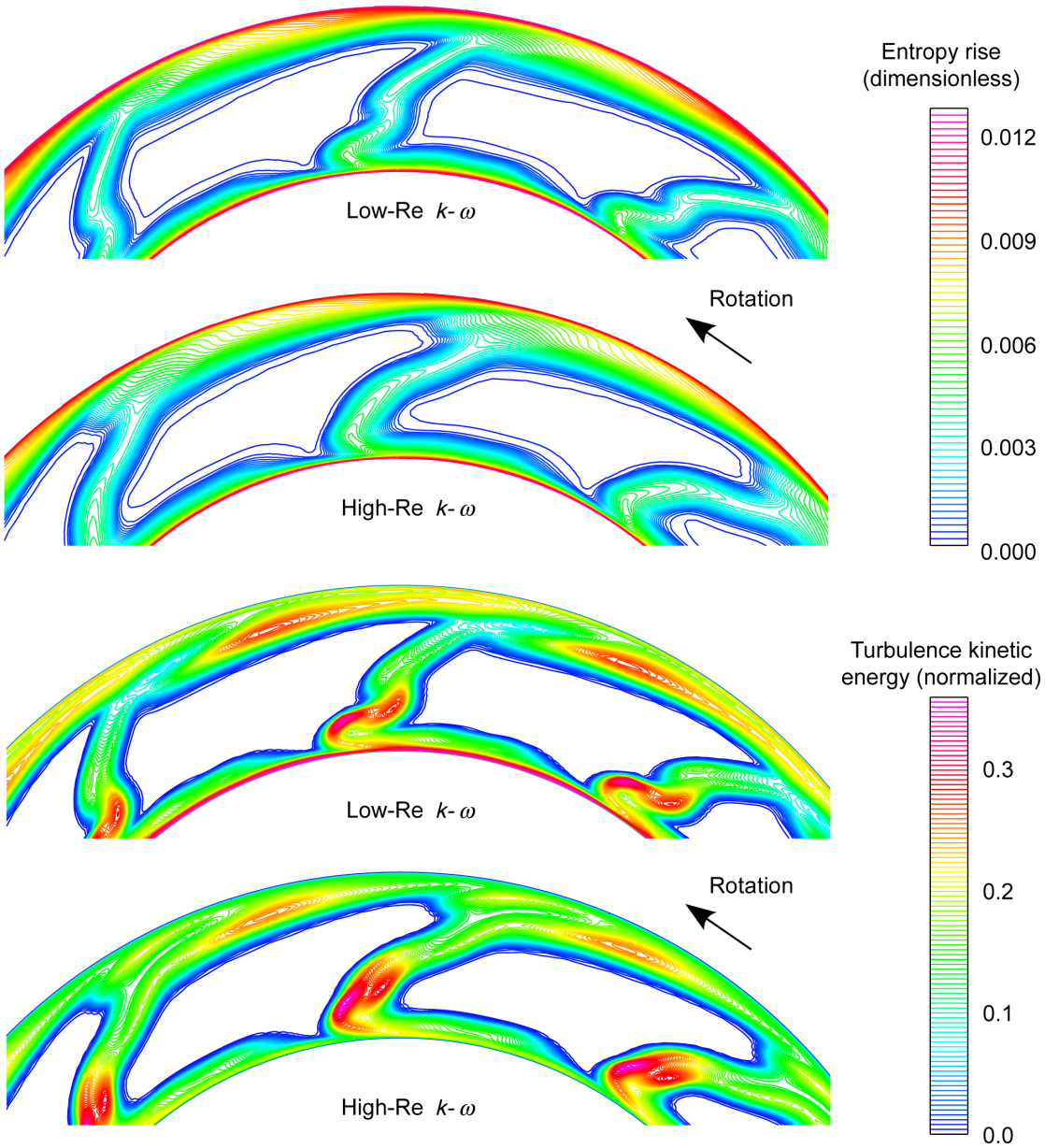

Figure 31(b).—Computed rotor exit flow field for design operating conditions; Station 2b.

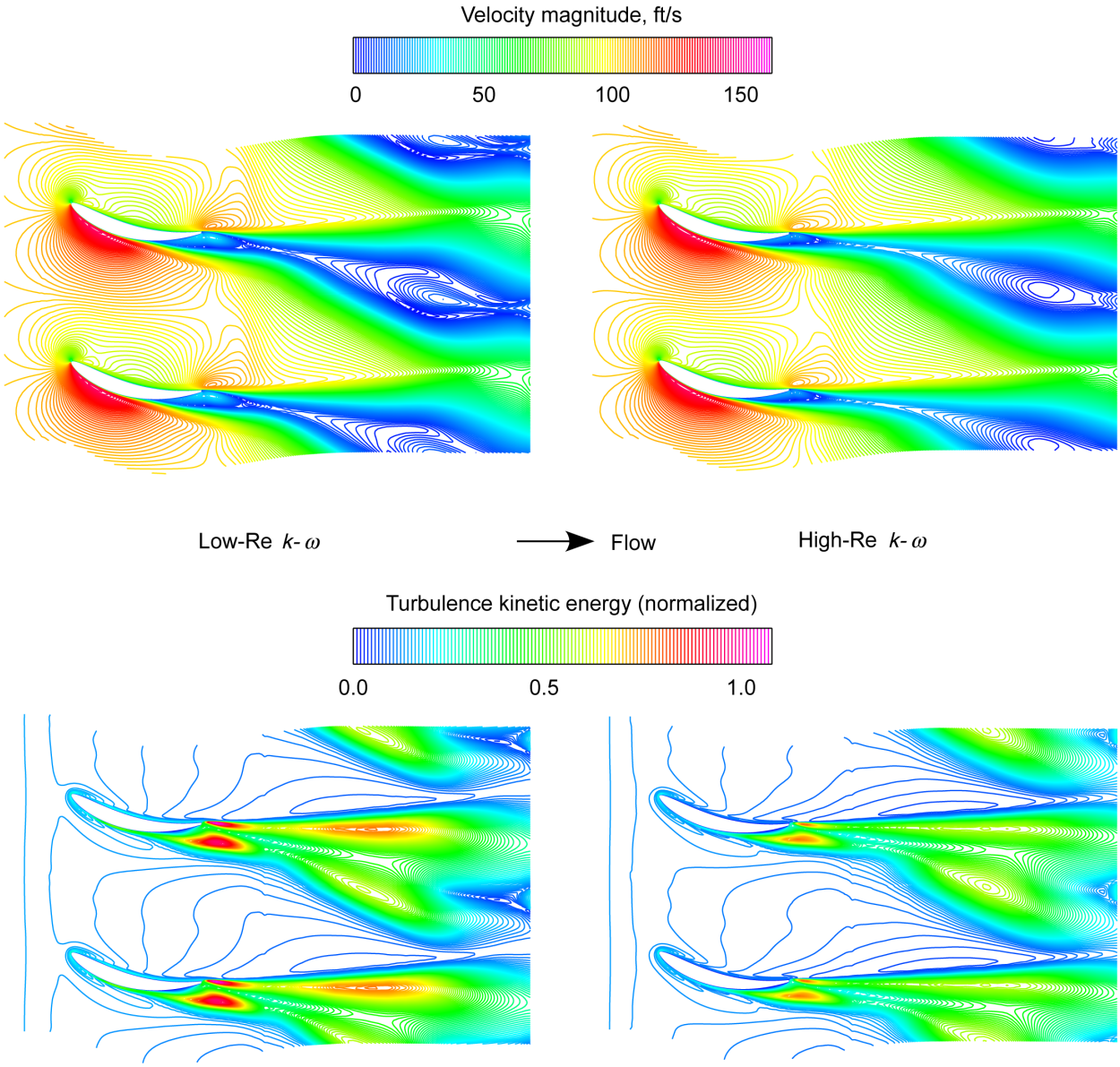

Figure 32(a).—Computed stator flow field for design operating conditions; 85 percent of passage flow.

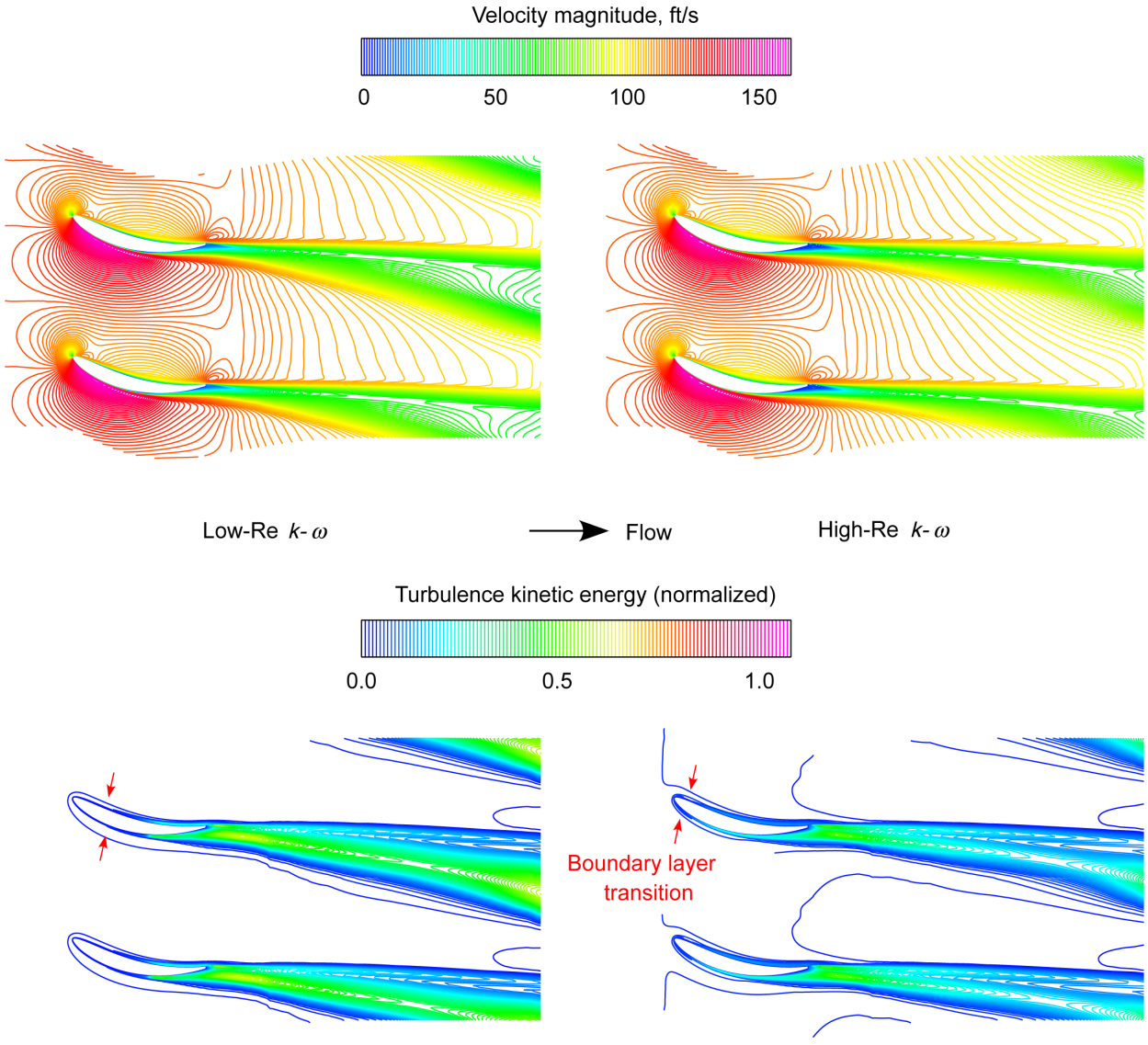

Figure 32(b).—Computed stator flow field for design operating conditions; 50 percent of passage flow.

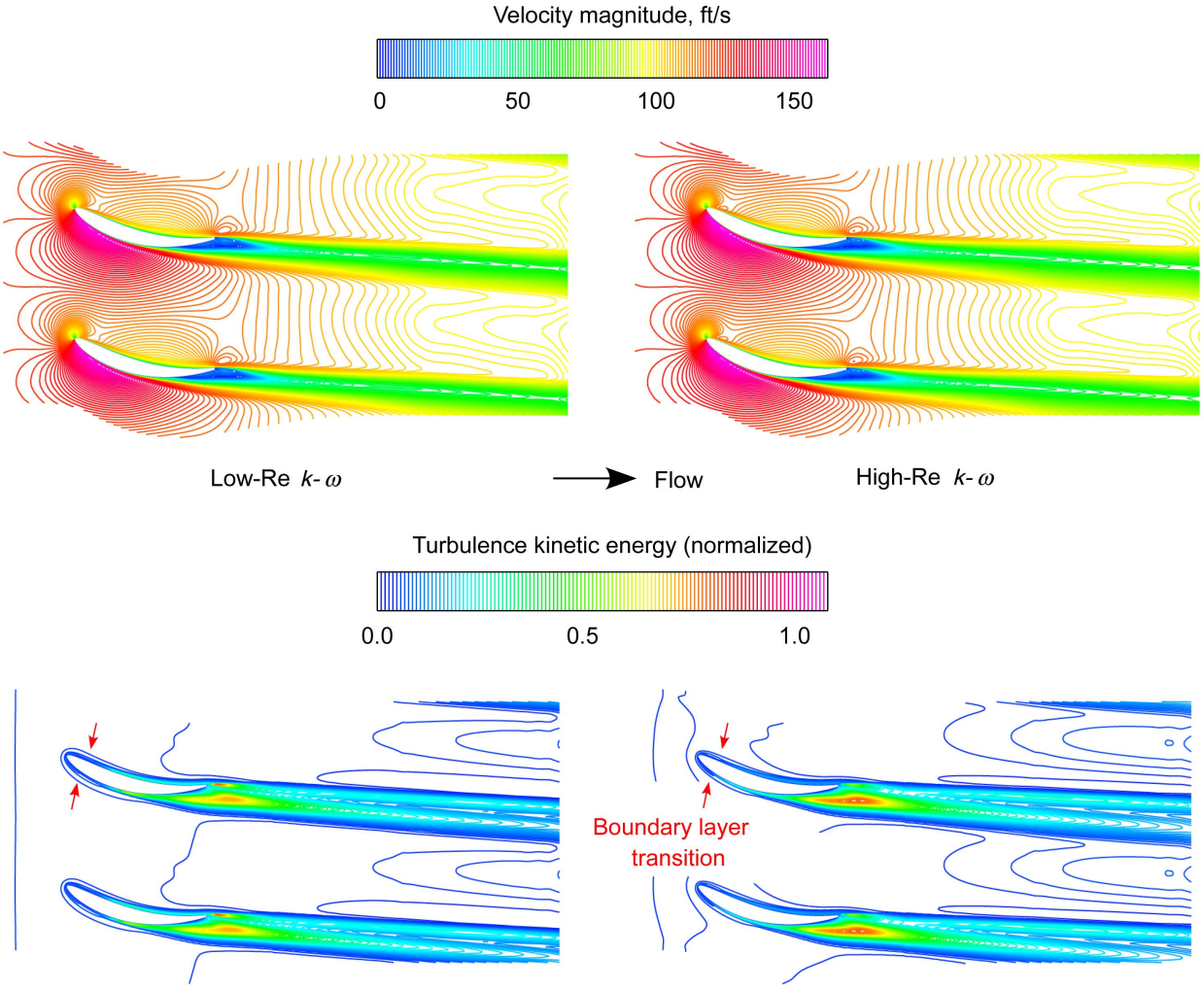

Figure 32(c).—Computed stator flow field for design operating conditions; 15 percent of passage flow.

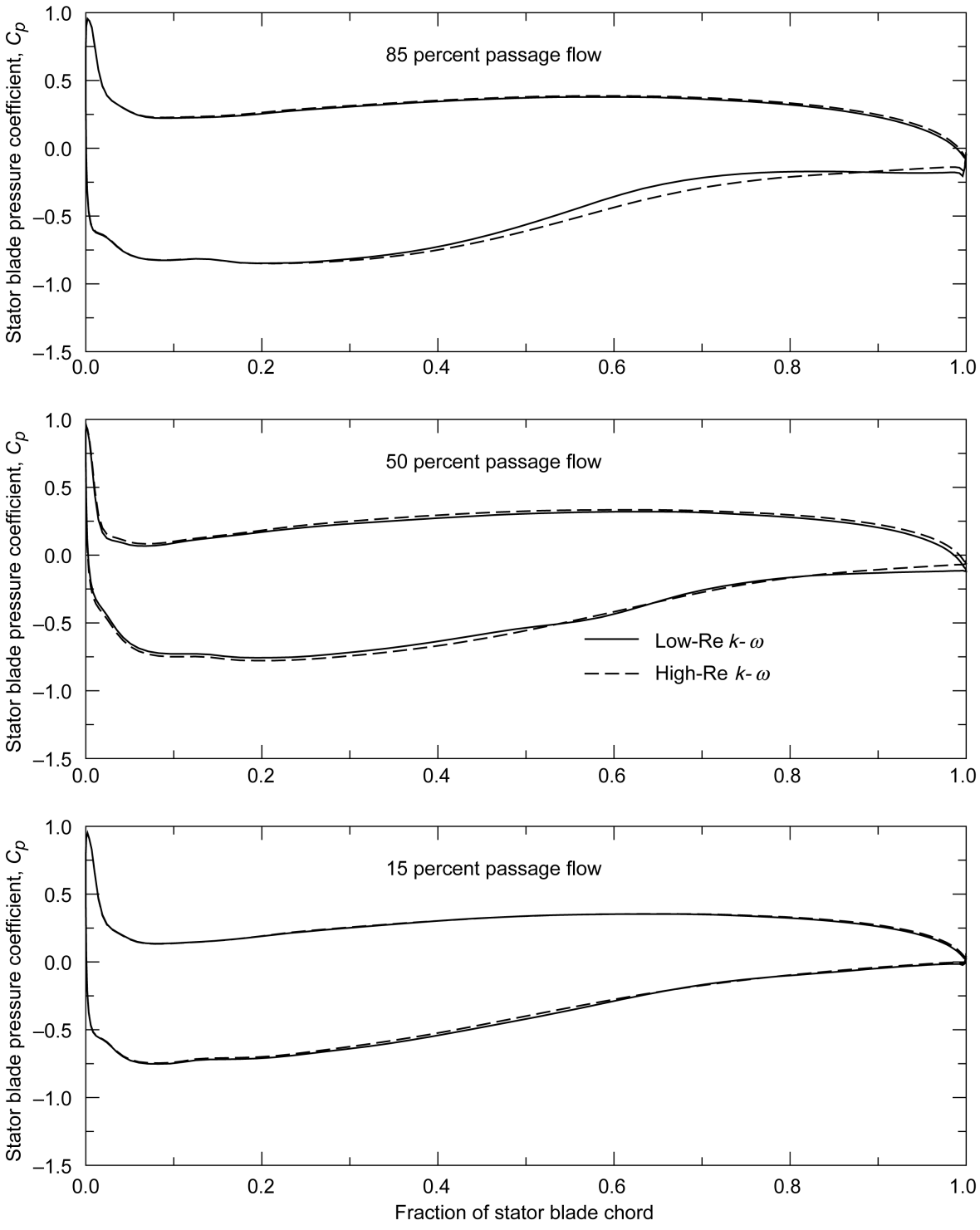

Figure 33.—Chordwise distributions of stator blade surface pressure coefficient.

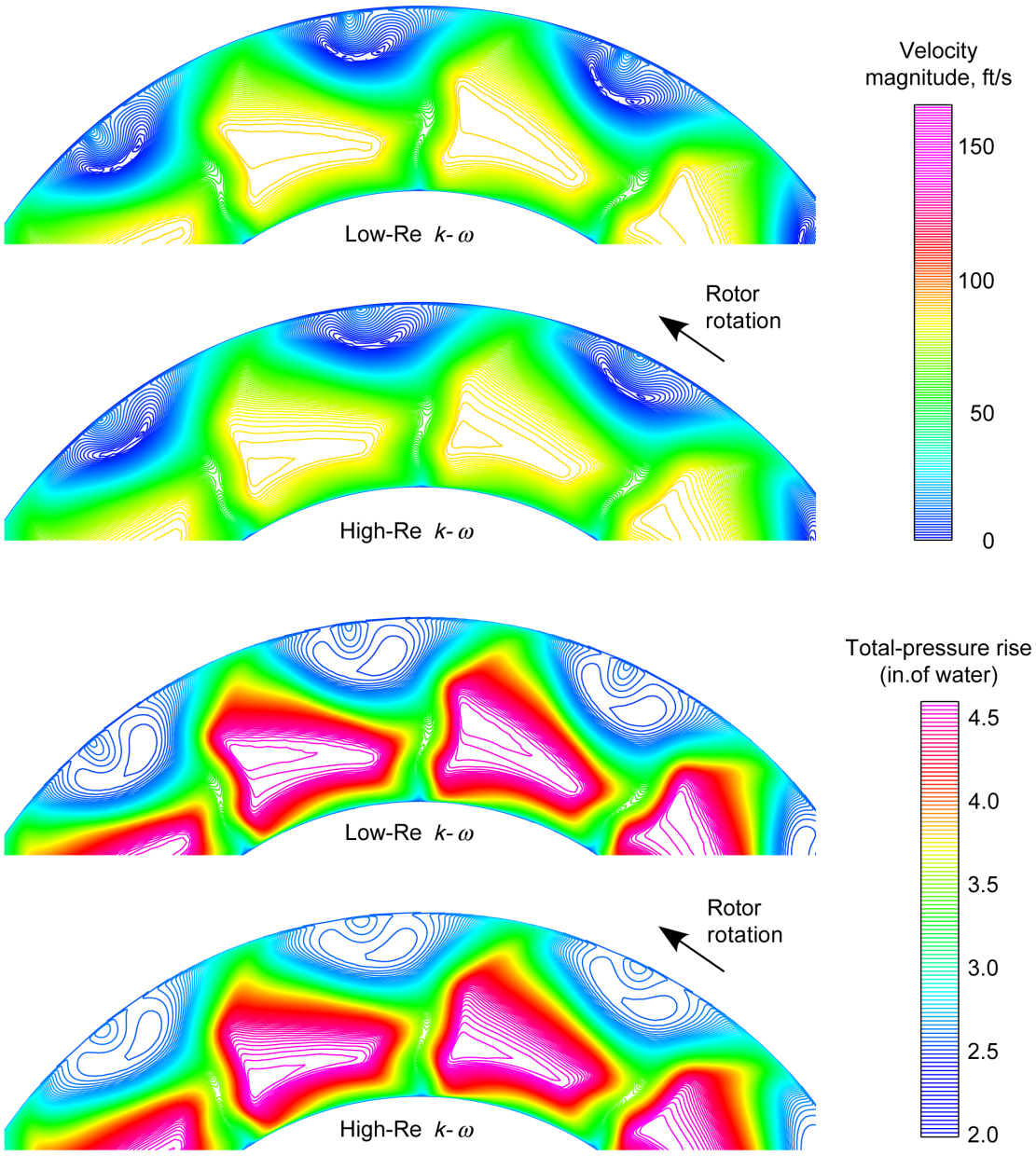

Figure 34(a).—Computed stator exit flow field for design operating conditions; Station 3c.

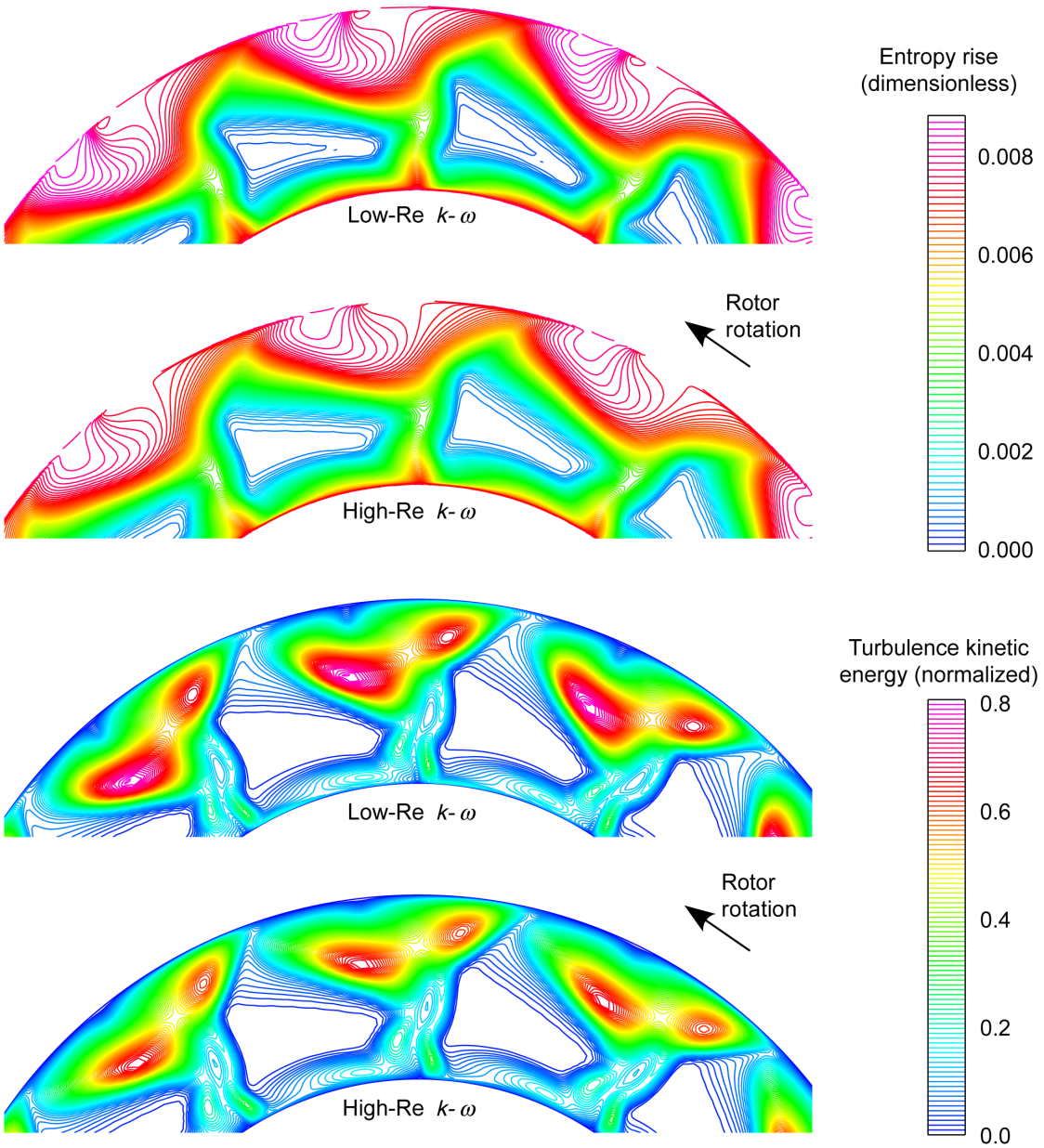

Figure 34(b).—Computed stator exit flow field for design operating conditions; Station 3c.

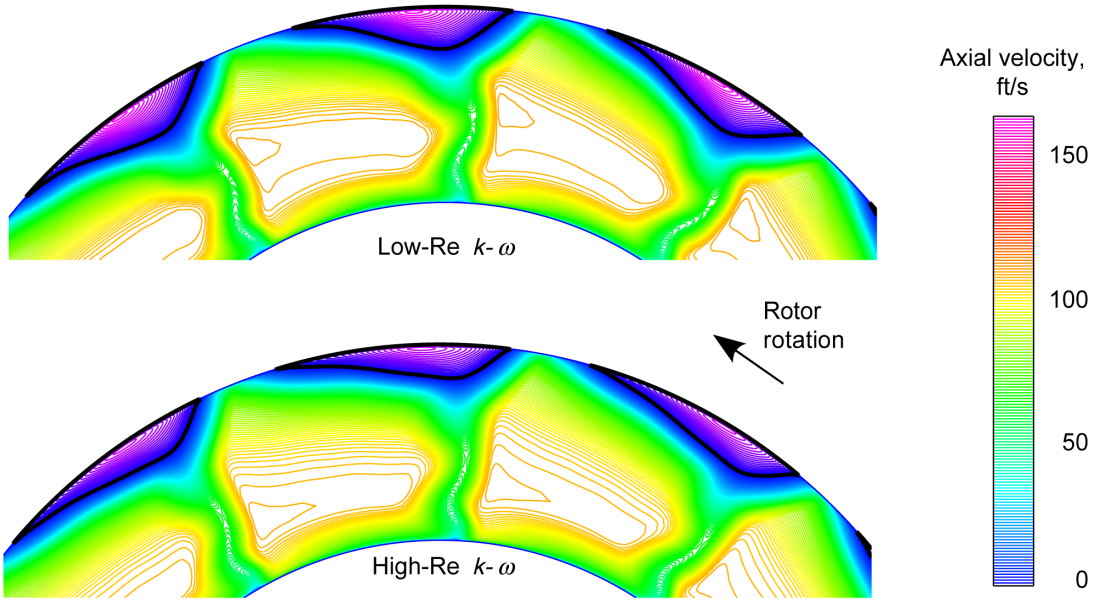

Figure 34(c).—Computed stator exit flow field for design operating conditions; Station 3c.

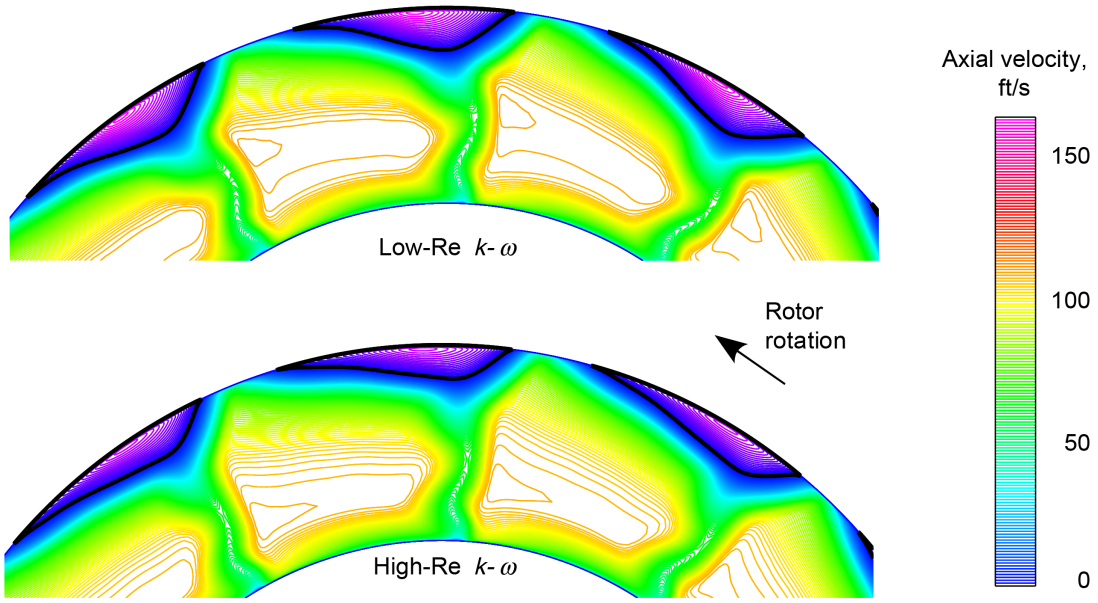

Figure 35.—Computed stator exit flow field for design operating conditions; Station 3c.

REPORT DOCUMENTATION PAGE	Form Approved OMB No. 0704-0188

1. REPORT DATE *(DD-MM-YYYY)*	2. REPORT TYPE	3. DATES COVERED *(From - To)*
01-12-2010	Final Contractor Report	

4. TITLE AND SUBTITLE
Computational Aerodynamic Simulations of a Spacecraft Cabin Ventilation Fan Design

5a. CONTRACT NUMBER
NNC06BA07B

5b. GRANT NUMBER

5c. PROGRAM ELEMENT NUMBER

6. AUTHOR(S)
Tweedt, Daniel, L.

5d. PROJECT NUMBER

5e. TASK NUMBER
Task 190

5f. WORK UNIT NUMBER
WBS 439906.04.01.02.02

7. PERFORMING ORGANIZATION NAME(S) AND ADDRESS(ES)
AP Solutions, Inc.,
5075 Everton Ave.
Solon, Ohio 44139

8. PERFORMING ORGANIZATION REPORT NUMBER
E-17264

9. SPONSORING/MONITORING AGENCY NAME(S) AND ADDRESS(ES)
National Aeronautics and Space Administration
Washington, DC 20546-0001

10. SPONSORING/MONITOR'S ACRONYM(S)
NASA

11. SPONSORING/MONITORING REPORT NUMBER
NASA/CR-2010-216330

12. DISTRIBUTION/AVAILABILITY STATEMENT
Unclassified-Unlimited
Subject Categories: 02 and 71
Available electronically at http://gltrs.grc.nasa.gov
This publication is available from the NASA Center for AeroSpace Information, 443-757-5802

13. SUPPLEMENTARY NOTES

14. ABSTRACT
Quieter working environments for astronauts are needed if future long-duration space exploration missions are to be safe and productive. Ventilation and payload cooling fans are known to be dominant sources of noise, with the International Space Station being a good case in point. To address this issue cost effectively, early attention to fan design, selection, and installation has been recommended, leading to an effort by NASA to examine the potential for small-fan noise reduction by improving fan aerodynamic design. As a preliminary part of that effort, the aerodynamics of a cabin ventilation fan designed by Hamilton Sundstrand has been simulated using computational fluid dynamics codes, and the computed solutions analyzed to quantify various aspects of the fan aerodynamics and performance. Four simulations were performed at the design rotational speed: two at the design flow rate and two at off-design flow rates. Following a brief discussion of the computational codes, various aerodynamic- and performance-related quantities derived from the computed flow fields are presented along with relevant flow field details. The results show that the computed fan performance is in generally good agreement with stated design goals.

15. SUBJECT TERMS
Fans; Aerodynamics; Noise; Performance

16. SECURITY CLASSIFICATION OF:			17. LIMITATION OF ABSTRACT	18. NUMBER OF PAGES	19a. NAME OF RESPONSIBLE PERSON
a. REPORT	b. ABSTRACT	c. THIS PAGE			STI Help Desk (email:help@sti.nasa.gov)
U	U	U	UU	65	19b. TELEPHONE NUMBER *(include area code)* 443-757-5802